NOVEL INSTRUMENTATION FOR A SCATTERING INDEPENDENT MEASUREMENT OF THE ABSORPTION COEFFICIENT OF NATURAL WATERS, AND A NEW DIFFUSE REFLECTOR FOR SPECTROSCOPIC INSTRUMENTATION AND CLOSE CAVITY COUPLING

A Dissertation

by

JOSEPH ALAN MUSSER

Submitted to the Office of Graduate Studies of
Texas A&M University
in partial fulfillment of the requirements for the degree of

DOCTOR OF PHILOSOPHY

December 2006

Major Subject: Physics

NOVEL INSTRUMENTATION FOR A SCATTERING INDEPENDENT MEASUREMENT OF THE ABSORPTION COEFFICIENT OF NATURAL WATERS, AND A NEW DIFFUSE REFLECTOR FOR SPECTROSCOPIC INSTRUMENTATION AND CLOSE CAVITY COUPLING

A Dissertation

by

JOSEPH ALAN MUSSER

Submitted to the Office of Graduate Studies of
Texas A&M University
in partial fulfillment of the requirements for the degree of

DOCTOR OF PHILOSOPHY

Approved by:

Chair of Committee,	Edward S. Fry
Committee Members,	John W. Bevan
	Robert A. Kenefick
	Marlan O. Scully
	George R. Welch
Head of Department,	Edward S. Fry

December 2006

Major Subject: Physics

ABSTRACT

Novel Instrumentation for a Scattering Independent Measurement of the Absorption Coefficient of Natural Waters, and a New Diffuse Reflector for Spectroscopic Instrumentation and Close Cavity Coupling. (December 2006)

Joseph Alan Musser, B.S., West Texas State University

Chair of Advisory Committee: Dr. Edward S. Fry

We report results for the development of a flow-through integrated cavity absorption meter (ICAM.) Absorption measurements have been made with 2% or less change in the signal in the presence of up to 10 m^{-1} of scattering in the medium. The operating range of the ICAM ranges from 0.004 m^{-1} to over 40 m^{-1} of absorption. This range allows one to use a single instrument to measure the absorption from sediment laden rivers out to the cleanest of ocean waters. Further, the ICAM signal has been shown to be independent of the flow rate and turbulence in the medium. In addition we report the development of a diffuse reflector which, to our best knowledge, has the highest measured diffuse reflectivity of 0.998 at 532 nm and 0.996 at 266 nm. We also show that the average distance a photon travels between successive reflections in an integrating cavity of arbitrary shape is four times the volume divided by the surface area, 4 V/S. Further, for a cavity which is formed by planes tangent to an inscribed sphere and which maintains a homogeneous and isotropic field, the average distance traveled by a photon between successive reflections is equal to 4 V/S of the inscribed sphere. Thus, each cavity has the same ratio of V/S as the inscribed sphere. These advances lead to an

increase in the sensitivity of absorption spectroscopy. The sensitivity approaches that of cavity ring down spectroscopy (CARS), without the adverse scattering effects traditionally associated with CARS.

ACKNOWLEDGEMENTS

"No man is an island, entire of itself; every man is a piece of the continent, a part of the main." John Donne wrote these words over 375 years ago in Meditation XVII. Many have played a role in my journey here at Texas A&M University. The "encouragement" I received, from both my father, Ed Musser, and my sister-in-law, Kristen Musser, to return to school planted the seed that later matured. I also thank my fellow faculty at Caprock high school in Amarillo, Texas for their support throughout this venture.

At TAMU I found my fellow graduate students to be my greatest resource. Brian Hennings, Jim Musser, Scott Nooner and Joel Walker were instrumental in my education. In the lab I have had the privilege of interacting with Frank Giouco, David Haubrich, Jeffrey Katz, Jayson Stewart, John Volpert and Ling Wang. Deric Gray also deserves special mention for his role as we brought this project alive and subsequently drove it straight down into the ground. Actually, he was instrumental in its remarkable success, along with my advisor Dr. Ed Fry. I also thank the rest of my committee for their support, especially Dr. Robert Kenefick. Dr. Robert Beck Clark has been a source of support, a teacher and a mentor throughout my time here; he is an example to all. I would not be where I am today, were it not for my parents Edgar and Patsy Musser. I also thank my brothers and my sisters-in-law for their encouragement: Bob, Tom, Bill, Jim, Donna and Kristen.

TABLE OF CONTENTS

CHAPTER Page

LIST OF TABLES

LIST OF FIGURES

FIGURE Page

FIGURE Page

FIGURE Page

CHAPTER I

INTRODUCTION AND BACKGROUND

Much of the information we gather from the natural world comes to us via scattered light. From utilitarian information such as the location and identification of objects, to the aesthetics of viewing a beautiful sunset or marveling at a double rainbow, all of these are visible to us through scattered light. Most of the light one sees is from diffuse scattering. Take a moment and consider how our perception of the world would change if scattering was predominantly specular rather than diffuse. The only surfaces which would be visible are those whose normal bisects the angle formed by the incident ray and the scattered ray. It truly would be a different world, with an object's appearance being highly dependent upon its position. Of course when we say light is diffusely scattered we are really making a comment not so much about light, but about the object scattering it.

1. Optical Properties

The mechanism for scattering light is best explained with the dipole. Polarized light interacts with the charged particles within matter. Electromagnetic fields drive the charges in atoms and molecules to move and oscillate within the material, creating a dipole. Thus energy from the electromagnetic field is absorbed into the material. Just as

---

This dissertation follows the style and format of Applied Optics.

an electromagnetic wave produces acceleration in charged objects, accelerating charges produce a changing electromagnetic field. In this manner the electromagnetic wave is reradiated. The direction of the wave may change as well as the phase of the wave. This is affected by how the dipoles in the material are oriented, how they interact with neighboring dipoles, as well as how they individually interact with the light field. When no energy is lost to the atom or molecule it is referred to as elastic scattering. Light may also be absorbed without reradiating, causing a vibrational, rotational or electronic transition. The light may be transmitted without any change in its wavelength or direction. Understanding and being able to measure these three parameters - scattering, absorption and transmission - independently of each other provides a wealth of knowledge regarding the identity and characteristic behavior of the material. Scattering, absorption and transmission of light can also vary as a function of wavelength. Thus it is desirable to measure these quantities at multiple narrow wavelength bands across the spectrum. Within the remote sensing field this type of measurement is curiously referred to as hyperspectral sensing. The prefix hyper- is defined by Merriam-Webster as more of, above, beyond, excessive. Unfortunately, hyperspectral is part of the vernacular and we are now stuck with it.

We are primarily concerned with scattering, absorption, and transmission in natural waters, part of a field more generally termed marine or ocean optics. In natural waters these parameters are affected not only by the water medium itself, but also by the constituents within the medium; these constituents can be dissolved matter or suspended particulates. Consider a collimated, monochromatic beam of light incident upon a thin

column of water, see Fig. 1. It is clear from conservation of energy that the power of the light absorbed P_a, plus the power of the light scattered in all directions P_s, plus the power of the light transmitted P_t, is equal to the incident power P_i.

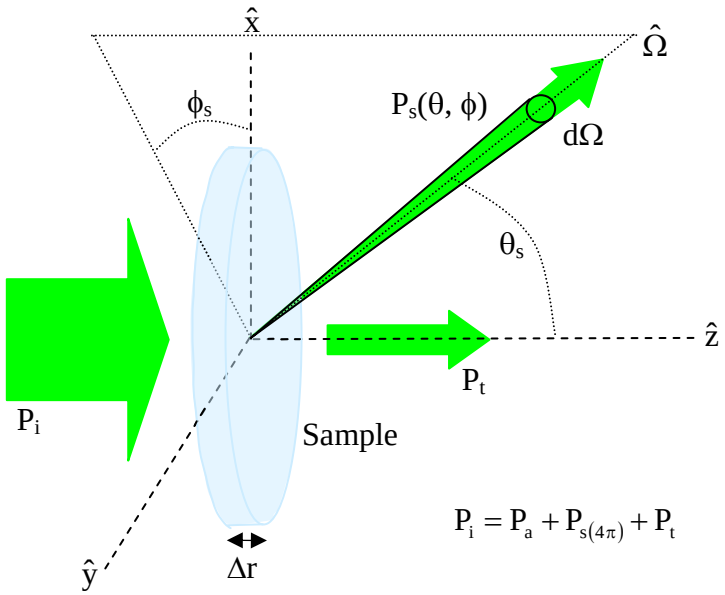

Fig. 1. The interaction of light with matter.

The volume scattering function $\beta_\lambda(\theta, \phi)$ describes the distribution of the scattered light. Sometimes this much detail is not necessary and the scattering will be described by the scattering coefficient b, the back scattering coefficient b_b, and the forward scattering coefficient b_f as defined in the following equations, see Fig. 1:

$$\beta_\lambda(\theta,\phi) \equiv \underset{\Delta r\to 0}{\text{Lim}}\,\underset{\Delta\Omega\to 0}{\text{Lim}}\frac{\left(P_s(\theta,\phi)/P_i\right)}{\Delta r\Delta\Omega}, \tag{1.1}$$

$$b \equiv \underset{\Delta r\to 0}{\text{Lim}}\frac{\left(P_s/P_i\right)}{\Delta r} = \int_{4\pi}\beta(\theta,\phi)d\Omega, \tag{1.2}$$

$$b_b \equiv \int_0^{2\pi} d\phi \int_{\pi/2}^{\pi} \beta(\theta,\phi)\sin\theta d\theta, \tag{1.3}$$

$$b_f \equiv \int_0^{2\pi} d\phi \int_0^{\pi/2} \beta(\theta,\phi)\sin\theta d\theta. \tag{1.4}$$

The absorption coefficient is defined as follows,

$$a \equiv \lim_{\Delta r \to 0} \frac{(P_a / P_i)}{\Delta r}. \tag{1.5}$$

In Eqs. (1.2) - (1.5) we have suppressed any notation of wavelength dependence; it is to be understood that all these parameters are wavelength dependent. One can now describe the total beam attenuation c as the sum of the absorption coefficient and the scattering coefficient,

$$c = a + b. \tag{1.6}$$

In the ocean optics community it is customary to measure all these parameters in units of inverse meters, except for the volume scattering function which is typically in units of inverse meters-steradians. To further describe the nature in which light is scattered we define a parameter g where

$$g = \int_{4\pi} \frac{\beta(\theta,\phi)}{b} \cos\theta d\Omega. \tag{1.7}$$

Notice that g is normalized and has the range $-1 \le g \le 1$. As the scattering becomes strongly forward (backward) peaked g will approach 1 (-1); however, if the scattering is isotropic g will equal zero.

All of the properties we have discussed thus far have been dependent only on the material through which the light is propagating, not on the nature of the light field itself.

These types of properties are called inherent optical properties. Conversely properties which depend on both the light field and the medium through which it travels are called apparent optical properties. Two examples of apparent optical properties are water color and water visibility (Secchi depth); both of these change dramatically throughout the day, as the Sun traverses the sky. When discussing apparent optical properties it is often useful to specify the radiance **L** and the irradiance E. Radiance is the energy per unit time (power) per unit area emitted from a surface in a given solid angle and in a given direction,

$$\mathbf{L} = \frac{d^2\Phi}{d\Omega dA\cos\theta}\hat{\mathbf{\Omega}}, \tag{1.8}$$

where Φ is the power, A is the area of the emitting surface and the radiance is measured in W/m^2sr. Irradiance is the radiant energy illuminating a given surface per unit time per unit area,

$$E = \frac{\Phi}{A}, \tag{1.9}$$

and is measured in W/m^2. The term field has many meanings in physics. When we are speaking of light within a cavity or a marine environment and use the term light field we will generally mean the radiance. In the cases in which we are describing the field at the wall of a cavity or at a detector surface we generally mean the irradiance. The term light field is used throughout marine optics and is generally interpreted according to the context.

2. Tools of the Trade

In this day and age of remote satellite sensing it is imperative that one understand the propagation of light through natural waters if one is to properly interpret satellite data. Satellites detect light that has been backscattered from the atmosphere, the ground surface, the water surface and throughout the water column. In order to solve the radiative transfer equation, one must know the initial radiance distribution, the absorption coefficient, and the volume scattering function. Recall that both the absorption coefficient and the volume scattering function are characteristics of the natural water as well as any material dissolved or suspended in the water. To validate the interpretation of satellite data these inherent optical properties must be measured locally. It is not a trivial matter to measure them. If one removes a sample from the ocean environment for a laboratory measurement, the results can change as particulates settle out of suspension or with the introduction of contaminants to the sample. The introduction of something as seemingly benign as a suspension of micro-air bubbles can distort conventional absorption measurements.[1] Therefore, it becomes necessary to make *in situ* measurements. Previous absorption meters have often been sensitive to scattering as well as absorption.[2] Some of the most interesting biological zones as well as the most sensitive environmental zones are rivers and shorelines. These environments can range from relatively low levels of absorption, ~0.005 m^{-1}, to levels of over 40 m^{-1} for both absorption and scattering.[3-5]

Several designs have been put forth to deal with these difficulties. The designs

tend to fall into three categories: those which try to capture the forward scattered light and reintroduce it into the sample without concern for the homogeneity of the light field; those which measure both the attenuation and some amount of the scattering; and finally those which use an integrating cavity to prevent losses due to scattering.

An example of the first category is the liquid core waveguide, LCW.[3] These devices use either total internal reflection or a reflective outer wall to guide the light through the medium. They lose the backscattered light as well as some of the light scattered near 90°. The forward scattered light, near 90°, is either outside the critical angle for waveguiding or can leak out through the water outflow port. Depending on the type of waveguide used, one must also be concerned that the optical path length varies depending on the volume scattering function of the sample.

In the second category, devices measure the attenuation of a collimated beam and then subtract from it an approximation of the scattered light. The devices usually rely on either the "magic angle" method for approximating the scattering or collecting the forward scattering via a reflective tube wall.[6-8] Both of these cases are somewhat distasteful and involve empirical modeling, based on assumed scattering and absorption characteristics of the sample. Thus, for example, in the "magic angle" approach, if something of interest does exist in the volume scattering function it will almost certainly be missed and the correction to obtain the absorption value will be wrong. This calibration method can yield measurements with negative absorption coefficients for dissolved materials.[1]

There have been very few *in situ* category three designs. One commercially available now, introduces the light into the cavity in an anisotropic manner.[9] In any cavity the light field will not be homogeneous or isotropic when the inverse of the absorption coefficient is of the order of the cavity diameter. This problem becomes even more pronounced when the light is introduced in a nonhomogeneous matter. Another complication arises because the cavity diameter is much larger than the input and exit ports for the medium, raising questions of sample integrity as one moves the device from one water zone to another.

Although our flow-through ICAM design also falls into this third category, it illuminates the integrating cavity with a homogeneous and isotropic field. It was Elterman[10] who suggested the use of an isotropic and homogeneous field, produced within an integrating cavity, to measure the absorption coefficient of samples independently of their scattering coefficient. Over twenty years later Pope et al.[11, 12] showed how to adapt this concept to obtain the most accurate measurements ever made of the absorption coefficient of water. In Fig. 2, the data from Pope et al.[12] clearly shows the harmonics of the O-H stretching and scissors vibrational modes.

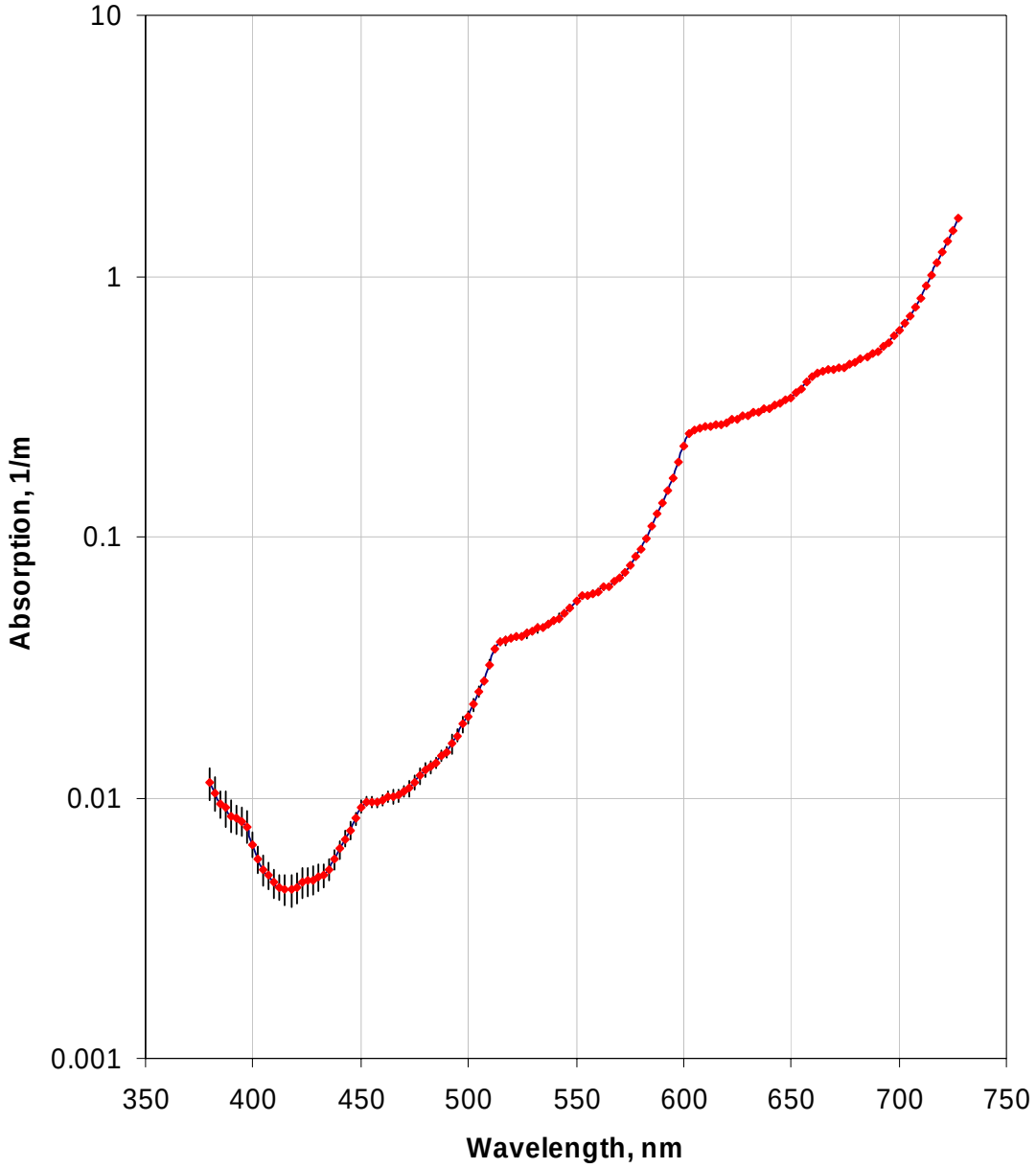

Fig. 2. Pope et al., absorption data of “pure” water.

Integrating cavities are powerful tools when assessing light fields. Their ability to gather light from all directions and integrate it into a single signal, independent of its original propagation and proportional to the total intensity, allows them a wide range of

applications: radiometry, spectroscopy, cosine illumination sources, close cavity coupling, etc. One of the primary ingredients in an integrating cavity is the Lambertian reflector. A Lambertian reflector reflects light proportional to the cosine of the reflected angle and independent of the angle of incidence, see Fig. 3.

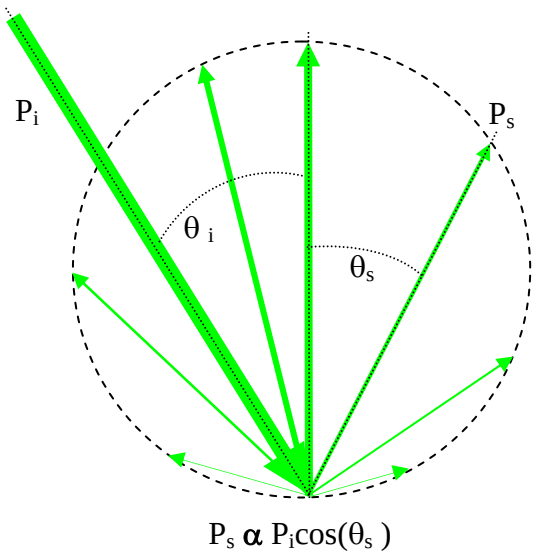

Fig. 3. Geometry of a Lambertian reflector. P_i is the incident power, P_s is the scattered power, θ_i is the incident angle, and θ_s is the scattering angle.

3. Monte Carlo Simulation of the Flow-Through Integrating Cavity Absorption Meter

The Monte Carlo simulations for the flow-through integrating cavity absorption meter (ICAM) were performed by Gray[13], and Gray et al.[14] The basic geometry of the ICAM consists of a quartz tube surrounded by two cylindrical diffuse reflectors separated by a small air gap, see Fig. 4. The uniform cross section of the flow-through tube allows for a smooth flow of water without concerns regarding trapping or mixing of different samples. The outer surface of the quartz tube is ground.

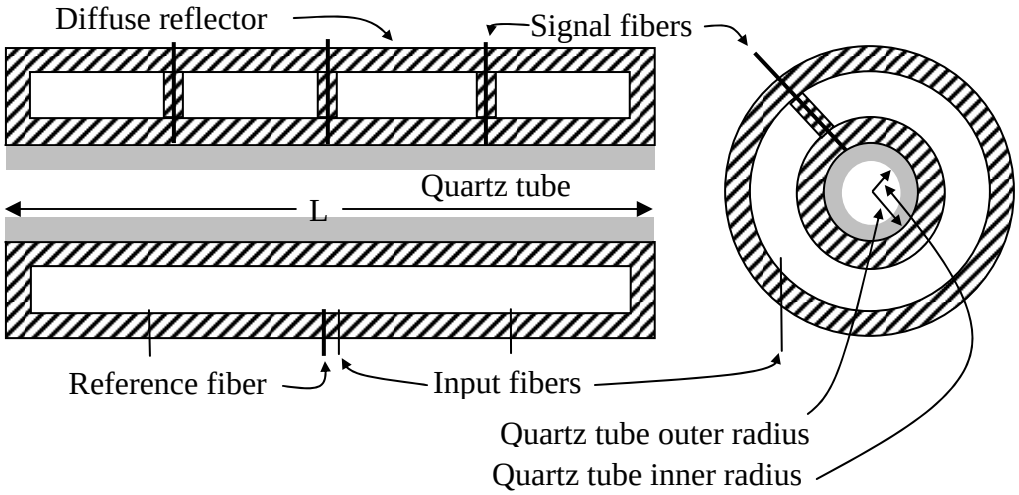

Fig. 4. The flow-through ICAM design.

The light is introduced into the small air gap between the two cylindrical diffuse reflectors. The light that is transmitted from this outer integrating cavity, through the

diffuse wall and into the inner cavity, produces an isotropic and homogeneous field in the inner cavity. A fiber optic cable samples the inner cavity's light field at the midpoint of the quartz tube. A reference signal is collected by a fiber optic cable located in the outer cavity. To obtain the raw absorption signal the inner cavity signal is divided by the reference signal. Gray normalized his signal by dividing the raw absorption signal by the signal achieved when the cavity is filled with an absorptionless fluid having an index of refraction equivalent to water. Although this is an impossible task in the lab, it is trivial in the Monte Carlo code. I will refer to this signal as the absorption signal for now and address experimental methods of calibration later. Gray used a 50 cm long tube with a radius of 15 mm as his standard geometry. He fit the absorption signal as follows

$$\chi = \frac{\text{Flux(a)}}{\text{Flux(a = 0)}} = \frac{\text{p}}{\text{a} - \text{q}}, \tag{1.10}$$

where p and q are fitting parameters and a is the absorption coefficient. The response of the standard geometry ICAM is shown in Fig. 5.

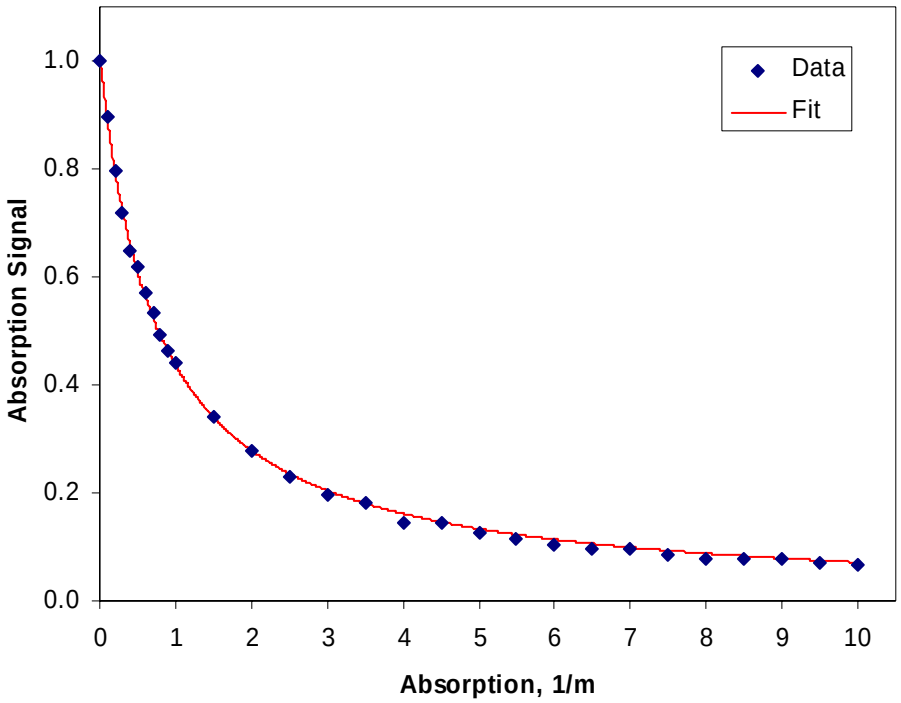

Fig. 5. Monte Carlo simulation of the ICAM.

In Fig. 6 one can see the response of the ICAM as a function of the radius of the tube. At large radius, end effects become pronounced and the device decreases in sensitivity as more light escapes out the ends. As the radius decreases the optical path length also decreases. The optimal radius for signal discrimination with a 50 cm long tube is about 1 cm. In Fig. 7, the detector flux is plotted vs. the length of the cavity. One can see that for a given diameter, a longer tube will always provide greater sensitivity. Of course the goal is not to have the greatest sensitivity possible, but the most sensitive instrument that is practical in the environment to be used. Gray et al. suggested a 50 cm tube is sufficiently sensitive while still short enough to use in natural

waters.

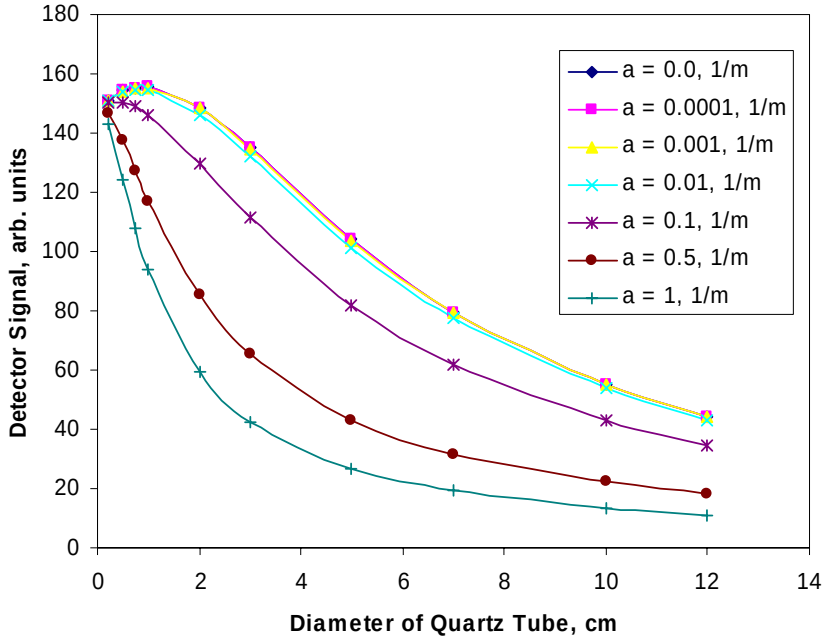

Fig. 6. Monte Carlo simulation of the ICAM response vs. diameter.

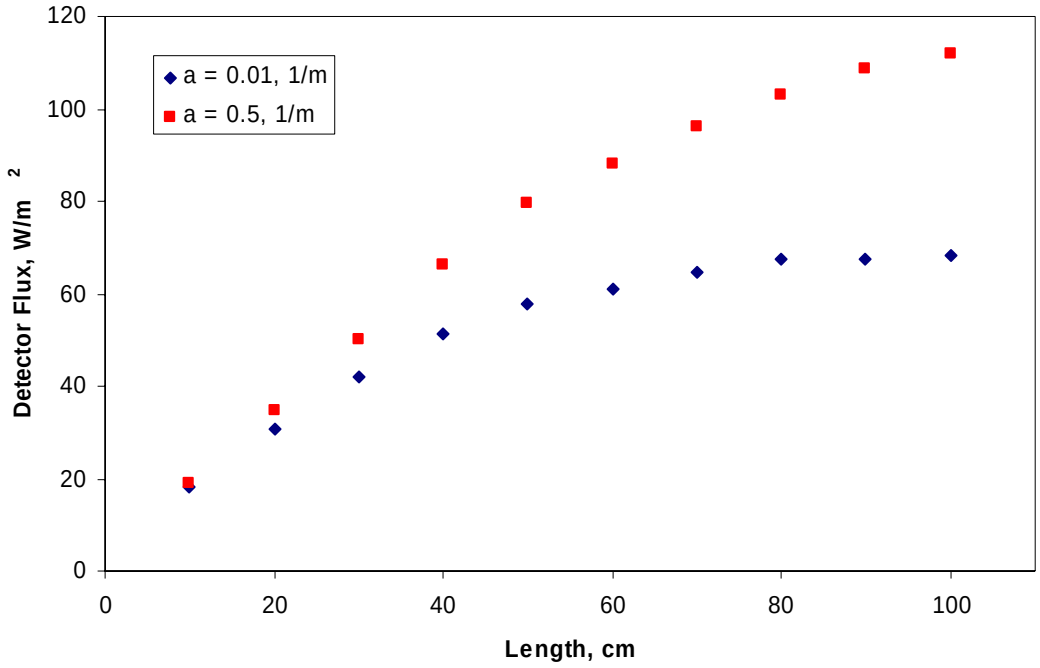

Fig. 7. Monte Carlo simulation of the ICAM response vs. length.

In Fig. 8, the percentage of the power that is lost through the diffuse reflector, that which is lost out the open ends of the tube, and that which is absorbed in the medium is plotted as a function of the absorption coefficient. Most of the power is lost through the ICAM walls or lost out the ends of the device at low absorptions. At high absorption most of the power is absorbed by the medium, as expected. The medium's fraction of the power absorbed does not approach one, instead it approaches 0.96. The reason is that the quartz tube waveguides a certain amount of light out the end of the tube without it ever having sampled the medium.

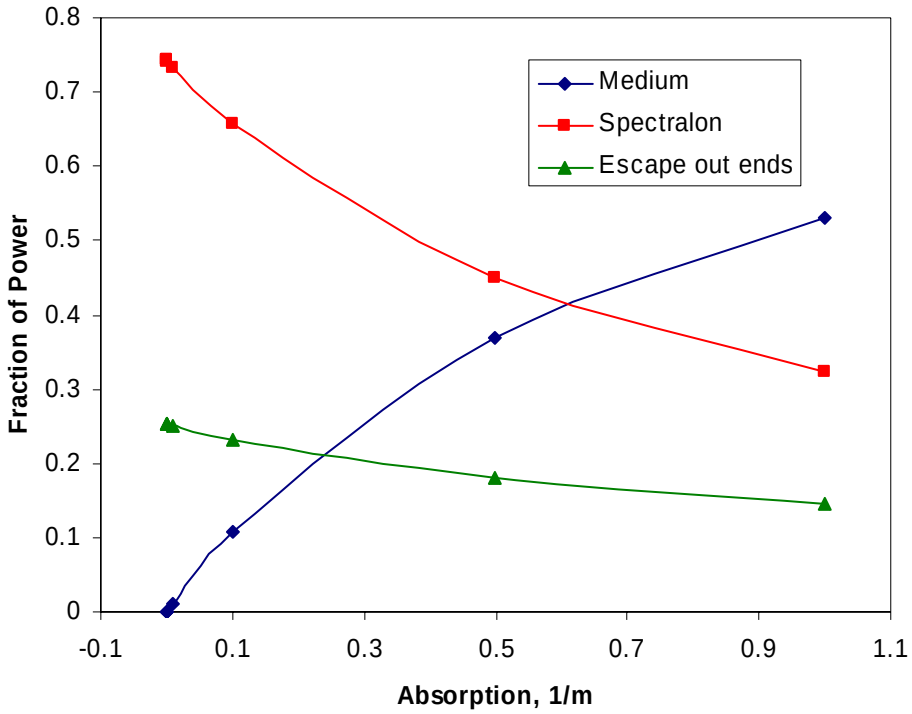

Fig. 8. Monte Carlo results for the fraction of power absorbed by the medium, lost via the Spectralon wall, and escaping out the ends of the tube.

The detector's response as a function of the scattering coefficient of the medium is shown in Fig. 9. The results are shown for two g values of the Henyey-Greenstein phase function, 0 (isotropic scattering) and 0.95 (highly forward peaked as is the case with natural waters). The question naturally arises, why does the forward peaked scattering have such a small impact on the absorption measurements? As Gray pointed out, a photon headed toward the open end of the tube or to the opposite side of the tube will, after scattering, be most probable to continue in the same general direction thus having little impact on the optical path length or its tendency to escape out the end of the tube. On the other hand, if the scattering is isotropic it is very likely that its direction

and hence its path length will change, thus we see a markedly different impact for the g = 0 case, see Fig. 10. In practice, scattering in natural waters is always highly peaked in the forward direction.

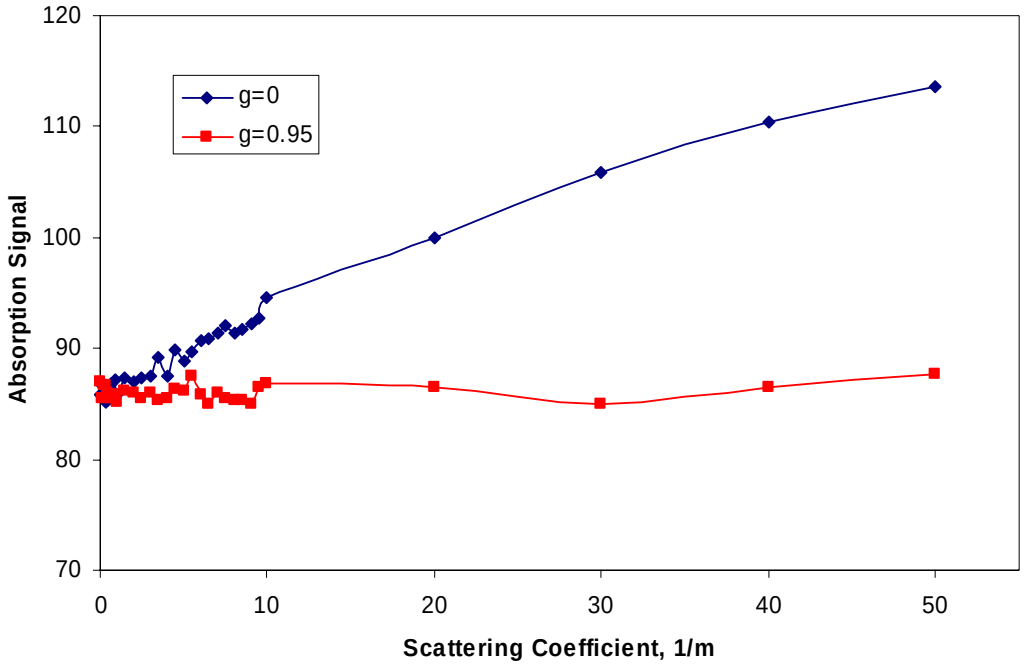

Fig. 9. Monte Carlo simulation of the ICAM response vs. the scattering coefficient.

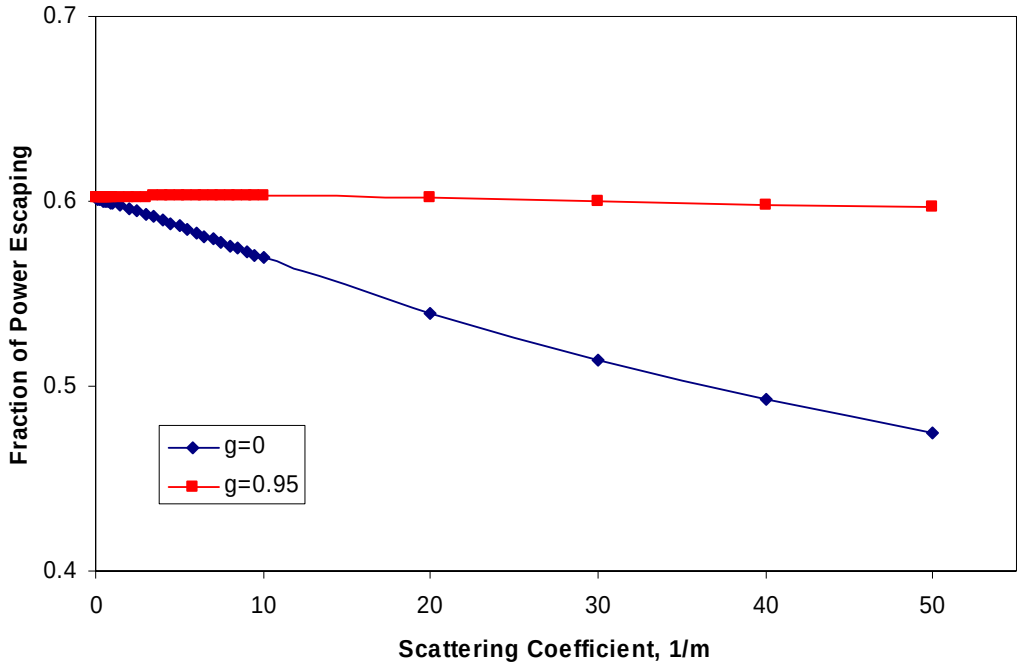

Fig. 10. Gray et al. Monte Carlo results for the fraction of power escaping out the ends of the ICAM as a function of the scattering coefficient for both highly forward peaked scattering, g=0.95, and isotropic scattering, g=0.

.

CHAPTER II

INTEGRATING CAVITIES I, DYNAMICS*

1. The Time Response of an Integrating Cavity

Integrating cavities, as mentioned in the introduction, are used in several areas of optics, including: radiometry, photometry, spectroscopy and materials characterization. Integrating cavities generally use cw illumination. Provided an integrating cavity has a wall reflectivity near unity, the decay of a temporally short pulse in an empty cavity can provide a measure of the absolute reflectivity of the cavity wall. Once the reflectivity is known, the integrating cavity can be used to make highly sensitive measurements of weak absorption by monitoring the decaying field of a temporally short pulse in the presence of a weakly absorbing medium. In the derivation to determine the temporal response of an integrating cavity the following variables are defined:

E = irradiance on the wall of the cavity, i.e. the radiation energy incident on the wall per unit area per unit time (W/m^2)

ρ = average reflectivity of the Lambertian surface of the cavity (assumed constant and independent of the angle of incidence), $0 \leq \rho \leq 1$

---

*Reprinted with permission from "Integrating cavities - temporal response," by E. S. Fry, J. A. Musser, G. W. Kattawar, P. W. Zhai, 2006. Applied Optics, accepted for Publication

τ = time constant of the cavity ≡ time for irradiance to decrease to 1/e

n = average number of reflections in time τ

$\bar{d}$ = average distance traveled between successive reflections at the cavity wall

c = speed of light

t = time

$\bar{t}$ = average time between reflections.

The average time between reflections is given by

$$\bar{t} = \frac{\bar{d}}{c}. \tag{2.1}$$

The following derivation is the widely accepted time response of an integrating cavity;[16,17] it is reproduced here based on a slide presentation by Arecchi.[18] Assume the irradiance E_I incident on the cavity walls decays exponentially

$$E_I(t) = E_0 e^{-t/\tau} \tag{2.2}$$

where E_0 is the irradiance incident on the cavity walls at time t = 0. At time t the irradiance leaving the wall is

$$E_L(t) = \rho E_0 e^{-t/\tau}. \tag{2.3}$$

During a time t equal to the decay constant τ there will be n reflections in which the irradiance E_L leaving the cavity wall after each reflection is the incident irradiance multiplied by the reflectivity ρ. There are two choices one could take for the zero of time: at the instant of the first reflection, or such that the first reflection occurs at $\bar{t}$.

In the first case we consider the zero of time to be at the instant of the first reflection, thus at the $(n+1)^{th}$ reflection, $t = n\bar{t} = \tau$, and

$$E_I(\tau) = E_0\rho^n, \qquad E_L(\tau) = E_0\rho^{n+1}. \tag{2.4}$$

From Eqs. (2.2) and (2.3), the irradiances at $t = \tau$ are

$$E_I(\tau) = E_0 e^{-1}, \qquad E_L(\tau) = \rho E_0 e^{-1}. \tag{2.5}$$

Recalling that $n\bar{t} = \tau$ and combining Eqs (2.4) and (2.5) yields

$$n = -\frac{1}{\ln\rho}, \qquad \tau_1 = -\frac{1}{\ln\rho}\bar{t} = -\frac{1}{\ln\rho}\frac{\bar{d}}{c}. \tag{2.6}$$

The subscript 1 has been added to τ to signify this is the τ from the first case. If the reflectivity $\rho = 0$, Eq. (2.6) gives $n = 0$ and $\tau_1 = n\bar{t} = 0$. Physically this is reasonable. If at time $t = 0$ the photons are all incident on the wall and the reflectivity is zero, the field will immediately drop to zero. For ρ near unity both n and τ_1 are large. Eq. (2.6) is the standard result found in the literature for the time constant of an integrating cavity.[16,17]

One can gain further insight by not assuming an exponential solution. A Taylor series expansion of $E_I(t+\bar{t})$ about the time t yields

$$E_I(t+\bar{t}) = E_I(t) + \sum_{k=1}^{\infty}\frac{\bar{t}^k}{k!}\frac{d^k E_I(t)}{dt^k}. \tag{2.7}$$

Introducing a change of variables $\xi = t/\bar{t}$, Eq. (2.7) can be rewritten as

$$E_I(t+\bar{t}) = E_I(t) + \sum_{k=1}^{\infty}\frac{1}{k!}\frac{d^k E_I(t)}{d\xi^k}. \tag{2.8}$$

Recall that the amount of light lost at each instant is the irradiance, hitting the cavity wall at that instant, multiplied by ρ - 1. Thus, $E_I(t+\bar{t}) - E_I(t) = E_I(t)[\rho - 1]$, and Eq. (2.8) becomes

$$\sum_{k=1}^{\infty} \frac{1}{k!} \frac{d^k E_I(t)}{d\xi^k} + E_I(t)(1-\rho) = 0 . \tag{2.9}$$

Notice that Eq. (2.9) is a homogeneous infinite order differential equation with constant coefficients and suggests solutions of the form $e^{\gamma\xi}$. Substituting this into Eq. (2.9) yields

$$\sum_{k=1}^{\infty} \frac{1}{k!} \gamma^k + (1-\rho) = 0 . \tag{2.10}$$

This equation is

$$e^{\gamma} - \rho = 0 . \tag{2.11}$$

Thus the solution to Eq. (2.9) is

$$E_I(t) = E_0 e^{\gamma t/\bar{t}} = E_0 e^{t \ln \rho/\bar{t}} . \tag{2.12}$$

Recall that $E_I(t) = E_0 e^{-t/\tau}$, thus we have

$$\tau = -\frac{\bar{t}}{\ln \rho}, \tag{2.13}$$

which is the same as that derived earlier in Eq. (2.6).

In the second case we pick t = 0 such that the average first reflection occurs at the time $\bar{t}$. Thus the n^{th} reflection occurs at $t = n\bar{t} = \tau$ and

$$E_I(\tau) = E_0 \rho^{n-1}, \qquad E_L(\tau) = E_0 \rho^n . \tag{2.14}$$

Combining Eqs. (2.14) and (2.5), which still holds, we have

$$n = 1 - \frac{1}{\ln \rho}, \qquad \tau_2 = \left(1 - \frac{1}{\ln \rho}\right) \bar{t} = \left(1 - \frac{1}{\ln \rho}\right) \frac{\bar{d}}{c}, \tag{2.15}$$

for both E_I and E_L, with τ_2 distinguishing this as the second case. Clearly τ_1 differs from τ_2. In the second case, when the reflectivity $\rho = 0$ Eq. (2.15) gives $n = 1$ and $\tau_2 = \bar{t}$. This too is reasonable. At time $t = 0$ the photons must travel an average time $\bar{t}$ before hitting the cavity wall, thus $\tau_2 \approx \bar{t}$. For ρ near unity n will be large and Eqs. (2.6) and (2.15) will have negligible differences.

To resolve whether Eq. (2.6) or Eq. (2.15) is most appropriate, Fry et al.[15] carried out Monte Carlo simulations of the decay of the irradiance in an integrating cavity. They performed the simulations for two different cases. In the first case, the cavity wall was given a reflectivity of near unity ($\rho = 0.9999$). The photons were started from random locations throughout the cavity and with initial directions to insure a homogeneous and isotropic field. A detector on the wall of the cavity measured the fractional energy it received (the total number of photons it received divided by the total number of photons processed) as a function of the total distance S traveled by the photons. The cavity radius was unity. The simulation was run until the initial transients stabilized; this point was chosen at $S = 50$. At this moment the wall reflectivity was changed from $\rho = 0.9999$ to the value of interest and the decay of the radiation field was monitored. In this manner, the true behavior of the cavity as a function of reflectivity could be determined.

The results of the first simulation are shown in Fig. 11. One can see a signal indicative of a homogeneous isotropic field just prior to $S = 50$. For $\rho = 0$ one sees the

irradiance becomes zero after one cavity diameter (S = 52, diameter = 52 - $50_{(\text{startup distance})}$). This is expected as this is the farthest distance a photon can travel before striking the wall where it is absorbed. This curve is not exponential, but parabolic. Even with $\rho \neq 0$ the decay is not immediately exponential but requires a few wall collisions before it follows an exponential decay. The Monte Carlo time constants τ_{MC} were determined by fitting the decay after s = 52.

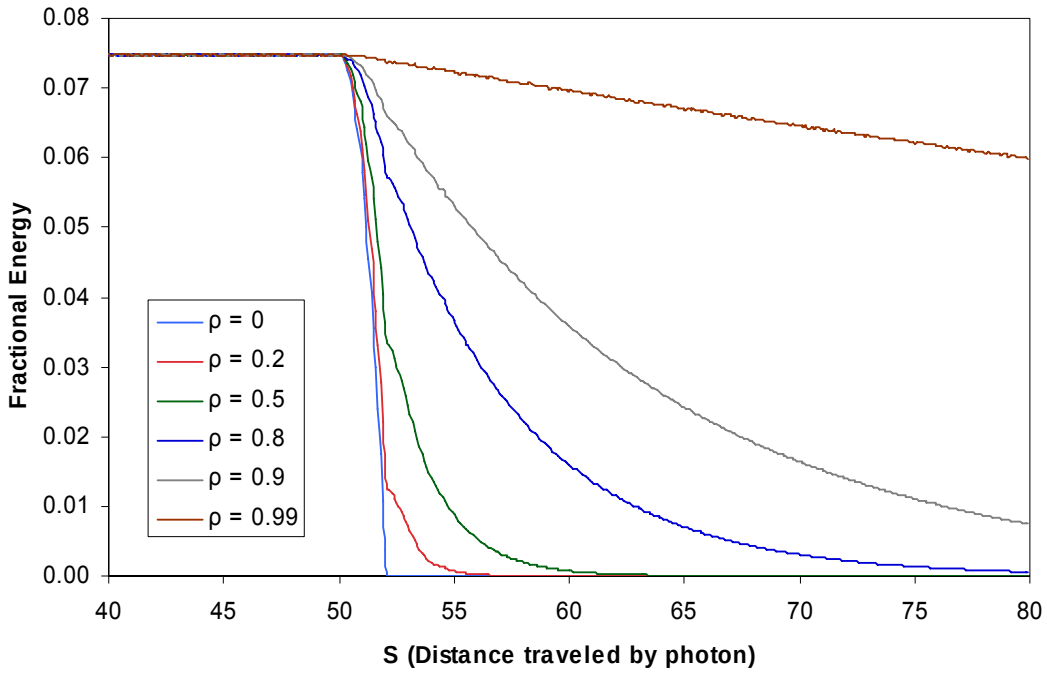

Fig. 11. Monte Carlo simulation for the decay of the radiation in an integrating cavity.

These time constants are compared to those calculated from Eqs. (2.6) and (2.15) for several cavity reflectivities, see Table 1. One will notice that for high reflectivities the agreement between all three is quite good indicating that the assumption of an

exponential decay is appropriate. As the reflectivity decreases from unity so does the agreement between the time constants. Notice that $c\tau_1 \leq c\tau_{MC} \leq c\tau_2$ for all $\rho > 0$. Further, one can see that case 1 provides much better agreement with the Monte Carlo simulation. One should be cautious regarding the exponential decay assumption. Clearly it was shown to be valid with the Monte Carlo simulation; however, the initial conditions chosen for the simulation have a subtle link to the exponential decay assumption. The initial conditions were chosen such that the radiation field was homogeneous and isotropic. Just how critical is this condition?

Table 1. A comparison of the decay constants from case 1 and 2 to the Monte Carlo simulation.

ρ	$c\tau_{MC}$	$c\tau_1$	Case 1 Error	$c\tau_2$	Case 2 Error
0.0	0.544	0.000	100%	1.333	145.1%
0.20	0.902	0.828	-8.2%	2.162	139.7%
0.50	2.001	1.924	-3.9%	3.257	62.8%
0.80	6.056	5.975	-1.3%	7.309	20.7%
0.90	12.738	12.655	-0.65%	13.998	9.8%
0.99	132.75	132.67	-0.06%	134.00	0.94%

In the second Monte Carlo simulation the conditions were more akin to what might be found in an experimental setup. In this case a pulse of photons with a Lambertian distribution over 2π steradians was launched into the cavity from a point on the cavity wall. The detector was located 90° from the launching point. The results for the second simulation are shown in Fig. 12. There is a sharp peak at $s = 2^{1/2}$ which is the

most direct path for a photon to travel to the detector. The width of this peak is due to the width of the detector. A finite detector produces a slight spread in the paths which can reach the detector directly from the point source where the light was injected.

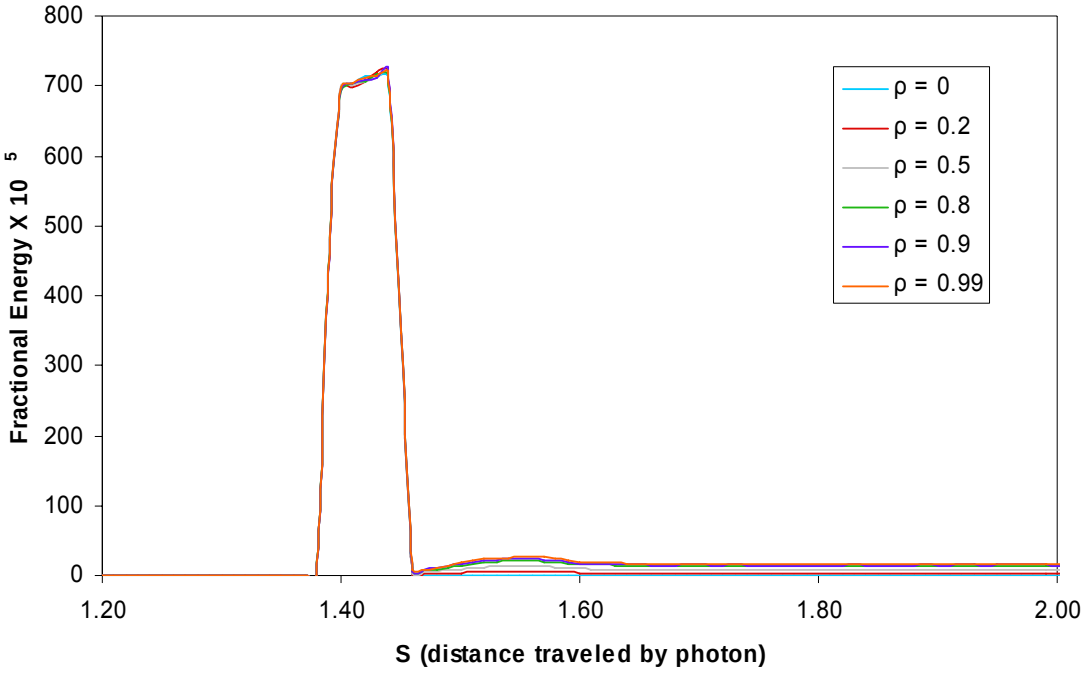

Fig. 12. Monte Carlo simulation of the decay of an injected pulse, S = 1.2 to 2.0.

There is a secondary weaker peak at s = 3.7, see Fig. 13. This is the farthest distance a photon can travel and reach the detector with only one reflection. In a few more reflections the signal smoothes to a near exponential curve, see Fig. 14. This is indicative of a homogeneous and isotropic radiation field having been established in the cavity. The experimentalist should keep these nuances in mind, we will return to them

later. Once the detected energy began to decay exponentially, it was fitted to obtain the decay constant $c\tau_{MC}$.

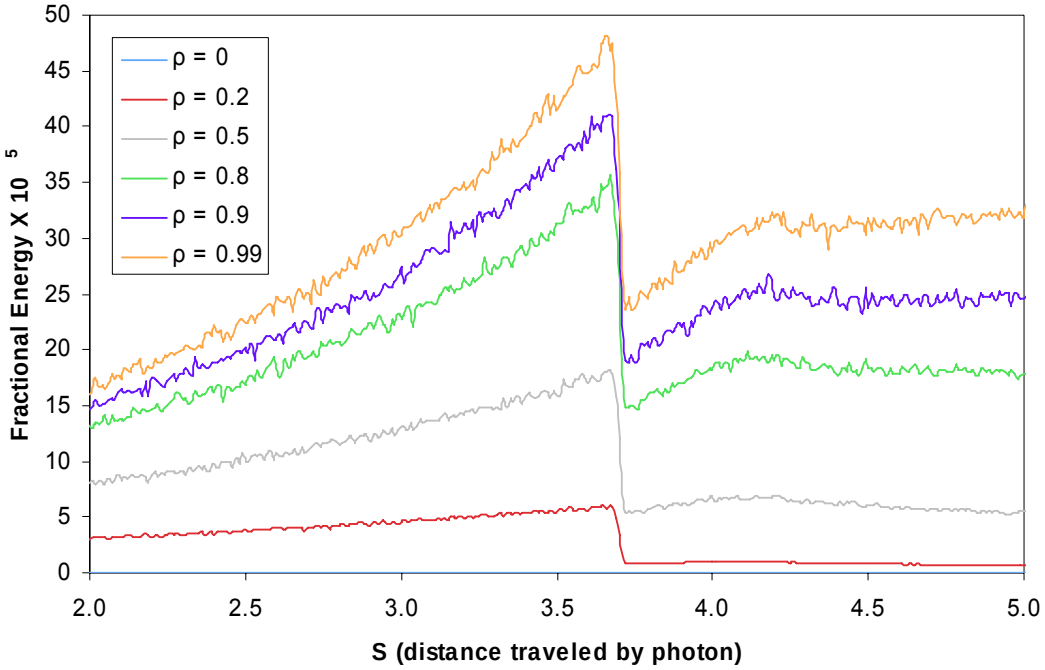

Fig. 13. Monte Carlo simulation of the decay of an injected pulse, S = 2.0 to 5.0.

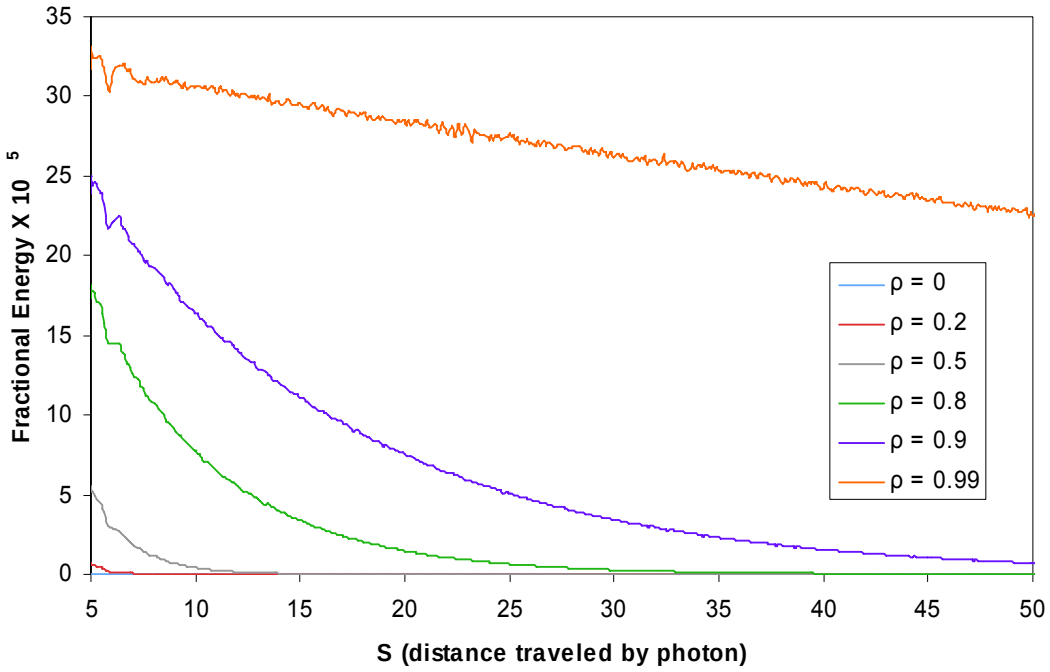

Fig. 14. Monte Carlo simulation of the decay of an injected pulse, S = 5 to 50.

In Table 2, the new Monte Carlo decay constants are compared to those for Eqs. (2.6) and (2.15). The results agree well for reflectivities near unity and become worse as ρ decreases. One will notice that the decay constants of the Monte Carlo simulation for the injected pulse are almost identical to those of the Monte Carlo simulation for the uniform field. This is an artifact of the choice to fit the decay constant after the simulation had approached an exponential decay. In other words, once the second simulation had achieved a uniform field (the condition of the first simulation) the decay constant was determined. At low reflectivities this condition is never met and the Monte Carlo simulations differ. This shouldn't be too surprising since at low reflectivities the cavity does not decay exponentially, nor should it be expected to. What one really

measures at low reflectivities is the geometric relationship between the location where the light pulse was introduced and the available paths to the detector for the given number of reflections. This is seen in the Monte Carlo data as multiple peaks in the signal. This effect is actually seen in all of the data, regardless of ρ. It is the reason for waiting for the energy to begin to decay exponentially before fitting it to obtain the time constant.

The following points should be taken away from this analysis. The manner in which the light is launched into and detected in the cavity is critical to the initial response of the cavity. The assumed exponential decay of the cavity is a valid assumption provided $\rho \geq 0.5$ and it is nearly identical to the results from the Monte Carlo simulations as the reflectivity approaches unity.

Table 2. Monte Carlo simulation results for the decay constants of the injected pulse.

ρ	$c\tau_{MC}$	$c\tau_1$	Case 1 Error	$c\tau_2$	Case 2 Error
0.2	0.892	0.828	-7.1%	2.162	142%
0.5	2.000	1.924	-3.8%	3.257	63.0%
0.8	6.056	5.975	-1.3%	7.310	20.7%
0.9	12.740	12.655	-0.67%	13.99	9.8%
0.99	132.75	132.67	-0.06%	134.00	0.94%

2. The Average Distance Between Reflections in a Spherical Shell

Cavity geometry, as mentioned in the above discussion, is critical to the temporal response of an integrating cavity. One of the important features used to describe an integrating cavity's geometry is the average distance $\bar{d}$ that a photon travels between reflections. Fig. 15 shows the cross-section of a spherical shell with inner radius R_1 and outer radius R_2. It is convenient to calculate $\bar{d}$ in three separate regions I, II, and III as depicted in the diagram.

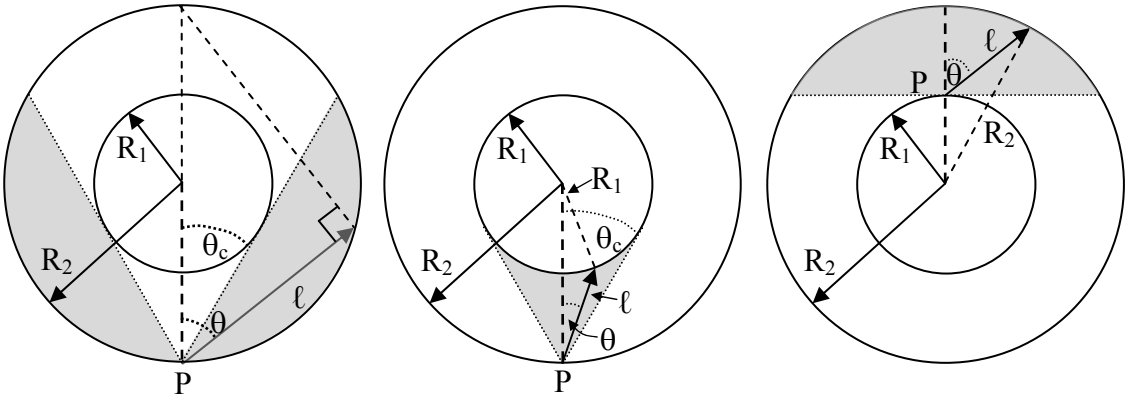

Region I Region II Region III

Fig. 15. Regions I, II and III for the calculation of $\bar{d}$ for a spherical shell.

The normalized probability function for photons emitted with a Lambertian distribution, from a wall surface, is

$$p(\mu,\phi)d\mu d\phi = \frac{\mu d\mu d\phi}{\pi}, \quad \text{note} \int_0^{2\pi}\int_0^1 \frac{\mu d\mu d\phi}{\pi} = 1, \tag{2.16}$$

where $\mu = \cos\theta$ and the point of emission is taken as the origin of the spherical coordinate system. Consider a unit area P from which photons are reflected, in a Lambertian manner, into a full 2π steradians. In region I the reflections are restricted to angles θ such that $\theta_c \le \theta \le \pi/2$ where θ_c is the angle formed by the normal at point P and a ray originating from point P and tangent to the inner circle. In region I we have:

$$\langle \ell \rangle_I = \bar{d}_I = \int_0^{2\pi} \int_0^{\mu_c} \frac{\ell \mu d\mu d\phi}{\pi}, \tag{2.17}$$

and from Fig. 15, we see that for region I

$$\ell = 2R_2 \cos\theta = D_2 \mu, \tag{2.18}$$

where $D_2=2R_2$ is the diameter of the outer cavity. Solving Eq. (2.17) yields,

$$\langle \ell \rangle_I = \frac{2D_2 \mu_c^3}{3}. \tag{2.19}$$

In region II, θ is restricted to $0 \le \theta \le \theta_c$ and using the law of cosines ($R_1^2 = R_2^2 + \ell^2 - 2R_2 \ell \cos\theta$) we find

$$\ell = R_2 \left(\mu - \sqrt{(\mu^2 - 1) + \beta^2} \right), \tag{2.20}$$

where $\beta = R_1/R_2$.

Substituting Eq. (2.20) into Eq. (2.17) with ϕ running from 0 to 2π and μ running from μ_c to 1 yields,

$$\langle \ell \rangle_{II} = \frac{D_2}{3} \left(1 - \mu_c^3 - \beta^3 \right). \tag{2.21}$$

Combining the results for region I and II yields,

$$\langle \ell \rangle_{I+II} = \frac{D_2}{3}\left(1 + \mu_c^3 - \beta^3\right). \tag{2.22}$$

We now consider photons reflected from a point Q on the inner sphere, see Fig. 15. In region III θ is restricted to $0 \le \theta \le \pi/2$ and again using the law of cosines $\left(R_2^2 = \ell^2 + R_1^2 - 2\ell R_1 \cos(180 - \theta)\right)$ we have

$$\ell = R_2\left(-\mu\beta + \sqrt{\beta^2\left(\mu^2 - 1\right) + 1}\right). \tag{2.23}$$

Subtituting Eq. (2.23) into Eq. (2.17) with ϕ from 0 to 2π and θ from 0 to $\pi/2$ yields,

$$\langle \ell \rangle_{III} = \frac{D_2}{3}\left(-\beta + \frac{1 - \left(1 - \beta^2\right)^{3/2}}{\beta^2}\right) = \frac{D_2}{3}\left(-\beta + \frac{1}{\beta^2}\left(1 - \mu_c^3\right)\right). \tag{2.24}$$

To combine the average distances from region I, II, and III they must be weighted by the probability of a reflection from their respective surfaces, that is the probability is equal to the fraction of the region's surface area to the cavity's whole surface area. Thus region I + II must be weighted by $1/(1 + \beta^2)$ and region III by $\beta^2/(1 + \beta^2)$, and we have,

$$\langle \ell \rangle_{I+II+III} = \bar{d} = \frac{2D_2}{3}\left(\frac{1 - \beta^3}{1 + \beta^2}\right). \tag{2.25}$$

In the case of $\beta = 0$, $\bar{d} = 2D_2/3$ which is the well known case for a spherical cavity. Notice that Eq. (2.25) reduces to 4V/S where V is the volume of the cavity and S is the total surface area of the cavity.

3. The Average Distance Between Reflections in a Right Circular Cylinder

Consider a right circular cylinder of diameter D and height H, see Fig 16. The cylinder's axis lies along the z-axis of a cylindrical coordinate system. Consider any two walls of the cavity labeled i and j (they may be the same wall). Take the source point P located on wall i and the end point Q located on wall j.

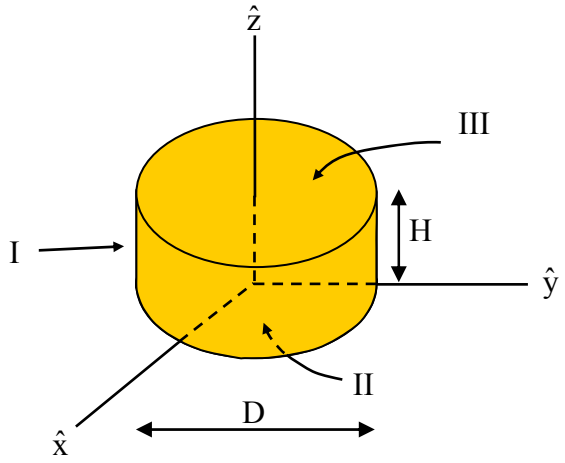

Fig. 16. Regions I, II and III for the calculation of $\bar{d}$ for a right circular cylinder.

The unit normal to each wall is $\hat{n}_{iP}$ and $\hat{n}_{jQ}$. The vector from P to Q is **r**. With respect to P, an element of area dA_j at Q on wall j subtends a solid angle

$$\frac{dA_j}{r^2}\frac{\left|\hat{n}_{jQ}\cdot\vec{r}\right|}{r}. \tag{2.26}$$

For a Lambertian surface, the differential probability of emission from point P in the direction **r** is

$$\frac{\left|\hat{n}_{iP}\cdot\vec{r}\right|}{r}. \tag{2.27}$$

Thus the differential probability dp_j of reflection from P to Q in the solid angle dA_j is

$$dp_j = \frac{1}{\pi}\frac{dA_j}{r^2}\frac{\left|\hat{n}_{jQ}\cdot\vec{r}\right|}{r}\frac{\left|\hat{n}_{iP}\cdot\vec{r}\right|}{r}, \tag{2.28}$$

where the normalization is provided by $1/\pi$. The Lambertian weighted distance from P to Q averaged over all points Q on wall j is given by

$$\bar{d}_{Pj} = \iint_j r\,dp_j = \frac{1}{\pi}\iint_j \frac{1}{r}\frac{\left|\hat{n}_{jQ}\cdot\vec{r}\right|}{r}\frac{\left|\hat{n}_{iP}\cdot\vec{r}\right|}{r}dA_j. \tag{2.29}$$

Since wall i is assumed to be uniformly illuminated, $\bar{d}_{Pj}$ can be averaged over it using the differential probability $dp = dA_i/A_i$. Therefore, the result for the average Lambertian weighted distance a photon travels between wall i and wall j is

$$\bar{d}_{i\to j} = \frac{1}{A_i}\iint_i \bar{d}_{Pj}dA_i = \frac{1}{\pi A_i}\iint_i dA_i \iint_j \frac{1}{r}\frac{\left|\hat{n}_{jQ}\cdot\vec{r}\right|}{r}\frac{\left|\hat{n}_{iP}\cdot\vec{r}\right|}{r}dA_j. \tag{2.30}$$

Since the Lambertian cosine factors are always positive the directions of the normals are chosen such that the dot products are always positive quantities. The unit vectors are $\hat{n}$, $\hat{l}$ and $\hat{k}$; the corresponding vector components are represented by $\{\rho, \varphi, z\}$. There are three surfaces I, II, and III from which light can reflect. As in the case of the spherical shell, the associated surface areas of the regions are needed to determine the probability of a photon originating from the given region. Their areas are

$$A_I = \pi DH; \qquad A_{II} = A_{III} = \frac{\pi D^2}{4}. \tag{2.31}$$

A photon can be reflected from the cavity wall in three unique ways from region I to region I, from region I to region II and from region II to region III.

Consider $\bar{d}_{I\to I}$. The source point for such a reflection is $\{R,0,z_0\}$ where we are free to choose $\varphi_0=0$ due to symmetry. The end point is $\{R, \varphi, z\}$. The normal to the cavity wall at the source and end points is $\hat{n}_1=\{1,0,0\}$, see Fig. 17. The components in the directions $\hat{n}$, $\hat{l}$ and $\hat{k}$ of the vector from the source to the end point are given by $2R \sin^2 \varphi/2$, $2R \sin \varphi/2 \cos \varphi/2$, and $(z-z_0)$, respectively. Therefore, $\mathbf{r_1} = \{R(1- \cos \varphi), R\sin \varphi, z-z_0\}$ and its magnitude is $r_1 = \sqrt{2R^2(1-\cos\varphi)+(z-z_0)^2}$. The Lambertian cosine factor as well as the component of infinitesimal area dA_I perpendicular to $\mathbf{r_I}$ is $\left|\hat{n}_I \cdot \vec{r}_1\right|/r_1$,

$$\frac{\left|\hat{n}_I \cdot \vec{r}_I\right|}{r_I} = \frac{R(1-\cos\varphi)}{\sqrt{2R^2(1-\cos\varphi)+(z-z_0)^2}}. \tag{2.32}$$

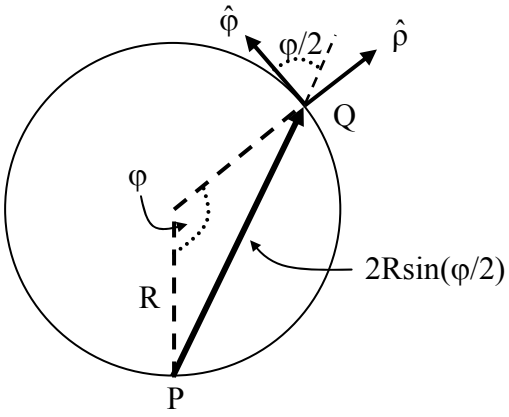

Fig. 17. Cross-sectional view of a cylindrical cavity at a height of z_o. The source point P is located on the wall at a distance of z_o above the base. The end point Q is also located on the wall; however, it is at a distance of z above the base.

Introducing the normalized coordinates $\zeta = \frac{z}{H}$ and $\nu = \frac{z_0}{H}$, where $0 \le \zeta, \nu \le 1$, and the dimensionless parameter $\alpha = \frac{2R}{H} = \frac{D}{H}$ yields $r_1 = H\sqrt{\frac{1}{2}\alpha^2(1-\cos\varphi) + (\zeta-\nu)^2}$.

Thus,

$$\bar{d}_{PI} = \frac{R^3}{\pi H^2}\int_0^{2\pi} d\varphi \int_0^1 d\zeta \frac{(1-\cos\varphi)^2}{\left(\frac{1}{2}\alpha^2(1-\cos\varphi) + (\zeta-\nu)^2\right)^{3/2}}. \tag{2.33}$$

Averaging over all source points P on the region I wall yields $\bar{d}_{I\to I}$,

$$\bar{d}_{I\to I} = \frac{1}{A_I}\int_0^H \bar{d}_{PI}\, 2\pi R dz_0 = \frac{1}{H}\int_0^H \bar{d}_{PI} dz_0 = \int_0^1 \bar{d}_{PI} d\nu, \tag{2.34}$$

giving

$$\bar{d}_{I\to I} = \frac{R^3}{\pi H^2}\int_0^{2\pi} d\varphi \int_0^1 d\zeta \int_0^1 d\nu \frac{(1-\cos\varphi)^2}{\left(\frac{1}{2}\alpha^2(1-\cos\varphi)+(\zeta-\nu)^2\right)^{3/2}}. \tag{2.35}$$

Integrating over ζ and ν yields

$$\bar{d}_{I\to I} = \frac{D}{\pi}\int_0^{2\pi} \sin^2\frac{\varphi}{2}\sqrt{1+\alpha^2\sin^2\frac{\varphi}{2}}\,d\varphi - \frac{8D\alpha}{3\pi} \tag{2.36}$$

for the average distance traveled by photons reflecting off the cylinder wall and hitting elsewhere on the cylinder wall. The integral in Eq. (2.36) is a hypergeometric function, but for our purposes will be evaluated numerically.

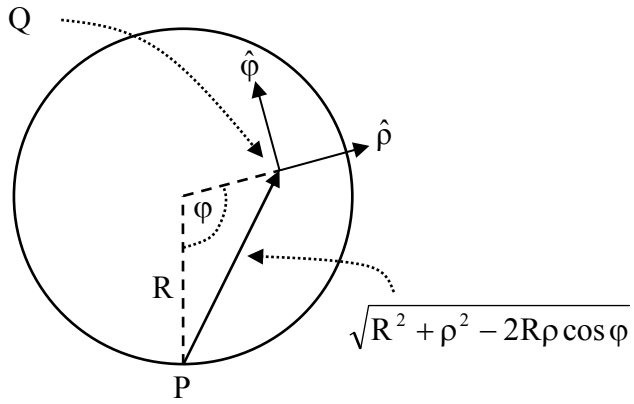

Fig. 18. Base of the cylindrical cavity. The source point P is on the wall a distance z_o above the base. The end point Q is on the base (z=0) a distance ρ from the cylinder axis.

Consider $\bar{d}_{I\to II}$, from a source point on the cylinder wall to an end point on the base of the cylinder, see Fig. 18. Notice that $\bar{d}_{I\to II}$ is equivalent to $\bar{d}_{I\to III}$. The source point is located at $\{R,0,z_0\}$; the end point is at $\{\rho, \varphi,0\}$. The normals are $\hat{n}_I = \{1,0,0\}$ and $\hat{n}_{II} = \{0,0,-1\}$. The vector, from the source point to the end point, in the direction of $\hat{n}$, $\hat{l}$ and $\hat{k}$ is $\vec{r}_{II} = (R - \rho\cos\varphi, \rho\sin\varphi, -z_0)$; its magnitude is $r_{II} = \sqrt{R^2 + \rho^2 - 2R\rho\cos\varphi + z_0^2}$. Thus the Lambertian cosine factor is

$$\frac{|\hat{n}_I \cdot \vec{r}_{II}|}{r_{II}} = \frac{R - \rho\cos\varphi}{\sqrt{R^2 + \rho^2 - 2R\rho\cos\varphi + z_0^2}} \tag{2.37}$$

and the component of infinitesimal area dA_{II} on the bottom face that is perpendicular to $\mathbf{r_{II}}$ is

$$\frac{|\hat{n}_{II} \cdot \vec{r}_{II}|}{r_{II}} = \frac{z_0}{\sqrt{R^2 + \rho^2 - 2R\rho\cos\varphi + z_0^2}}. \tag{2.38}$$

Again we introduce normalized coordinates $\eta = \frac{\rho}{R}$ and $\nu = \frac{z_0}{H}$, where $0 \le \eta, \nu \le 1$ and $\alpha = \frac{2R}{H} = \frac{D}{H}$. Thus $r_{II} = H\sqrt{\frac{1}{4}\alpha^2(1 + \eta^2 - 2\eta\cos\varphi) + \nu^2}$ and

$$\bar{d}_{PII} = \frac{\alpha^3}{8\pi}\int_0^{2\pi} d\varphi \int_0^1 d\eta \frac{\eta(1 - \eta\cos\varphi)z_0}{\left\{\frac{1}{4}\alpha^2(1 + \eta^2 - 2\eta\cos\varphi) + \nu^2\right\}^{3/2}}. \tag{2.39}$$

Averaging over all source points on the cylinder wall is done just as before in Eq. (2.34), thus the average distance is

$$\bar{d}_{I\to II} = \frac{\alpha^2 D}{8\pi}\int_0^{2\pi} d\varphi \int_0^1 d\eta \int_0^1 d\nu \frac{\eta\nu(1-\eta\cos\varphi)}{\left\{\frac{1}{4}\alpha^2\left(1+\eta^2-2\eta\cos\varphi\right)+\nu^2\right\}^{3/2}}. \qquad (2.40)$$

Integration yields the following

$$\bar{d}_{I\to II} = \frac{2\alpha D}{3\pi} - \frac{\alpha^2 D}{4\pi}\int_0^{2\pi} d\varphi \int_0^1 d\eta \frac{\eta(1-\eta\cos\varphi)}{\sqrt{4+\alpha^2\left(1+\eta^2-2\eta\cos\varphi\right)}}. \qquad (2.41)$$

This integral will be numerically integrated.

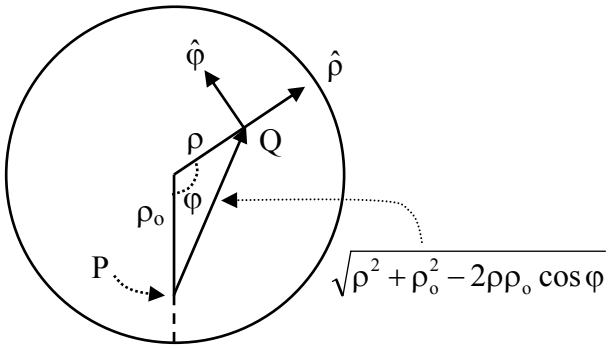

Fig. 19. Cross-sectional view of the cylindrical cavity. The source point P is on the base (z=0) at a distance of ρ_o from the axis. The end point Q is on the top (z=H) at a distance ρ from the cylinder axis.

Finally consider $\bar{d}_{II\to III}$, where the source points are located on the lower end face and the end points are located on the upper end face, see Fig. 19. The source point is $\{\rho_0,0,0\}$ and the end point is $\{\rho, \varphi, H\}$. The normals are $\hat{n}_{II} = \{0,0,-1\}$ and $\hat{n}_{III} = \{0,0,1\}$. The vector from the source point to the end point is

$\vec{r}_{III} = \{\rho - \rho_0 \cos\varphi, \rho_0 \sin\varphi, H\}$ and its magnitude is $\vec{r}_{III} = \sqrt{\rho^2 + \rho_0^2 - 2\rho\rho_0 \cos\varphi + H^2}$.

The cosine factors are

$$\frac{|\hat{n}_{II} \cdot \vec{r}_{III}|}{r_{III}} = \frac{|\hat{n}_{III} \cdot \vec{r}_{III}|}{r_{III}} = \frac{H}{\sqrt{\rho^2 + \rho_0^2 - 2\rho\rho_0 \cos\varphi + H^2}}. \tag{2.42}$$

Again we introduce normalized coordinates $\eta = \frac{\rho}{R}$ and $\mu = \frac{\rho_0}{R}$ where $0 \le \eta, \mu \le 1$, as well as $\alpha = \frac{2R}{H} = \frac{D}{H}$. Thus $r_{III} = H\sqrt{\frac{1}{4}\alpha^2\left(\eta^2 + \mu^2 - 2\eta\mu\cos\varphi\right) + 1}$ and

$$\bar{d}_{PIII} = \frac{\alpha^2 H}{4\pi}\int_0^{2\pi} d\varphi \int_0^1 d\eta \frac{\eta}{\left\{\frac{1}{4}\alpha^2\left(\eta^2 + \mu^2 - 2\eta\mu\cos\varphi\right) + 1\right\}^{3/2}}. \tag{2.43}$$

Next we must average over all source points on the base,

$$\bar{d}_{II\to III} = \frac{1}{\pi R^2}\int_0^R \bar{d}_{PIII}\, 2\pi\rho_0 d\rho_0 = 2\int_0^1 \bar{d}_{PIII}\,\mu d\mu. \tag{2.44}$$

Plugging Eq. (2.43) into Eq. (2.44) yields

$$\bar{d}_{II\to III} = \frac{\alpha^2 H}{2\pi}\int_0^{2\pi} d\varphi \int_0^1 d\eta \int_0^1 d\mu \frac{\eta\mu}{\left\{\frac{1}{4}\alpha^2\left(\eta^2 + \mu^2 - 2\eta\mu\cos\varphi\right) + 1\right\}^{3/2}}. \tag{2.45}$$

Integrating over μ yields

$$\bar{d}_{II\to III} = 2H - \frac{4H}{\pi}\int_0^{2\pi} d\varphi \int_0^1 d\eta \frac{\eta\left(4 + \alpha^2\eta^2 - \alpha^2\eta\cos\varphi\right)}{\sqrt{4 + \alpha^2\eta^2 + \alpha^2\left(1 - 2\eta\cos\varphi\right)}\left(4 + \alpha^2\eta^2\sin^2\varphi\right)}. \tag{2.46}$$

We will leave the remaining integrals to be done numerically.

For rays originating on the cylinder wall, the average Lambertian weighted travel distance to all cavity surfaces is

$$\bar{d}_W = \bar{d}_{I\to I} + \bar{d}_{I\to II} + \bar{d}_{I\to III}. \tag{2.47}$$

For rays originating on the bottom face, the average Lambertian weighted travel distance to all cavity surfaces is

$$\bar{d}_B = \bar{d}_{II\to I} + \bar{d}_{II\to III}. \tag{2.48}$$

Symmetry dictates that $\bar{d}_T = \bar{d}_B$; that is, the average Lambertian weighted travel distance from the bottom face to the top face must be equal to that from the top face to the bottom.

It is also clear that the average Lambertian weighted travel distance from the wall to either end face is equal to that from the end face to the wall when multiplied by the ratio of the end face surface area to the wall surface area; or, put more succinctly,

$$\bar{d}_{I\to II} = \frac{A_{II}}{A_I}\bar{d}_{II\to I}. \tag{2.49}$$

The cavity radiation is isotropic, therefore the probability P_W that a source point is on the wall is

$$P_W = \frac{A_I}{A_I + 2A_{II}} = \frac{2\pi RH}{2\pi RH + 2\pi R^2} = \frac{H}{H+R} = \frac{2}{\alpha+2}, \tag{2.50}$$

and the probability $P_B = P_T$ that a source point is on an end face is

$$P_B = P_T = \frac{A_{II}}{A_I + 2A_{II}} = \frac{\pi R^2}{2\pi RH + 2\pi R^2} = \frac{R}{2(H+R)} = \frac{\alpha}{2(\alpha+2)}. \tag{2.51}$$

Thus the average distance between reflections, for a cylindrical cavity with Lambertian walls, is

$$\begin{aligned}\bar{d} &= \bar{d}_W P_W + \bar{d}_B P_B + \bar{d}_T P_T \\ &= \left(\bar{d}_{I\to I} + 2\bar{d}_{I\to II}\right)\frac{2}{\alpha+2} + 2\left(\frac{A_I}{A_{II}}\bar{d}_{I\to II} + \bar{d}_{II\to III}\right)\frac{\alpha}{2(\alpha+2)}.\end{aligned} \tag{2.52}$$

Since $A_I/A_{II} = 4/\alpha$ Eq. (2.52) can be simplified to

$$\bar{d} = \frac{2}{\alpha+2}\bar{d}_{I\to I} + \frac{8}{\alpha+2}\bar{d}_{I\to II} + \frac{\alpha}{\alpha+2}\bar{d}_{II\to III}. \tag{2.53}$$

Using Eqs. (2.36), (2.41), and (2.46) with Eq. (2.53) gives

$$\begin{aligned}\bar{d} = \frac{2D}{\alpha+2} + \frac{2D}{\pi(\alpha+2)}\Bigg\{&\int_0^{2\pi}\sin^2\frac{\varphi}{2}\sqrt{1+\alpha^2\sin^2\frac{\varphi}{2}}\,d\varphi \\ &- \alpha^2\int_0^{2\pi}d\varphi\int_0^1 d\eta\,\frac{\eta(1-\eta\cos\varphi)}{\sqrt{4+\alpha^2+\alpha^2\eta^2-2\alpha^2\eta\cos\varphi}} \\ &- 2\int_0^{2\pi}d\varphi\int_0^1 d\eta\,\frac{\eta\left(4+\alpha^2\eta^2-\alpha^2\eta\cos\varphi\right)}{\sqrt{4+\alpha^2+\alpha^2\eta^2-2\alpha^2\eta\cos\varphi}\left(4+\alpha^2\eta\sin^2\varphi\right)}\Bigg\}.\end{aligned} \tag{2.54}$$

Numerically integrating the terms in the curly brackets yields zero for all $0 \le \alpha \le \infty$. Recall $\alpha = 2R/H$, thus the curly bracket term is zero for all α and the average distance between reflections in a cylindrical cavity is

$$\bar{d} = \frac{2D}{\alpha+2} = \frac{2DH}{2H+D}. \tag{2.55}$$

In the special case in which $\alpha = D/H = 1$,

$$\bar{d}_{D=H} = \frac{2}{3}D. \tag{2.56}$$

This is exactly the same as the average distance traveled between reflections in a spherical cavity, with a diameter D, inscribed within the cylinder. Note that all of the cylinder's surfaces are tangent to the sphere's surface.

4. The Average Distance Between Reflections in a Cavity of Arbitrary Shape

Consider a cavity of arbitrary shape whose volume is V and surface area is S. Let the cavity contain n photons per unit volume, distributed such that $\mathbf{L}(\mathbf{r},\Omega)$, the radiance, is a constant throughout the cavity. Consider an infinitesimal element of area dS on the wall of the cavity and the infinitesimal cylindrical volume shown in Fig. 20. The number of photons in the cylinder is $n(c\Delta t)(\mu dS)$ where $\mu = \cos\theta$. The photon propagation directions are uniformly distributed over a 4π solid angle at any point within the cavity; thus, the fraction of the photons propagating in the direction (θ, φ) in the solid angle $d\Omega = d\mu d\varphi$ is

$$P_u = \frac{1}{4\pi} d\mu d\varphi . \tag{2.57}$$

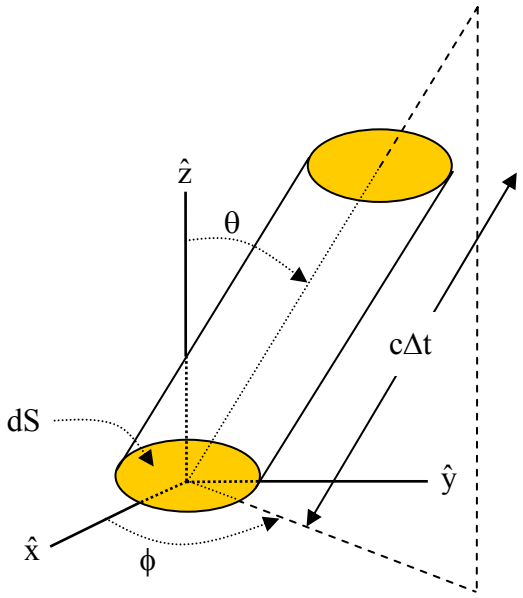

Fig. 20. Geometry for the photon flux incident on the wall of a cavity.

Therefore, in a uniform distribution, the number of photons in the cylinder in Fig. 20 that travel in the direction (θ, φ) in an infinitesimal solid angle dμdφ is

$$dN_u = n(c\Delta t)(\mu dS)\left(\frac{1}{4\pi}d\mu d\varphi\right) = \left(\frac{nc}{4\pi}\right)(\mu d\mu d\varphi)dSdt\,. \tag{2.58}$$

Since there is no photon-photon scattering within the volume, these photons must be supplied by reflection from the surface.

Consider the photons reflected from the surface. The total number of photons in the cavity is nV and these photons will, on average, be incident on the wall in a time $\bar{d}/c$, where $\bar{d}$ is the average distance between collisions with the cavity wall. Therefore, the total number of photons incident on the wall per unit time per unit area is

$$\frac{nV}{\left(\bar{d}/c\right)S} = \frac{ncV}{\bar{d}S}\,. \tag{2.59}$$

Let us assume the surface is Lambertian, that is constant $\mathbf{L}(\mathbf{r}, \boldsymbol{\Omega})$. Thus the probability that photons will be reflected from the surface at an angle θ to the normal is proportional to μ and is independent of the angle of incidence. The probability that photons will be reflected at angles θ, φ into an infinitesimal solid angle $d\Omega = d\mu d\varphi$ is then

$$P_r = \frac{1}{\pi}\mu d\mu d\varphi, \tag{2.60}$$

where the factor $1/\pi$ provides normalization. Photons reflected at angles θ, φ into the infinitesimal solid angle $d\mu d\varphi$ from the element of the cavity surface area dS in time dt are contained in the cylinder shown in Fig. 20. From Eqs. (2.59) and (2.60), the number of these photons is

$$dN_r = \left(\frac{ncV}{\bar{d}S}\right)\left(\frac{1}{\pi}\mu d\mu d\varphi\right)dSdt = \left(\frac{ncV}{\pi\bar{d}S}\right)(\mu d\mu d\varphi)dSdt\,. \tag{2.61}$$

Maintaining constant radiance requires $dN_u = dN_r$. Clearly, it is possible to satisfy this condition because the θ, φ dependences in dN_u and dN_r are identical in Eqs. (2.58) and (2.61), and we find

$$\bar{d} = 4\frac{V}{S}\,. \tag{2.62}$$

This is a completely general result for $\bar{d}$ independent of cavity shape and depending only on the volume to surface ratio and the condition that the field in the cavity be maintained as homogeneous and isotropic. This result has also been obtained from neutron transport theory.[19] We point out that Hobbs and McCormick[20] also recognized the correlation between the result from neutron diffusion and the average path length in an integrating cavity. The assumption of a Lambertian surface provided the μ factor

needed in Eq. (2.61) for the comparison with Eq. (2.58); however, Eq. (2.58) can be satisfied by other types of surfaces. A specular reflector will maintain an isotropic radiance distribution but will not convert an anisotropic radiance distribution into an isotropic one, whereas a Lambertian surface will asymptotically convert an anisotropic distribution into an isotropic distribution.

5. The General Result for a Cavity Formed by Planes Tangent to an Inscribed Sphere

Consider an arbitrary cavity shape for which each flat face is tangent to a single inscribed sphere of diameter D, radius R (a curved surface is considered to be an infinite number of flat surfaces). It will be shown that for such a cavity $\bar{d} = 2D/3$; this is identical to $\bar{d}$ for the inscribed sphere.

The cavity has volume V and surface area S. Suppose the areas of the flat faces (each face has 3 or more sides) for this cavity are denoted by S_i. Consider lines drawn from the center of the inscribed sphere to each vertex in the cavity wall. If there are M flat faces, these lines define M pyramidal shaped objects whose bases have area S_i, and whose volumes are V_i, where

$$\sum_{i=1}^{M} V_i = V, \qquad \text{and} \qquad \sum_{i=1}^{M} S_i = S. \tag{2.63}$$

Each of these pyramidal objects has a height equal to the inscribed sphere's radius R, which is perpendicular to the face at the tangent point. At a distance r from the apex of

one of these pyramidal objects, the cross-section parallel to the base has dimensions directly proportional to r; hence the area $s_i(r)$ of such a cross-section is proportional to r^2. The boundary condition at r=R is $s_i(R) = S_i$, hence

$$s_i(r) = S_i \frac{r^2}{R^2}. \tag{2.64}$$

The volume of these pyramidal objects is then

$$V_i = \int_0^R s_i(r)dr = S_i \frac{D}{6}. \tag{2.65}$$

Summing over all M objects that make up the cavity and using Eqs. (2.63) yields

$$\frac{V}{S} = \frac{D}{6}, \tag{2.66}$$

which is identical to V/S for the inscribed sphere. This is a general result for any object all of whose faces are tangent to a single inscribed sphere. The result for $\bar{d}$ in such a cavity then follows from Eq. (2.62),

$$\bar{d} = \frac{2}{3}D. \tag{2.67}$$

Eq. (2.62) is completely general. Consider a cylinder of arbitrary height H and diameter D; the volume to surface area ratio is

$$\left(\frac{V}{S}\right)_{cyl} = \frac{1}{2}\left(\frac{DH}{2H + D}\right). \tag{2.68}$$

Eq. (2.62) then yields

$$\bar{d} = 4\left(\frac{V}{S}\right)_{cyl} = \frac{2DH}{2H + D}, \tag{2.69}$$

which is identical to the brute force derivation resulting in Eq. (2.55). It is interesting to note that if H»D, then $\bar{d} \approx D$. Compare this result to a torus. The volume to surface ratio of a torus is $\left(V/S\right)_{torus} = D/4$, where D is the diameter of the ring cross-section. It is completely independent of the radius used to generate the torus. Using Eq. (2.62), we find that $\bar{d} = D$, which is exactly the same as a long cylinder. This should not be too surprising. In the case of the cylinder, the longer it gets the less the end caps affect the dynamics of the cavity. The torus, when cut open, can be viewed as a cylinder with the boundary condition that the radiance out one end is retro-reflected back into the cavity. That is, it behaves as if it were cut open and then stretched into a long cylinder while maintaining its cross-sectional diameter.

To sum things up we see that, provided the reflectivity of an integrating cavity is near unity, the simple models for the cavity decay constant agree well with the Monte Carlo simulations. As the reflectivity decreases the agreement decreases as well. It should be noted that if a sphere of diameter D can be inscribed inside an integrating cavity so that it is tangent at one point to every flat surface then the average distance traveled between reflections $\bar{d}$ in the cavity is 2D/3. Finally, for any cavity with a Lambertian surface and a reflectivity near unity, $\bar{d}$ will equal 4V/S, independent of the cavity's shape. If a nonhomogeneous field is injected into a cavity (which is incapable of converting the field into a homogeneous and isotropic field due to either the reflector's characteristics or the level of absorption in the sample) then $\bar{d} \neq 4V/S$. One would hardly think this obvious statement warrants any attention; however, a quick

overview of some of the commercial instruments in the marketplace reveals the necessity of such a statement. Thus the experimentalist should always be aware of the impact upon the dynamics of the integrating cavity due to the following: the given reflectivity, the absorption of the sample, and the manner in which the field is injected into the cavity.

CHAPTER III

INTEGRATING CAVITIES II,
A HIGHLY EFFICIENT LAMBERTIAN REFLECTOR

One of the key ingredients to the success of any integrating cavity device is the quality of the diffuse reflector. It is this diffuse reflectivity which allows one to integrate signals over all angles. Spectralon ®, by Labsphere*, is the world leader in diffuse reflectivity. Spectralon is composed of polytetrafluoroethylene PTFE, a powder which has been pressed into machinable blocks. Spectralon has an effective spectral range of 250 nm to 2500 nm.[21] Although Spectralon is an outstanding diffuse reflector it has a couple of issues which cause concern. If exposed to ultraviolet light it can undergo photolytic degradation[22,23] and its performance will diminish over time. Spectralon has a reflectivity of 99.0-99.2% across the visible spectrum, while in the ultraviolet range it decreases to 95.0% at 250 nm and then drops rapidly.[21] At 500 nm the optical path length in a 5 cm integrating sphere, made from Spectralon, is 3.69 m. If one were able to increase the reflectivity from 99.1% to 99.9% or 99.99% the path length would increase to 33 m and 333 m respectively. The 10 to 100 fold increase in the optical path length would greatly enhance the sensitivity of the integrating cavity. This raises the question, can we make a better diffuse reflector, one that works farther into the ultraviolet and with a higher reflectivity?

---

*Spectralon ® is produced by Labsphere, Inc., North Sutton, NH.

1. A Simple Model of a Retro-Reflector

We present a simple model to facilitate our understanding of a high efficiency diffuse reflector. Consider a beam of light at normal incidence to 1, 2, 3 or N sheets of glass. Let η be the reflectivity of a surface behind the last plate of glass and let ρ be the reflectivity at each glass-air interface. Let i_n be the intensity of the light in the successive locations, and traveling in the directions shown in Fig. 21. The intensity of light leaving upward from the n^{th} plate is i_{4n}, the intensity of light incident from above on the n^{th} plate is i_{4n+1}, the intensity of light going upward within the n^{th} plate is i_{4n-2}, etc. Let us assume the glass plates have no absorption. In the case of 1 layer of glass, see Fig. 22, we can solve for the total reflection with the following equations:

$$i_1 = i_0\rho + i_3(1-\rho) \tag{3.1}$$

$$i_2 = i_3\rho + i_0(1-\rho) \tag{3.2}$$

$$i_3 = i_2\rho + i_5(1-\rho) \tag{3.3}$$

$$i_4 = i_5\rho + i_2(1-\rho) \tag{3.4}$$

$$i_5 = i_4\eta\,. \tag{3.5}$$

These simultaneous equations can be solved for the total reflected light $R = i_1/i_0$,

$$R = \frac{\eta + 2\rho - 3\eta\rho}{1+\rho-2\eta\rho}\,. \tag{3.6}$$

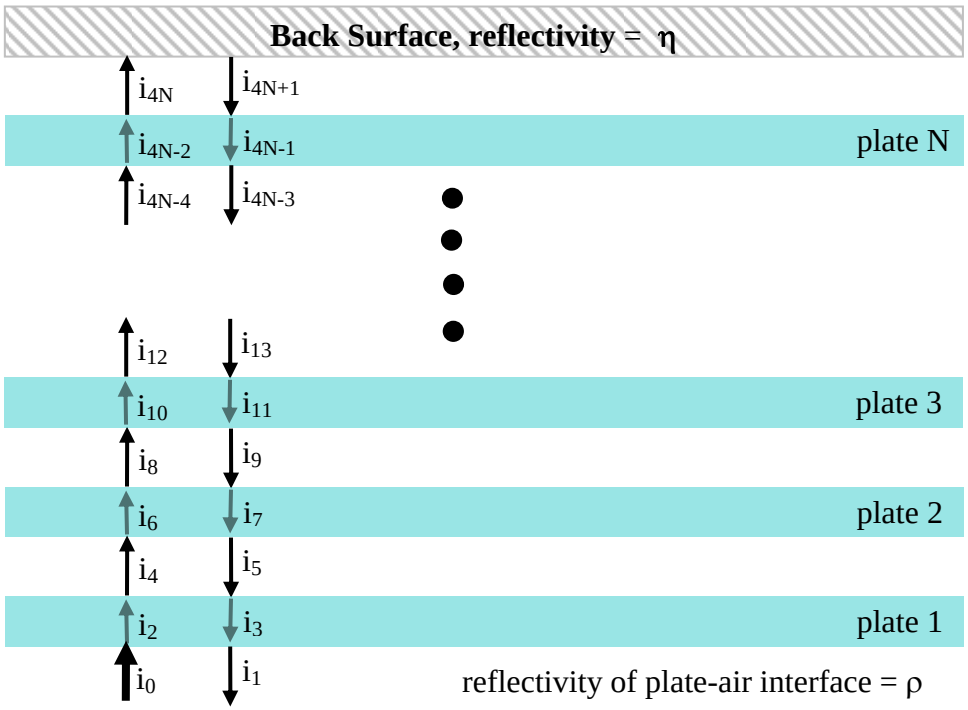

Fig. 21. Geometry for calculating the reflectivity of N plates.

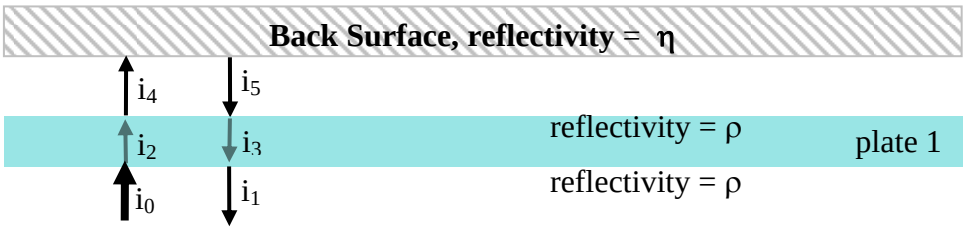

Figure 22. Geometry for calculating the reflectivity of 1 plate.

To solve the case of 2 layers of glass Eqs. (3.1) - (3.4) remain the same, Eq. (3.5) is replaced with Eq. (3.7) and Eqs. (3.8) - (3.11) are added to the list:

$$i_5 = i_4\rho + i_7(1-\rho) \tag{3.7}$$

$$i_6 = i_7\rho + i_4(1-\rho) \tag{3.8}$$

$$i_7 = i_6\rho + i_9(1-\rho) \tag{3.9}$$

$$i_8 = i_9\rho + i_6(1-\rho) \tag{3.10}$$

$$i_9 = i_8\eta\,. \tag{3.11}$$

Solving for the total reflected light we find

$$R = \frac{\eta + 4\rho - 5\eta\rho}{1 + 3\rho - 4\eta\rho}. \tag{3.12}$$

Continuing in this vein yields the following solutions:

1 layer of glass $$R = \frac{\eta + 2\rho - 3\eta\rho}{1 + \rho - 2\eta\rho} \tag{3.13}$$

2 layers of glass $$R = \frac{\eta + 4\rho - 5\eta\rho}{1 + 3\rho - 4\eta\rho} \tag{3.14}$$

3 layers of glass $$R = \frac{\eta + 6\rho - 7\eta\rho}{1 + 5\rho - 6\eta\rho} \tag{3.15}$$

4 layers of glass $$R = \frac{\eta + 8\rho - 9\eta\rho}{1 + 7\rho - 8\eta\rho} \tag{3.16}$$

N layers of glass $$R = \frac{\eta + 2N\rho - (2N+1)\eta\rho}{1 + (2N-1)\rho - 2N\eta\rho}. \tag{3.17}$$

Let us consider some test cases. If N = 0 the reflectivity goes to η. If $\rho = 0$, the reflectivity goes to η. If ρ or $\eta = 1$ the reflectivity goes to 1. All these results are as expected. In Fig. 23, the reflectivity is plotted for $\rho = 0.04$ (the typical reflectivity at a glass-air interface) and for $\eta = 0$, 0.04, 0.1, 0.2, 0.4, 0.8 and 0.9. Notice that as N grows large, η plays little role in the overall value of the reflectivity. In Fig. 24, the reflectivity

is plotted for $\eta = 0$ and for $\rho = 0.04, 0.1, 0.2, 0.4, 0.8$ and 0.9. Once again the overall value of the reflectivity depends little on ρ as N grows. In the limit of large N the reflectivity approaches unity even if ρ is small and η is 0. Consider $\rho = 0.04$ (the typical reflectivity for a quartz-air interface); a reflectivity of 0.999 is achieved with N just under 12,000, see Fig 25. Of course 12,000 layers of quartz glass plates are not practical, but the equivalent of twelve thousand layers could easily be achieved with micron sized quartz powder. Although a powder is not a retro-reflector as is a glass plate, the correspondence to multiple scatterings (reflections) provides a baseline to the concept.

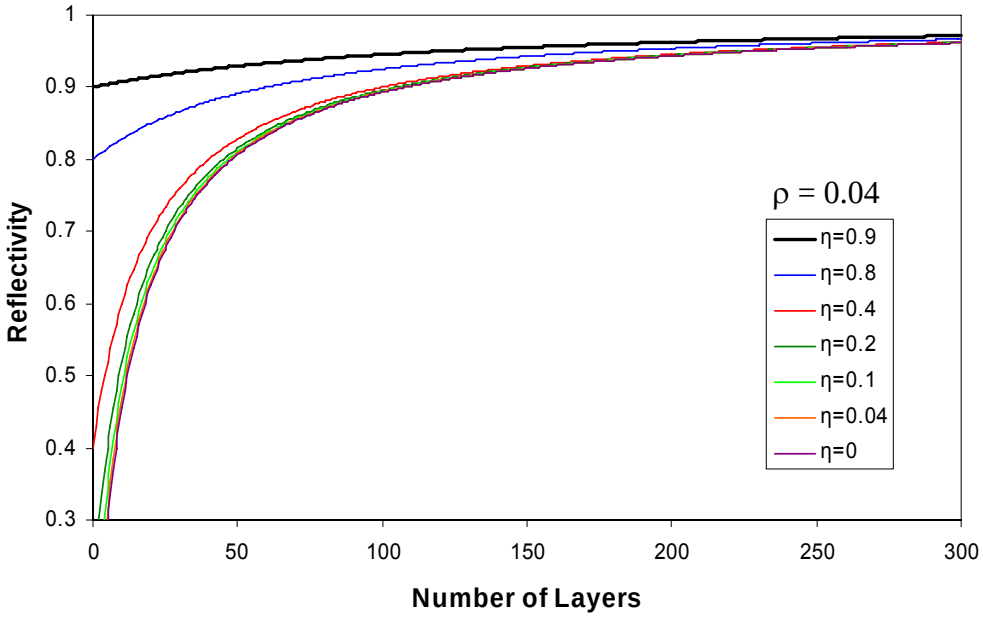

Fig. 23. Reflectivity vs. layers of glass as a function of η, with $\rho = 0.04$.

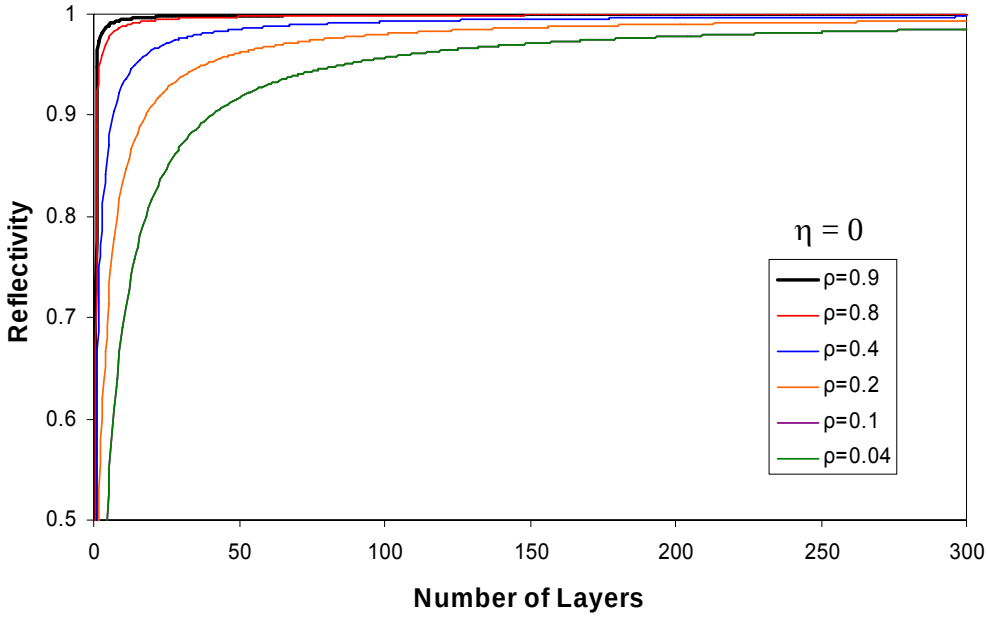

Fig. 24. Reflectivity vs. layers of glass as a function of ρ, with η = 0.0.

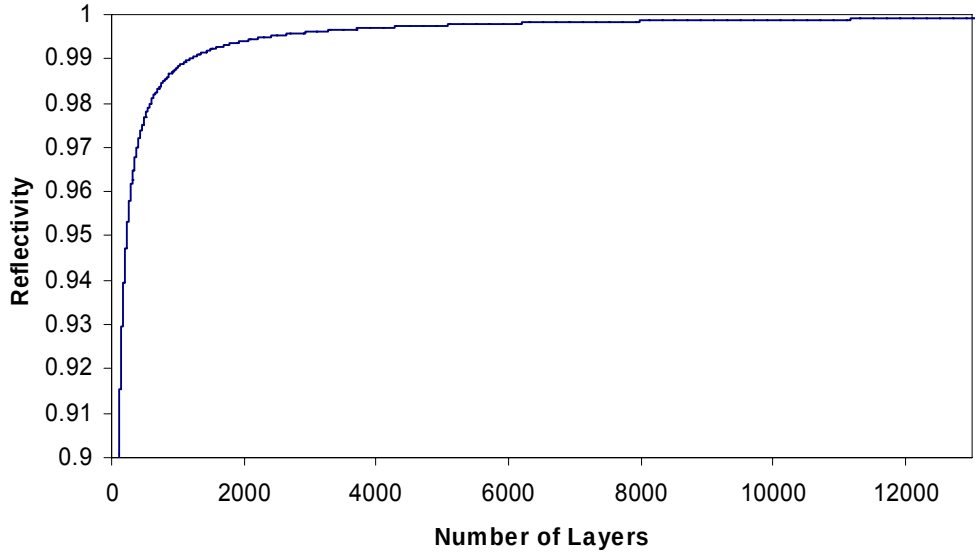

Fig. 25. Reflectivity of a stack of glass plates vs. the number of layers, with ρ = 0.04.

If one is to have a mirror of a reasonable thickness, say 2.54 cm, how thin must each glass layer be to have a reflectivity of 0.999 or 0.9999? Dividing the mirror thickness by the number of layers needed to achieve the given reflectivity yields a thickness of order 1 μm to 0.1 μm, respectively. Thus fine quartz powder should work well. The fact that powders or small droplets can provide a Lambertian surface has been known for a long time. Why then is this considered new? We hinted at it earlier with the comment about absorption. The diffuse reflector works via the index of refraction mismatch between the powder and the background medium, with the caveat that absorption be negligible. With thousands of reflections occurring in the powder layers, any absorption at all will quickly diminish the intensity of the light. Thus, the real search is for ultra pure powder with a high transmission in the wavelength of concern, i.e. fumed silica, magnesium fluoride, lithium fluoride, etc.

2. Reflectivity Tests of Fumed Silica

To begin our search we made our own fumed silica and qualitatively observed the high reflectivity and the diffuse nature of the powder. It became quickly obvious that it would have taken a monumental effort for us to produce the volume of fumed silica we desired. Fortunately we found two sources of ultra pure silica. The first was a special production run by Pegasus Glassworks Incorporated from Sturbridge, MA. They used a sol-gel process to produce the silica. The second source was the Degussa Corporation from Parsippany, NJ. Degussa mass produces a line of fumed silica products called

Aerosil. We tested three of their product lines, Aerosil 380, Aerosil 90, and Aerosil EG50. The numbers refer to the surface area per mass (m^2/g) of that grade. Fig. 26 and 27. show SEM images of fumed silica aggregates and agglomerates.[24] The base particles are approximately 40 nm and are not found alone. The base particles form aggregates and which then form agglomerates.

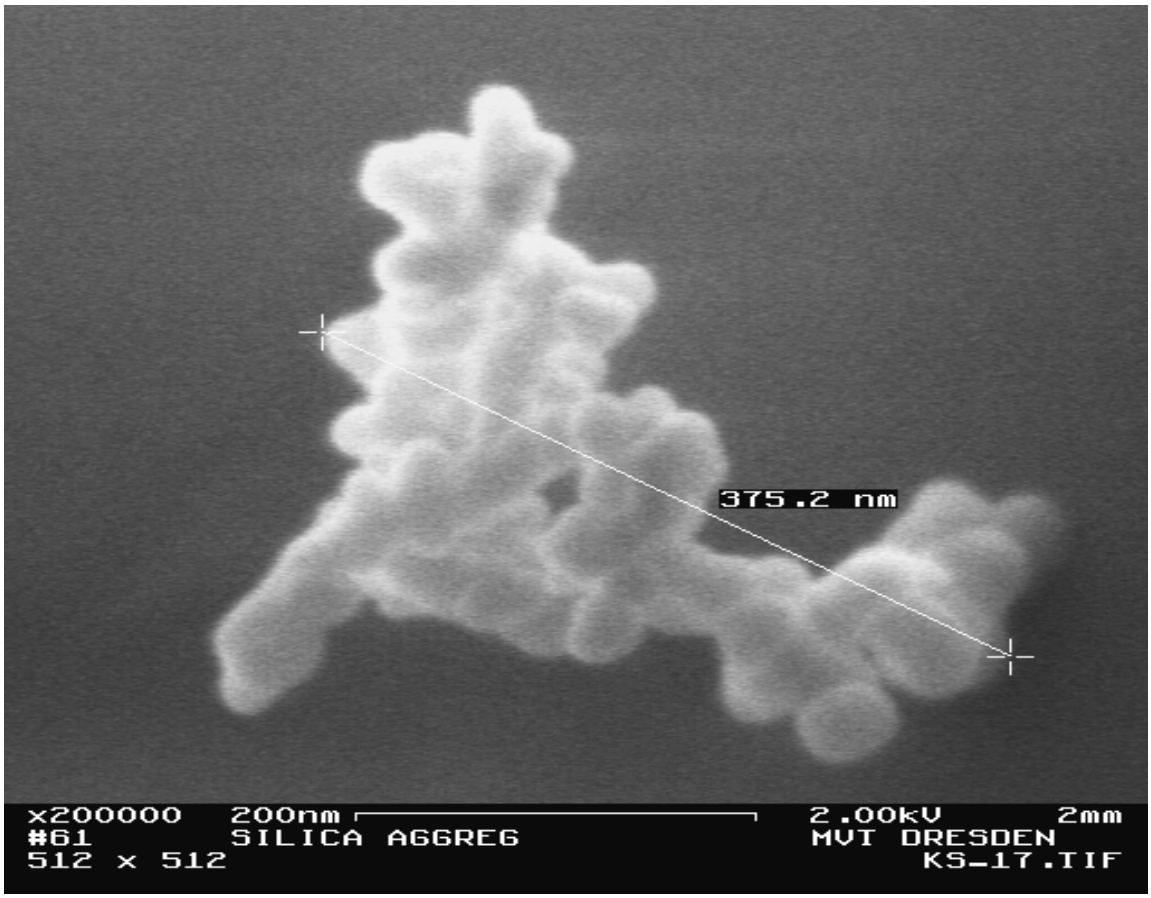

Fig. 26. Fumed silica aggregate ~ 1/3 μm.

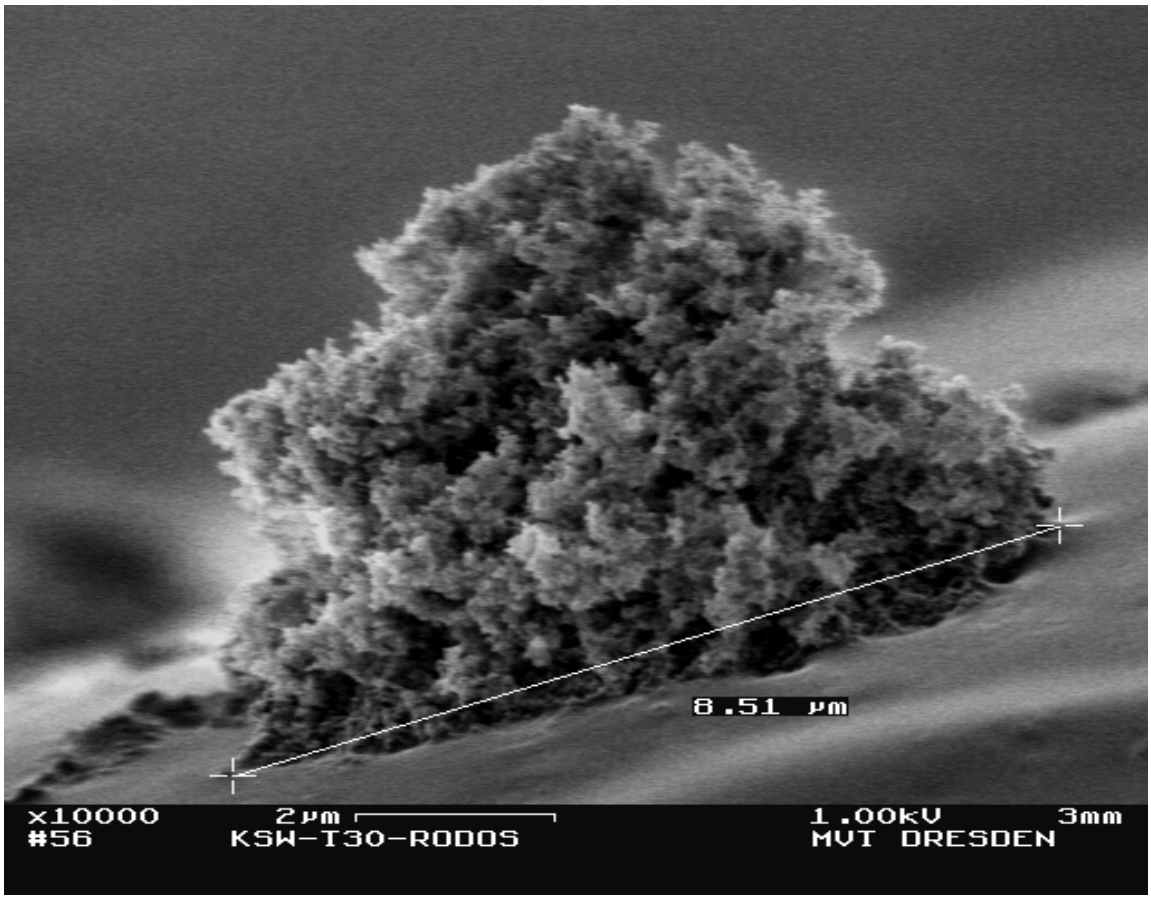

Fig. 27. Fumed silica agglomerate ~ 8.5 μm.

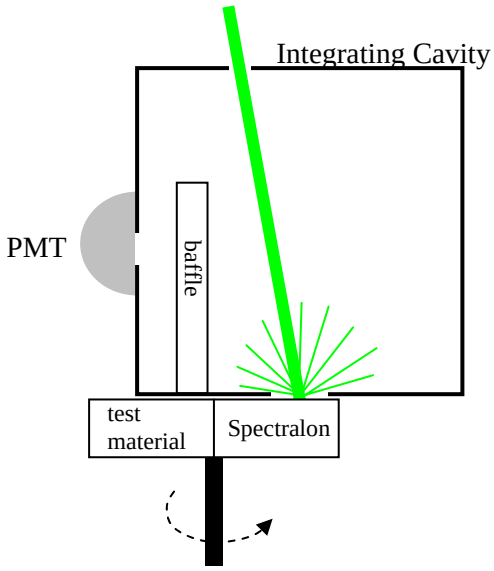

Fig. 28. Experimental setup for measuring the relative reflectivities of our samples.

The first test was a comparison of the reflectivity of the different powders as compared to Spectralon. This test was conducted by rotating the samples underneath a small port of an integrating cavity. A laser beam was incident on the sample at an angle of 8° from normal. On the side of the integrating cavity and shielded from any direct reflections was a Hamamatsu 1P21 photomultiplier tube, see Fig. 28. Fig. 29 shows the data for Spectralon vs. Aerosil 380, Aerosil 90, and Aerosil EG50. The “dog ears” in the data are due to specular reflections from a metal ring which is supporting the quartz powder. Both Aerosil 90 and EG50 outperformed Spectralon. In Fig. 30 one can see that the Pegasus quartz power also outperformed Spectralon.

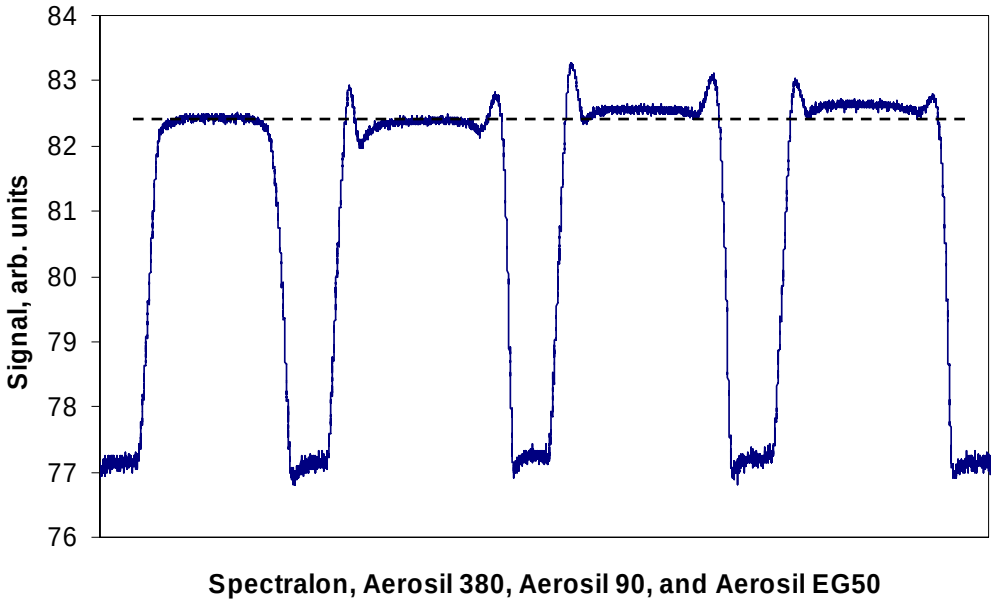

Fig.29. Relative reflectivity measurement for Spectralon vs. the Aerosil products.

The powders have a large surface area per unit mass and readily absorb moisture and other volatile materials. Thus, it became necessary to bake the powders and protect them from contamination. Fig. 31 compares the performance of each powder, which is normalized to Spectralon's reflectivity. The baked Aerosil EG 50 outperformed all other samples. The baked Aerosil 90 and baked Pegasus also performed well and are suitable for a variety of applications.

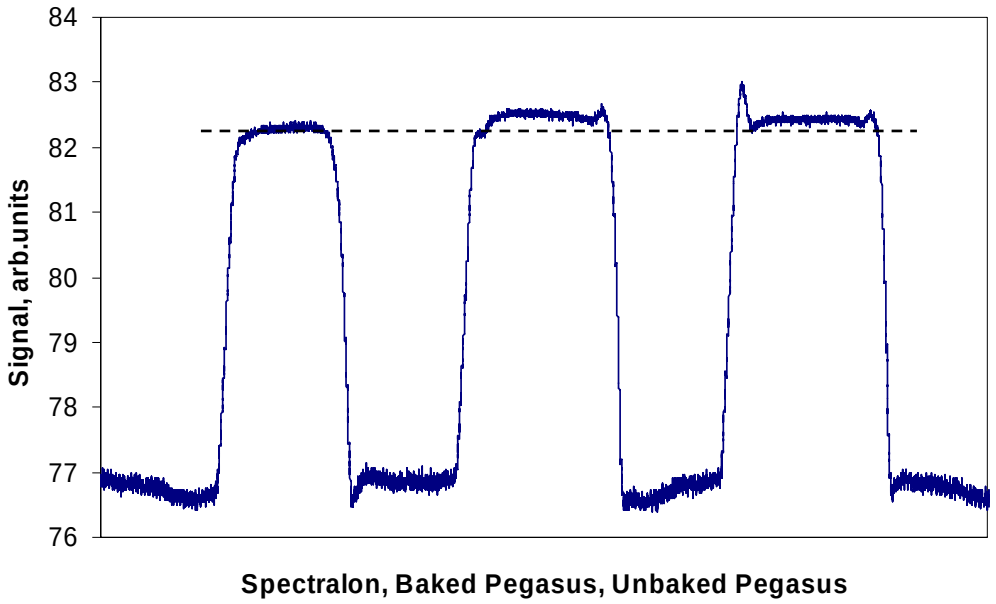

Fig. 30. Relative reflectivity measurements for Spectralon vs. the Pegasus product.

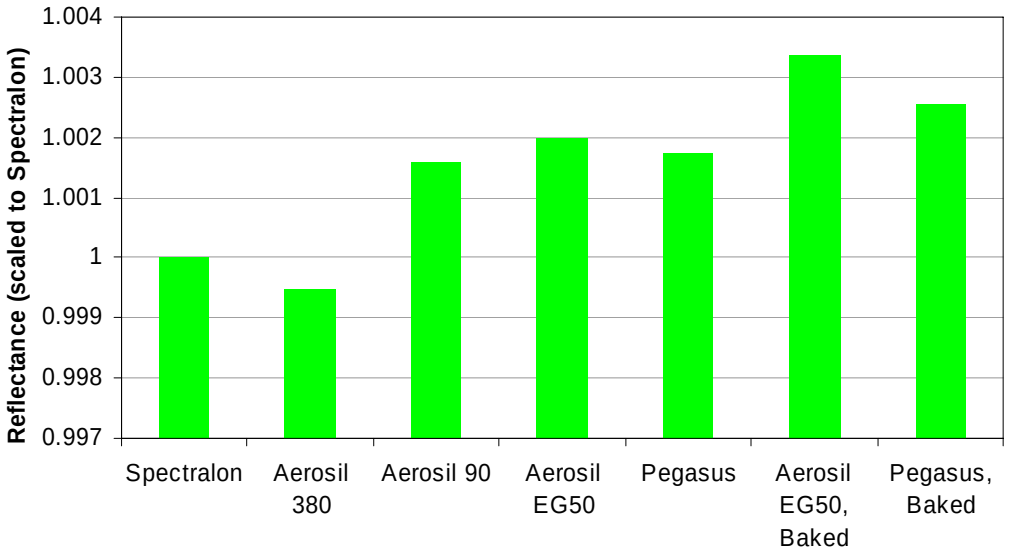

Fig. 31. Relative reflectivity comparison of all products at 532 nm.

3. Transmission vs. Pressure Test

Transmission measurements were made to determine the optimal pressure with which to press the powder. The Aerosil 90 and Aerosil EG50 were pressed into metal rings 1 cm tall and 2.54 cm inner diameter. The rings were illuminated from above with a 532 nm laser. The transmission through the sample was measured directly beneath the ring. As can be seen in Fig. 32, there is a wide range in which the reflectivity is fairly constant for the Aerosil 90 sample. Fig. 33 shows the low pressure range of Fig. 32.

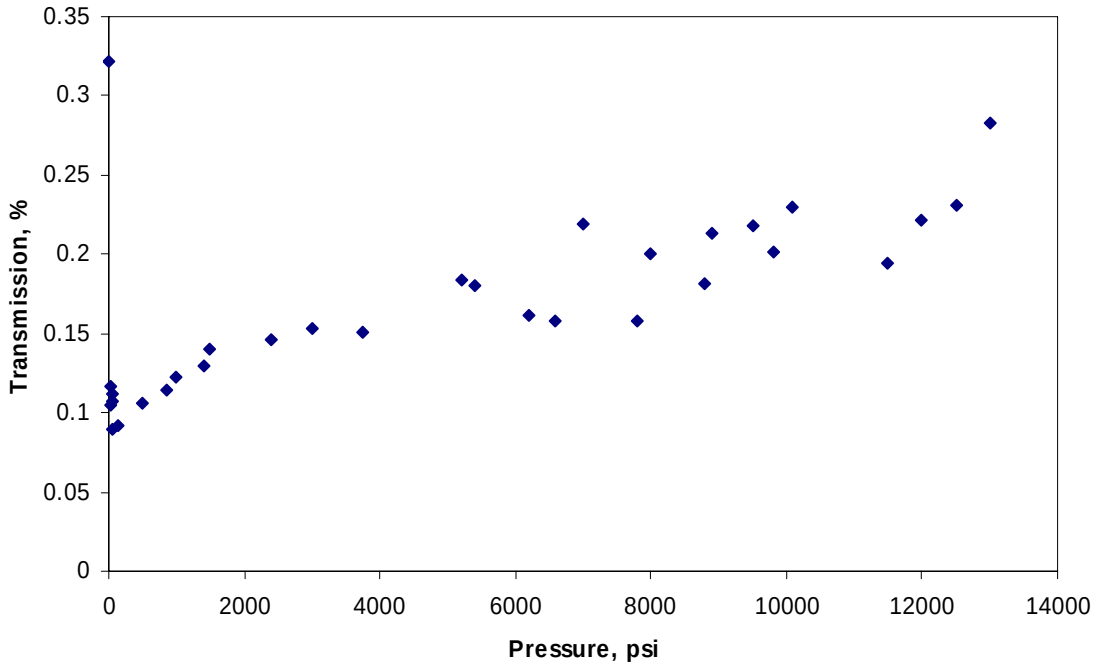

Fig. 32. Transmission vs. pressure for Aerosil 90.

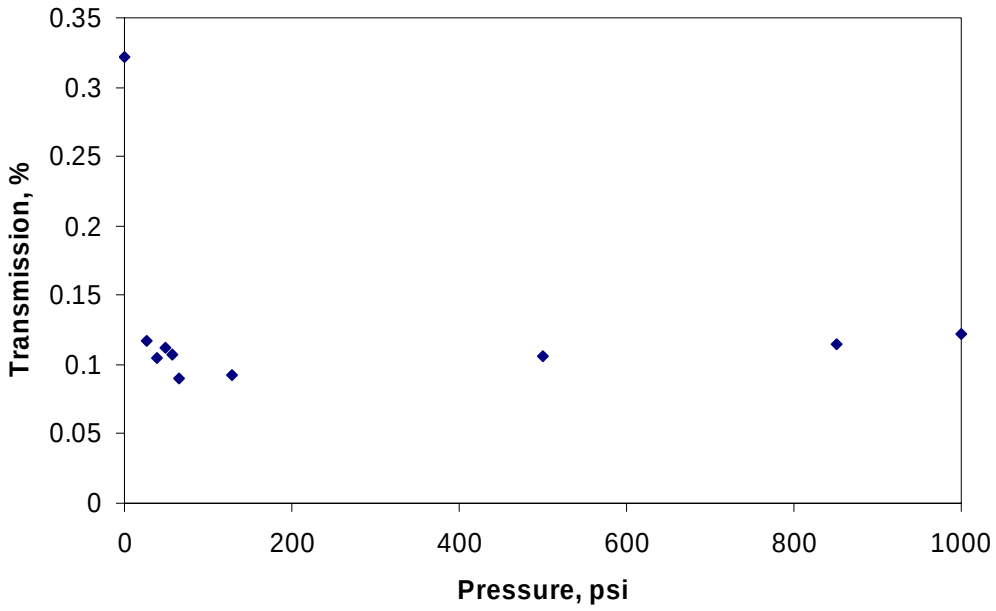

Fig. 33. Expanded low pressure range of Fig. 32.

Fig. 34 shows the transmission vs. pressure for Aerosil EG50. It should be noted the powder does have a tendency to relax and expand after being pressed. Although quartz is quite hard (H=7 on the Mohs scale), it did behave at the macroscopic level as though it were somewhat elastic. Like a rubber block it would partially expand back as pressure was removed from the powder. The powder can be machined after it has been pressed; however, it is a delicate process, similar to carving a bar of soap.

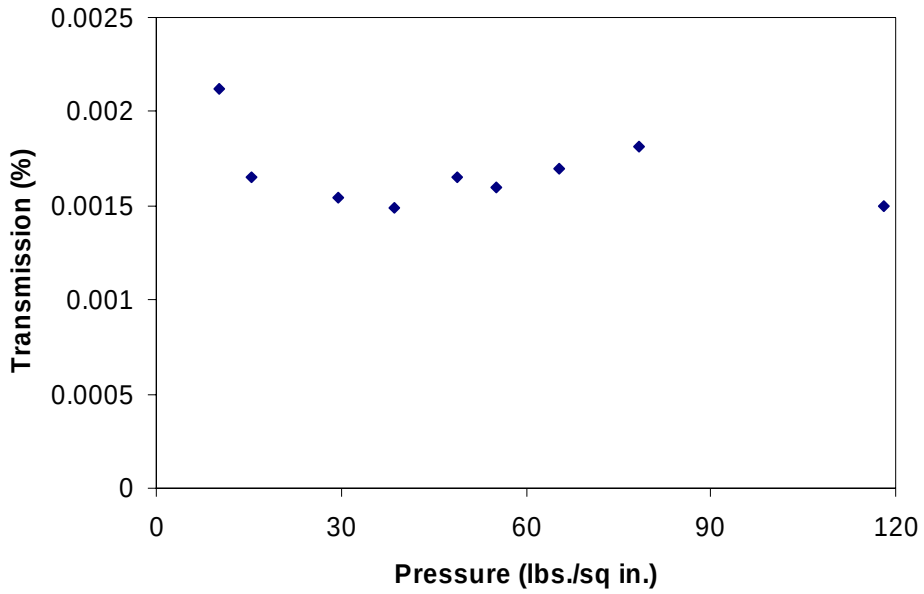

Fig. 34. Transmission vs. pressure for Aerosil EG50.

4. BRDF Measurements

The character of a diffuse scatterer can be quantified with the bi-directional reflectance distribution function, BRDF, as proposed by Nicodemus in 1977 and now widely used as an industry standard for describing diffusely reflective material.[21,25,26]

$$\mathrm{BRDF}(\theta_s,\phi_s) \equiv \frac{\mathrm{radiance}(\theta_s,\phi_s)}{\mathrm{irradiance}} = \frac{\left(P_s \big/ A\cos(\theta_s)d\Omega\right)}{P_i A} = \frac{P_s}{P_i d\Omega \cos(\theta_s)}. \quad (3.18)$$

In general the BRDF can be a function of both θ and ϕ, but usually the ϕ dependence is neglected, see Fig. 35.

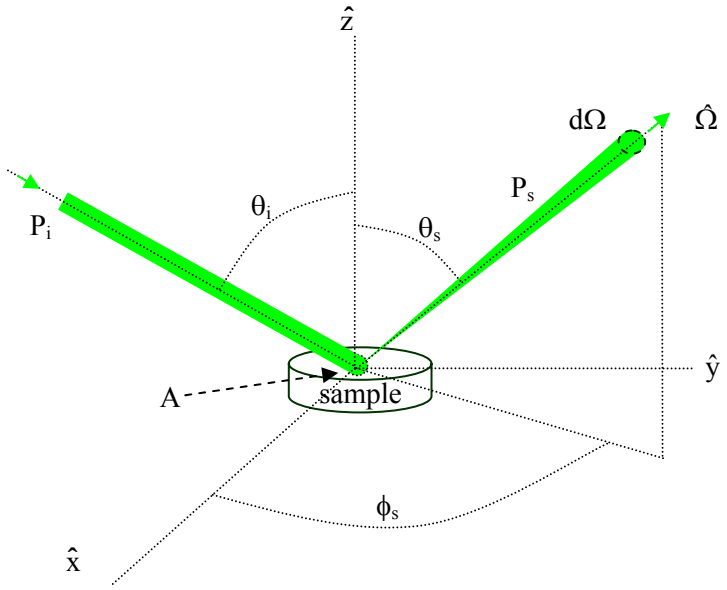

Fig. 35. Geometry for BRDF.

P_s is the power scattered into the solid angle $d\Omega$. A is the area of the sample illuminated. θ_s is the angle formed by the z axis and the unit vector $\hat{\Omega}$, along the scattering direction. ϕ_s is the azimuthal angle. Unless stated otherwise, we will only concern ourselves with the in plane BRDF; that is, when θ_i and θ_s lie in the same plane.

Recall that a Lambertian reflector is a reflector in which the number of photons scattered, at an angle θ_s, is proportional to the cosine of the scattering angle θ_s. Consider a surface which is uniformly illuminated. If one views a small circle from directly above it, one will see a circle; however, as one views this circle from some other angle one sees a smaller area, an ellipse. This is the projection of the circle along a vector directed toward the viewer. The area decreases as the $\cos(\theta)$, where θ is the viewing angle. Since both the number of photons scattered and the area decrease as $\cos(\theta)$ the apparent

brightness, that is the radiance, remains the same regardless of the viewing angle. This is evidenced in the BRDF as a constant value, $BRDF_{Lambertian}=\rho/d\Omega$, where ρ is the reflectivity of the Lambertian surface. A specular reflection, on the other hand, is represented in the BRDF as a delta function.

There are several issues which cause an experimental measurement of the BRDF to deviate from these expected results. Nicodemus points out that some of the assumptions he made are not truly valid. His derivation assumes a uniform beam illuminates the surface; this is not generally the case, usually one has a Gaussian beam. He also points out that scattering is not limited to the surface of the material, but also involves bulk scattering in which case both the area being illuminated and the area scattering light are poorly defined. The assumption that the surface is uniform is not true. Even with these concerns the BRDF is still a useful and standard tool to quantify reflecting surfaces. Stover fully discusses the following additional sources of error: finite detector aperture, scatter created from the apparatus, calibration inaccuracies, noise detection nonlinearities and mechanical errors[26].

We will concern ourselves with one of the errors, that introduced by the finite size of the detector. For a true Lambertian material the scattered light goes to zero as θ goes to $\pm$ 90°, ($\cos(\pm 90°) = 0$). Thus the $BRDF_{Lambertian}$ goes to $P_s/P_i d\Omega\cos(\theta_s) = \rho P_i\cos(\theta_s)/P_i d\Omega\cos(\theta_s)=\rho/d\Omega$. When measuring the BRDF, $P_s(\theta)$ is the measured quantity. The problem is that a finite sized detector never sees P_s go to zero. At $\theta = \pm 90°$ one half of the detector is still visible to the sample, see Fig. 36.

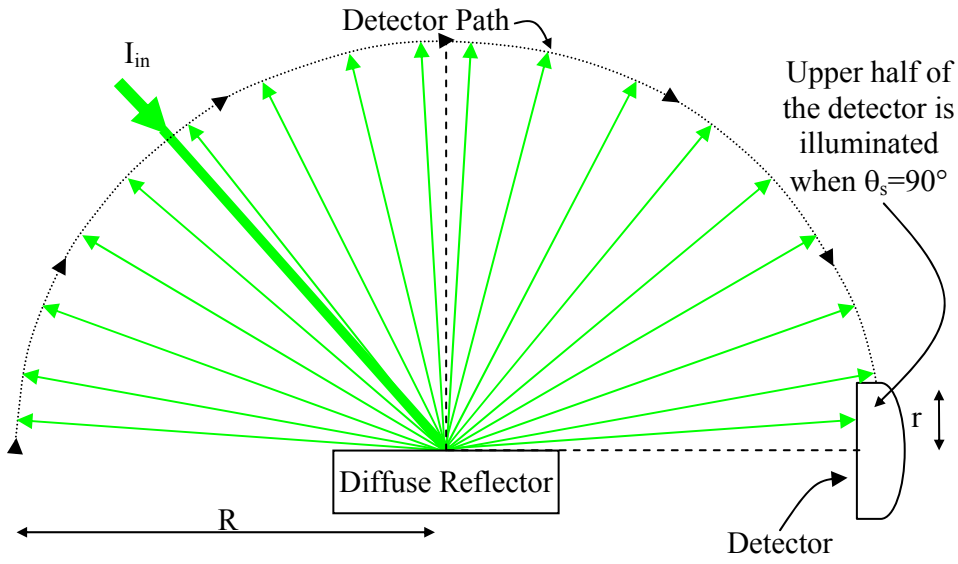

Fig. 36. Detector still "sees" light at 90°.

By dividing the small but finite value of P_s by cos(± 90°) the BRDF(±90°) grows to infinity. This problem can be easily solved by replacing cos(θ) in the BRDF with a weighted cosine function, $\cos_w(\theta)$. The $\cos_w(\theta)$ function accounts for the varying detector area visible as a function of θ. Since $\cos_w(\theta)$ is an even function we only need to define $\cos_w(\theta)$ for $0° \le \theta \le 90°$. Thus,

$$\cos_w(\theta) \equiv \frac{\int_{\text{area visible}} \cos[\theta(y)] 2\sqrt{r^2 - y^2}\, dy}{\int_{\text{area visible}} 2\sqrt{r^2 - y^2}\, dy}, \tag{3.19}$$

where the numerator is the integral of the cosine of the scattering angle, which is illuminating a horizontal section of the detector, weighted by that same detector area, $2x\,dy = 2\sqrt{r^2 - y^2}\,dy$, see Fig. 37. The denominator is the integral over the visible

region of the detector and normalizes the weighted cosine function. The limits of the integral are defined by the area of the detector that is visible. For $0 \leq \theta \leq 90\text{-}\alpha$ the limits run from y = -r to r, where $\alpha = \arctan(r/R)$. For $\theta \geq 90\text{-}\alpha$ the limits run from y_1 to r where $y_1 = -R \tan(90\text{-}\theta)$. By plotting $1/\cos(\theta)$ vs. $1/\cos_w(\theta)$ one can see that the singularity at $\theta = \pm 90°$ is avoided. This problem can also be minimized by the proper choices for the detector radius r and the detector distance R in the experimental setup.

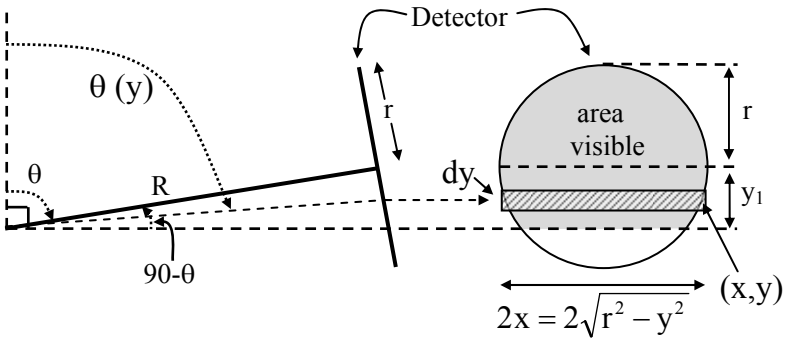

Fig. 37. Geometry for the limits defining the area visible on the detector.

There are very small errors introduced throughout the BRDF by approximating the correct $\cos_w(\theta)$ as $\cos(\theta)$. This is because the cosine function is not symmetric about an arbitrary value θ. In our experimental setup this makes a difference of about 1 part in 10,000 for all but θ near ±90°. The only error the calculation does not take into account regarding the finite-sized detector is the approximation that the surface of integration is normal to the outgoing ray along θ(y). This error also exists for those using $\cos(\theta)$ as an approximation. Provided one chooses experimental parameters such that $\arctan(r/R) \ll 1$

the error is negligible. In our experimental setup the deviation from perpendicular is a maximum of 0.6°. The projection of an area, at an angle of 0.6°, is off by a factor of only 0.0001. In Fig. 38 we plot the $1/\cos(\theta)$ function vs. the $1/\cos_w(\theta)$ for a 2.54 cm diameter detector that is 30.5 cm away from the sample. Notice that the weighted cosine function allows the BRDF to remain finite, just as it physically does. In our setup the 1.3 cm detector was 56 cm from the sample.

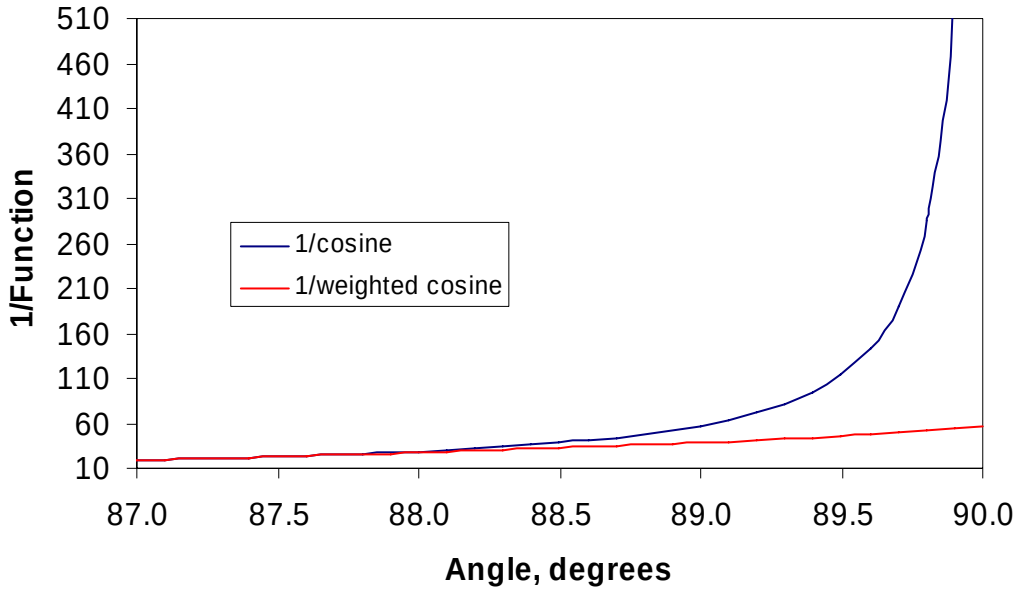

Fig. 38. Impact of 1/cosine vs. 1/ weighted cosine.

Another difficulty in measuring the BRDF is secondary scattering. A good Lambertian surface scatters a great deal of light in all directions. Therefore it is quite possible that this light will then reflect off of the rest of the instrument. Depending on the instrument's geometry this can increase the measured signal in an asymmetric

manner. Therefore it is customary to measure a traceable standard and subtract the difference between the measured standard's signal and the sample's signal. This difference signal is then added to the standard's known BRDF signal. This is not a bad method provided the sample and the standard don't differ too much in their BRDF. If the sample does differ significantly from the standard it is not true that the same amount of secondary scattering will be present at each angle. Consider a clean polished mirror as an example. Its specular reflection might not even hit the apparatus and therefore it is clear the two samples will not have the same level of error due to secondary scattering. We did not use a traceable standard with which to measure absolute values of the BRDF; thus the measurements should not be understood as absolute measurements. In our experiment, we merely wish to compare the BRDF for our diffuse quartz powder reflectors with that of Spectralon.

In Fig. 39 the BRDF of both Spectralon and Aerosil 90 are shown at 8° out of plane, 30° incidence at 404, 532 and 633 nm with perpendicular polarization. The BRDFs at each wavelength have been offset to aid the visual presentation. In-plane means that the angle of incidence and the angle of scattering lie in the same plane. Perpendicular polarization describes the situation in which the electric field vector is perpendicular to the incident plane.

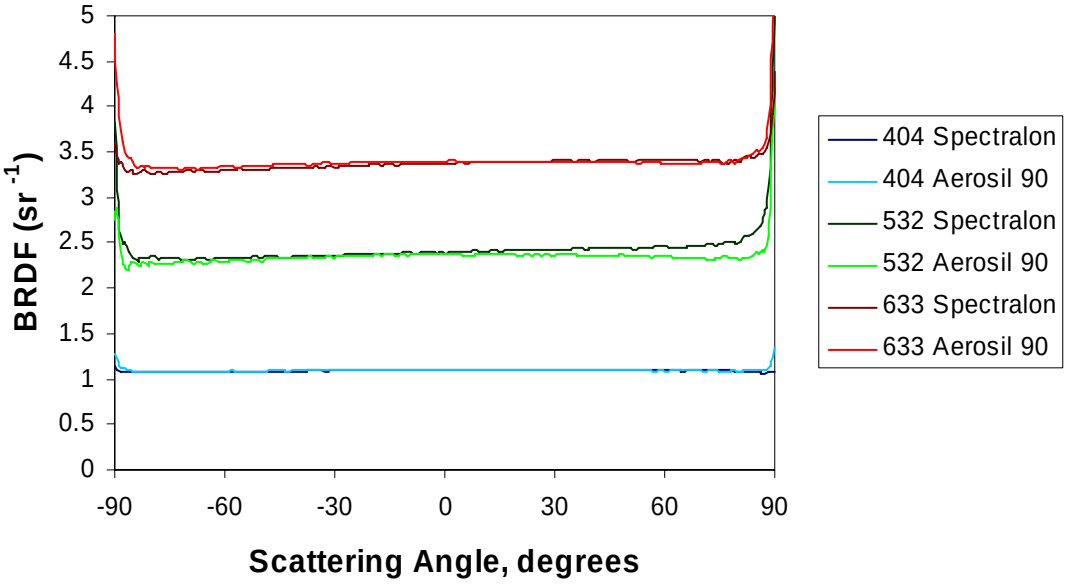

Fig. 39. BRDF, -30° incidence with parallel polarization. Data sets, for each wavelength, have been offset for the visual presentation.

Figs. 40 - 42 show the same information for 30° incidence with parallel polarization and 60° incidence with perpendicular and parallel polarization respectively. From these plots one can see that the quartz powder diffusively reflects as well as or better than the Spectralon. 90° out of plane BRDFs didn't vary sufficiently to warrant their display. In 90° out of plane BRDFs one tends to miss any knowledge regarding concerns of specular reflections. As mentioned above the BRDF data plotted was taken at 8° from in-plane. Previous measurements were taken in-plane; the primary difference, from the data shown, is that they have a blind spot at the angle of incidence.

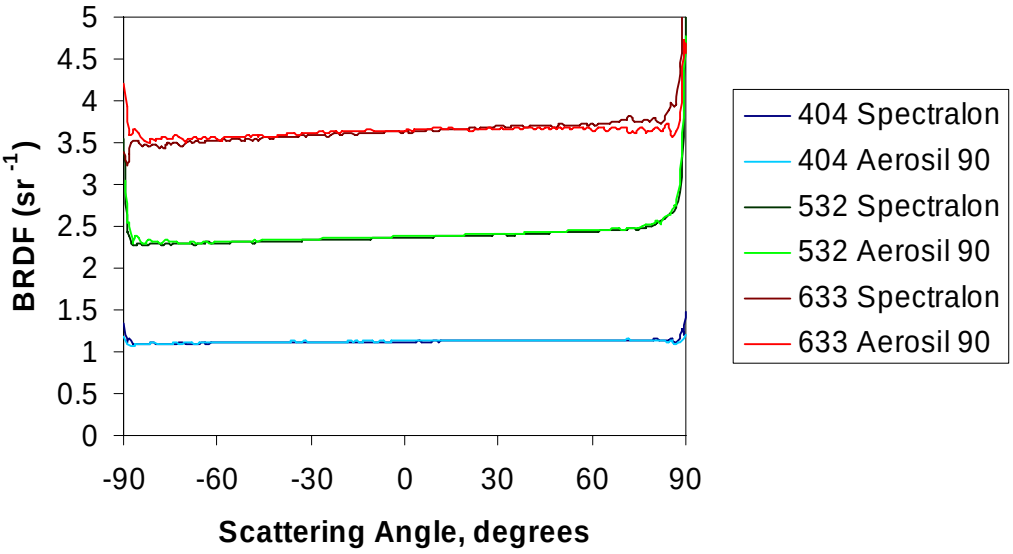

Fig. 40. BRDF, -30° incidence and perpendicular polarization. Data sets, for each wavelength, have been offset for the visual presentation

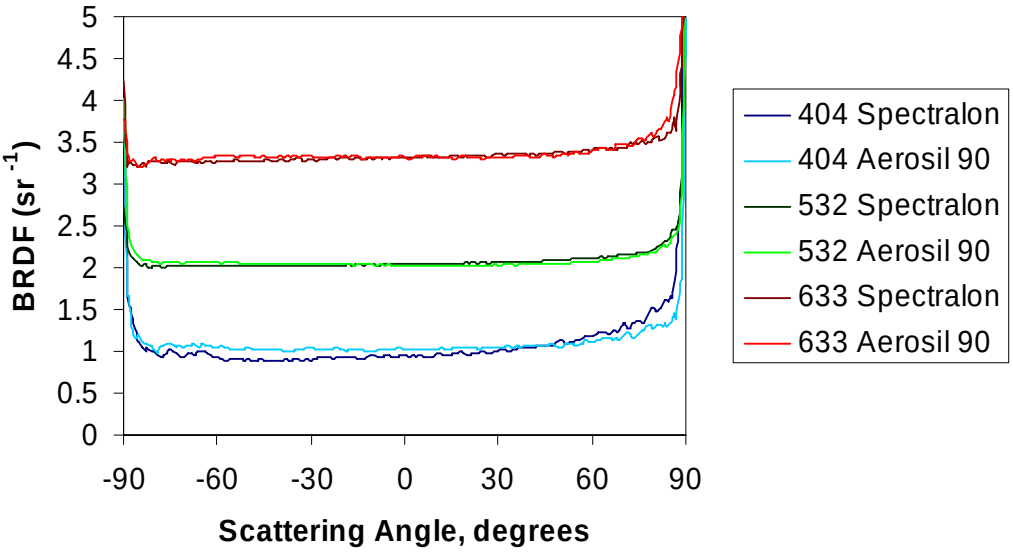

Fig. 41. BRDF, -60° incidence and parallel polarization. Data sets, for each wavelength, have been offset for the visual presentation.

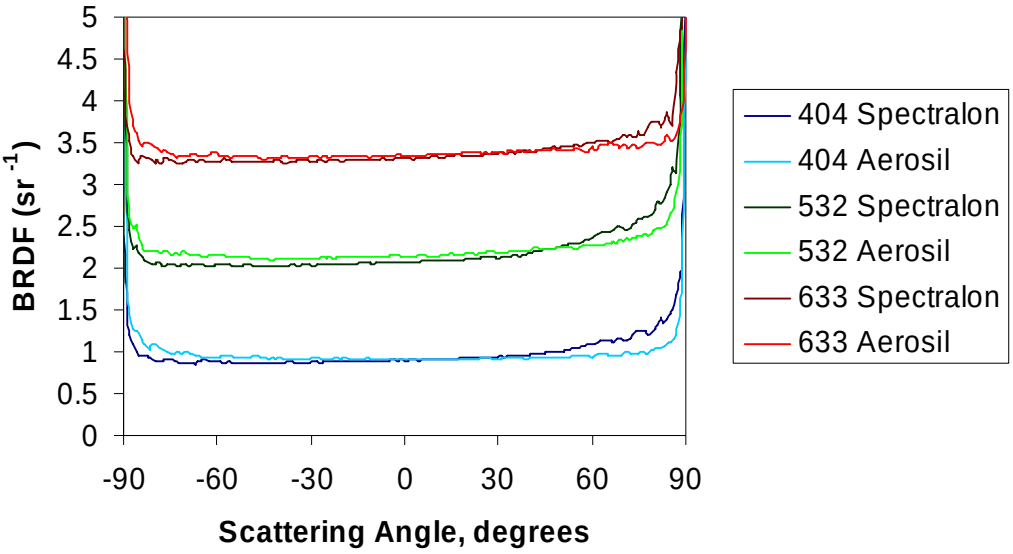

Fig. 42, BRDF, -60° incidence and perpendicular polarization. Data sets, for each wavelength, have been offset for the visual presentation.

In the flow-through ICAM the quartz powder and Spectralon will be held in place by a quartz tube. Thus, we need to know how a quartz sheet or a ground quartz sheet will affect the BRDF. In Fig. 43, the BRDF has been plotted for Aerosil 90 with no cover slide and Aerosil 90 with a cover slide having a ground surface facing the quartz powder. Not too surprising, the smooth upper surface of the quartz cover slide introduces some specular reflection upon the overall diffuse reflection of the underlying powder sample. This implies that it would take a few more reflections inside an integrating cavity with a smooth inner wall to achieve an isotropic homogenous light field from a well collimated beam. In the event of moderate to high absorption one should not expect to achieve a uniform light field from a Lambertian reflector placed behind a glass covering or like material. Moderate to high absorption is defined here to

be when the inverse of the absorption coefficient is of the same relative size as the diameter of the integrating cavity (cavity diameter ≈ 1/a). However, if one introduces the light in a manner which is already nearly isotropic and homogeneous the impact will be minimal, results demonstrating this will be presented Section 4.2.

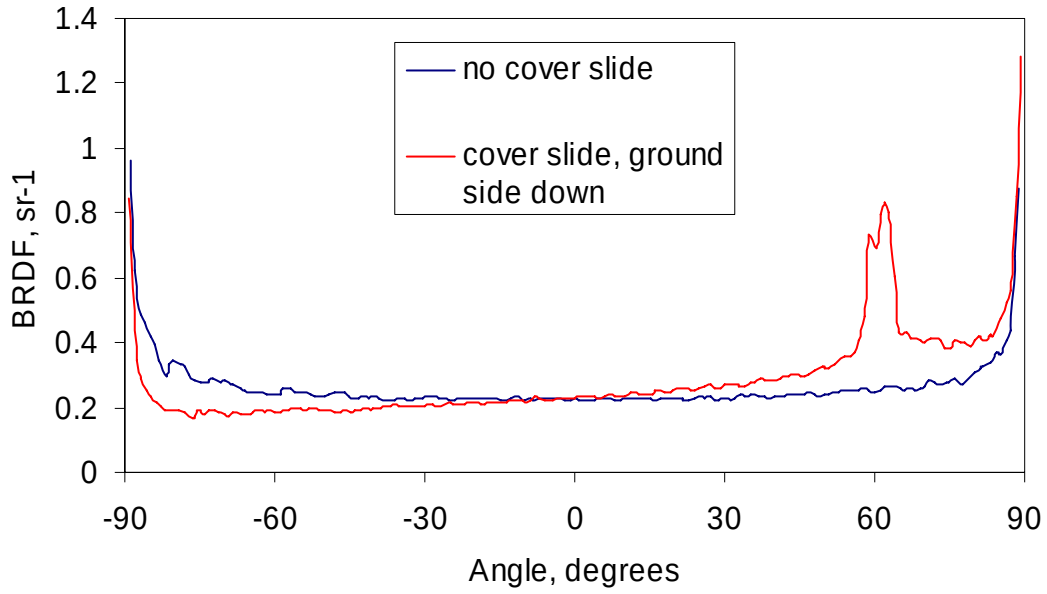

Fig. 43. BRDF showing the impact of a quartz cover slide over the Aerosil 90 powder. Data is taken at 404 nm, with -60° incidence and perpendicular polarization. The quartz cover slide has a ground surface facing the powder.

5. Measurement of the Absolute Reflectivity of Aerosil EG50

In Section 2.1, the well-known method for determining the absolute reflectivity of an integrating cavity was derived. It was shown that the decaying field of a temporally short pulse is related to the absolute reflectivity by Eq. (2.6), $\tau = -\frac{\bar{d}}{c \ln \bar{\rho}}$. Applying Eq. (2.51) for a cylinder with both the height and the diameter equal to 5 cm yields $\tau_{5\ \text{cm cyl}} = \frac{1}{9 \ln \bar{\rho}}$ ns. Thus one need only fit the trailing edge of the measured output pulse to determine τ_1, the time necessary for the pulse to drop to 1/e of its original value.

A second method can be used to fit the decay constant. Let us define the following terms:

T = the time from the start of the input pulse to the end of the output pulse

Δt = the time interval of the oscilloscope

N = the total number of intervals = $T/\Delta t$

n = the n^{th} interval

S_n = the amplitude of the input pulse at the time $t = n\Delta t$.

This method takes each interval of the input pulse and immediately begins to calculate the decay of it during an interval Δt. As more light comes in it sums it with the light remaining from the previous intervals and calculates its decay during the interval. Thus, the curve to be fit to the output pulse is

$$\mathrm{Fit}(t) = \sum_{n=1}^{t/\Delta t} S_n e^{\frac{-(n-1)\Delta t}{\tau_2}}, \qquad (3.20)$$

where τ_2 is the decay constant determined by this second method.

A cylindrical cavity 5 cm in diameter by 5 cm high was pressed out of baked Aerosil EG50. The cavity was pressed in two pieces. The first piece was shaped as a beaker and the second as a lid. The cavity walls were 5 cm thick. Light was introduced into the cavity with a 225 μm multimode fiber. An identical fiber was located 90° apart from the input fiber. The fibers were inserted between the lid and the walls of the cavity. From previous experiments it was determined this placement of the fibers behaves the same as cavities in which the fibers were inserted in the midpoint of the wall.

Hamamatsu 1P21 photomultiplier tubes were used as detectors. The 532 nm input pulse was measured by detecting the evanescent wave as the pulse passed through the fiber next to the detector. Any input fiber for the cavity is also an output fiber for the cavity; therefore, the signal measured from the input fiber is a convolution of the input pulse, the output pulse, and any back-reflections in the fiber. Light travels at approximately 20 cm/ns in quartz, hence the first back reflection of the input pulse's peak will have traveled down the ~ 60 cm fiber and back in 6 ns. This trip contains two reflections off the ends of the fiber. Thus its intensity will have decreased by a factor of 0.04^2 (the typical reflectivity at a glass-air interface) or $1.6*10^{-3}$ in 6 ns. Thus, only the output pulse is significant in mixing with the input signal on the detector. To determine whether the output pulse significantly affected the measurement of the input pulse, the input signal was measured directly from the exit of the input fiber, both prior to and after

the cavity measurements. These measurements showed that the output pulse had little impact on the measurement of the input pulse via the evanescent wave. During the 266 nm cavity measurements the input signal was monitored by detecting a reflection off of the face of the input fiber where the laser beam was coupled into the fiber. This pulse was in advance of the true input pulse entering the cavity by approximately 3 ns.

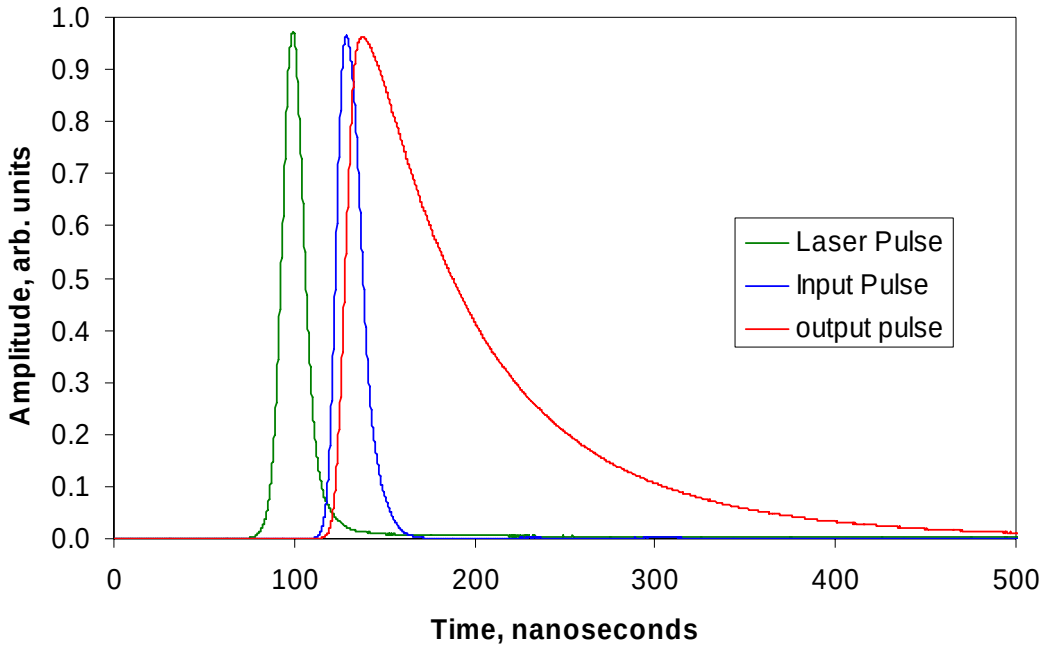

Fig. 44. 532 nm pulse in laser, pulse in fiber and output pulse from the cavity averaged 1024 times.

Laser pulses, 10 - 20 ns wide at 532 nm and later at 266 nm, were injected into the cavity. The Continuium Powerlite 9010 laser has a repetition rate of 10 Hz, thus there is no overlap between pulses within the cavity. An average of 1,024 laser shots at

532 nm are shown in Fig. 44 along with the cavity's response. The output pulse was multiplied by a scale factor so that it could be more easily compared to the input pulse.

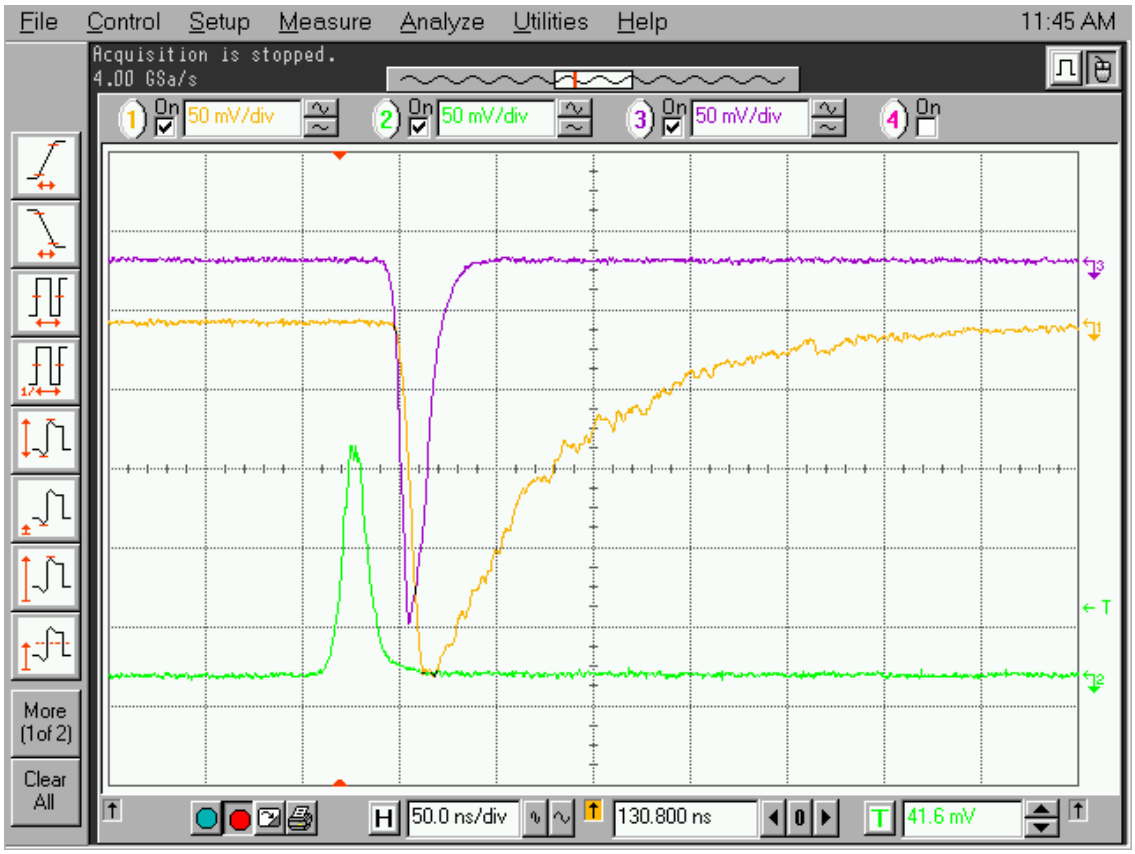

Fig. 45. Single pulse shot. The green pulse is from the laser cavity, the purple pulse is from the input fiber, and the gold pulse is the output pulse from the integrating cavity.

Fig. 45 is the oscilloscope trace of a single shot at 532 nm. In Figs. 46 and 47 the two fits for the cavity response at 532 nm are shown. At 532 nm $\tau_1 = 68$ ns and $\tau_2 = 66$ ns. Recall that τ_1 is the fit to the exponential tail of the output pulse and τ_2 is the fit to

the full output pulse. For the full curve fit the input pulse was shifted by 3 ns. Both fitting methods yield an average cavity reflectivity of 0.998. This is, to the author's best knowledge, the highest diffuse reflectivity ever measured at 532 nm.

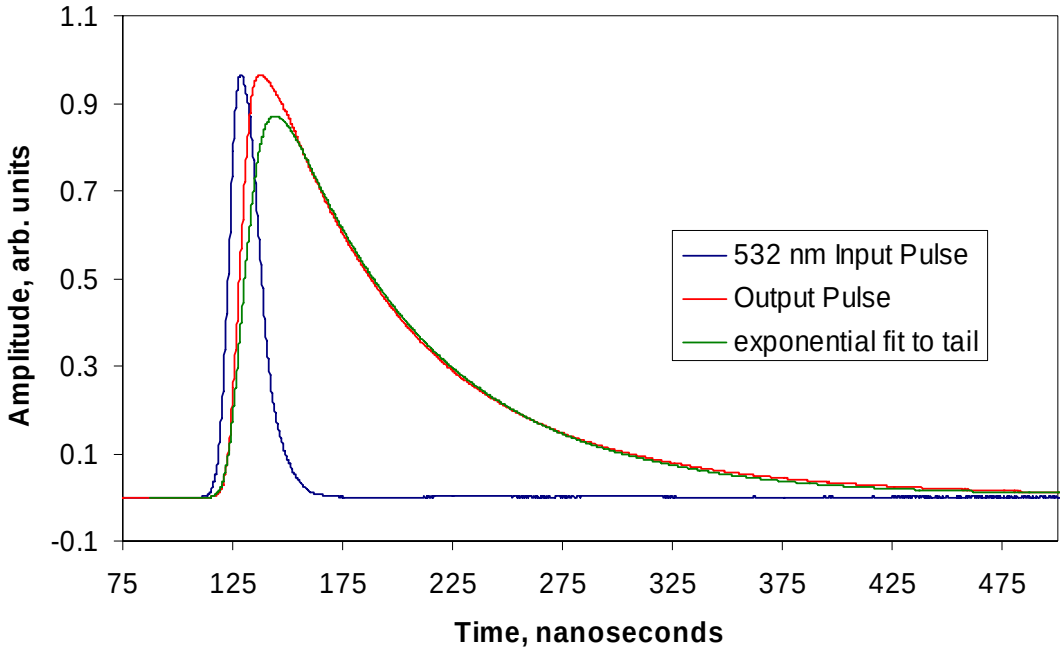

Fig. 46. Exponential fit to the output pulse's tail at 532 nm, $\tau_1 = 68$ ns.

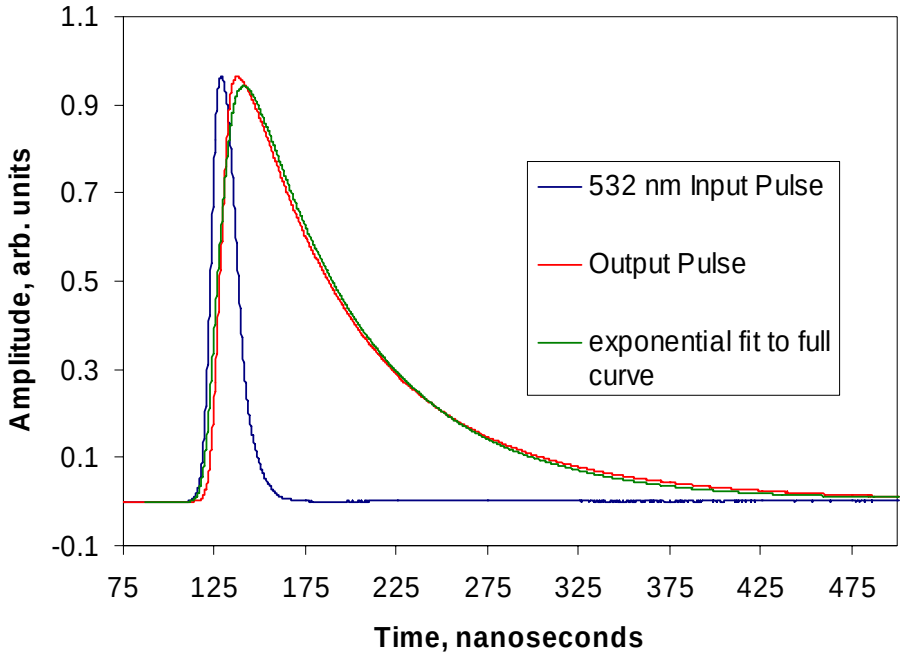

Fig. 47. Exponential fit to entire curve at 532 nm, $\tau_2 = 66$ ns.

When taking the data for the absolute reflectivity at 266 nm a different oscilloscope was used. This prevented the capture of all three pulses at once on the oscilliscope. To adjust for this, the pulse internal to the laser cavity was used as the trigger as well as a determination of the timing between the fiber input pulse and the cavity output pulse. In Figs. 48 - 50 the data for the 266 nm response is shown. At 266 nm $\tau_1 = 28.5$ ns and $\tau_2 = 31$ ns, thus both fitting methods yield an average reflectivity in the cavity of 0.996. This is, to the author's best knowledge, the highest diffuse reflectivity ever measured at 266 nm.

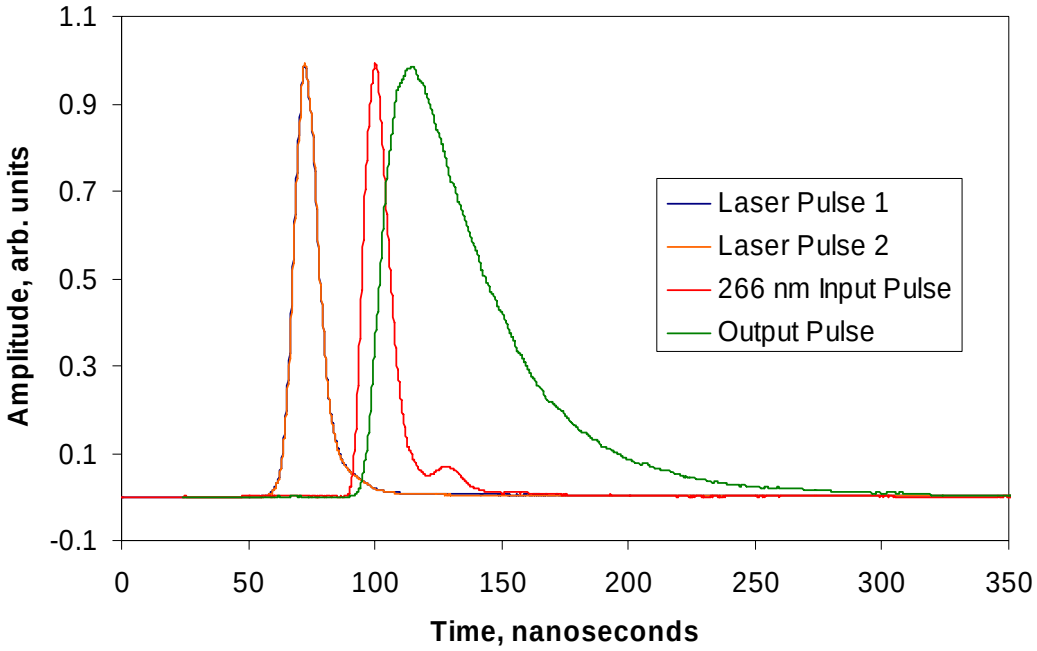

Fig. 48. Laser cavity pulse, input fiber pulse and cavity output pulse for the 266 nm absolute reflectivity measurement. Laser pulse 1 and laser pulse 2, which overlap identically, were used to determine the timing correlation between the fiber input pulse and the cavity output pulse.

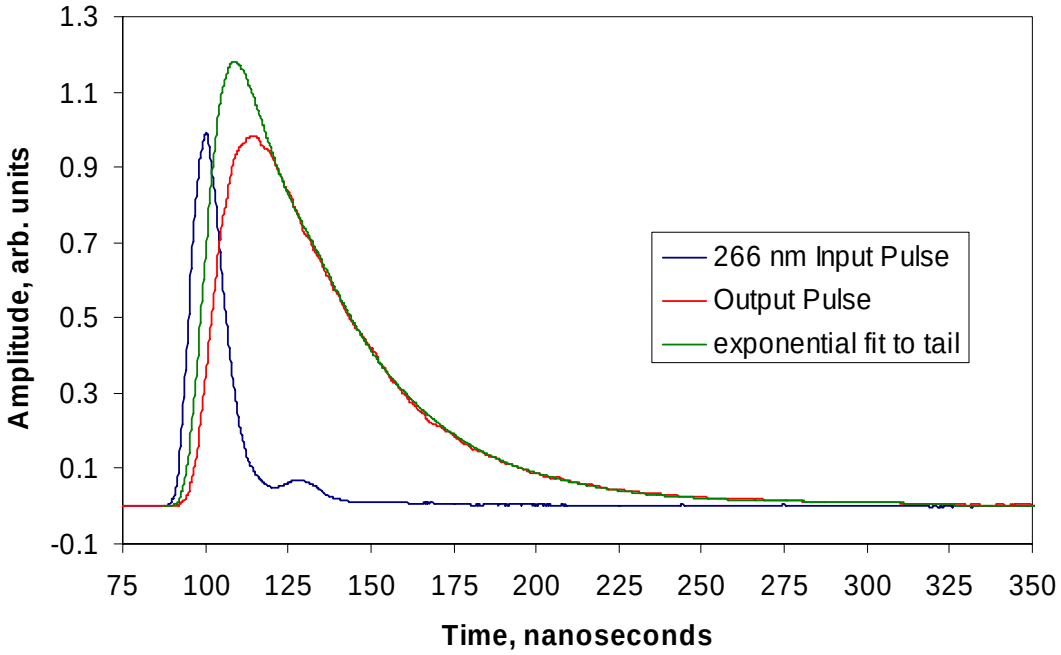

Fig. 49. Exponential fit to tail for the absolute reflectivity at 266 nm, $\tau_1 = 28.5$ ns.

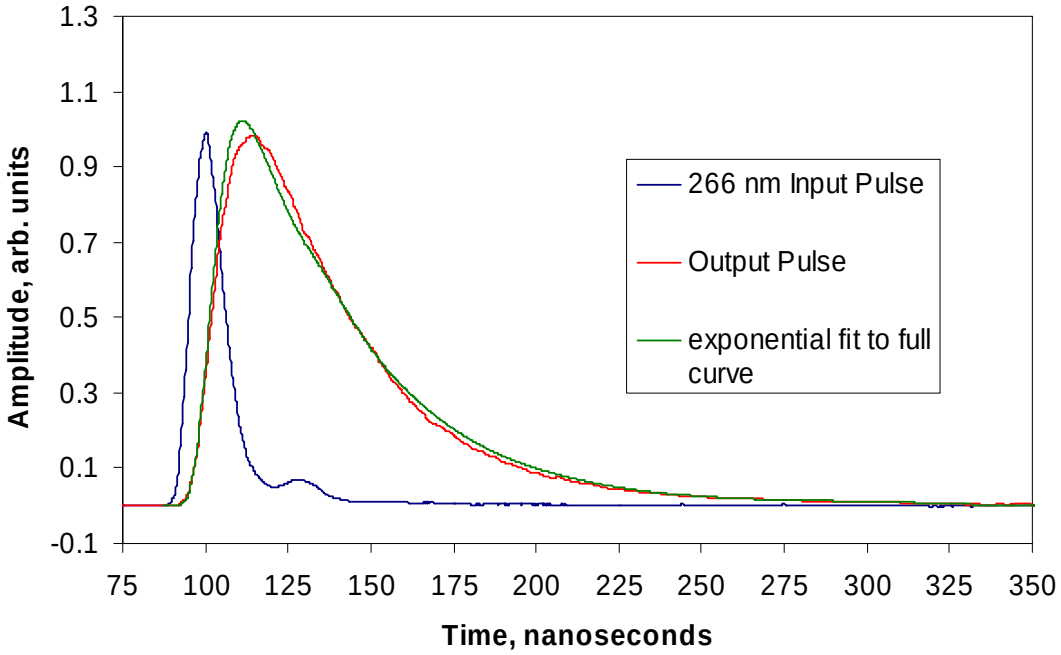

Fig. 50. Exponential fit to entire pulse for the absolute reflectivity at 266 nm, $\tau_2 = 31$ns.

CHAPTER IV

FLOW-THROUGH INTEGRATING CAVITY ABSORPTION METER

1. Design of the Flow-Through ICAM

The length of the prototype design is longer than that which was suggested to be optimal by Gray et al.[13,14] This was done in part so that we can experimentally monitor the absorption signal as a function of its distance from the end of the tube. The sample flows through a 122 cm long quartz tube which has a 2.54 cm inner diameter. The quartz tube has a ground outer surface to aid in diffusing the light field. The inner surface has not been altered so as to aid in cleaning and to prevent fouling in natural waters. The quartz tube is surrounded by two cylindrical diffuse reflectors separated by a small air gap, see Fig. 51. The cylindrical reflectors are 102 cm long. The inner diffuse reflector has a 6 mm wall thickness and is made from Spectralon. It has an albedo of 0.992. The second diffuse reflector is made from a 2.54 cm thick layer of Aerosil 90, its albedo is ~ 0.997. The width of the air gap separating the two layers is 2.54 cm. The choice to use Spectralon for the inner diffuse reflector was made prior to our development of the quartz powder reflectors. The light is introduced into the air gap between the two diffuse reflectors. Six separate wavelengths were used to span the visible spectrum, see Fig. 52. For the prototype we used 6 LEDs per wavelength on each end of the ICAM. The light that is transmitted through the diffuse wall, from this outer

integrating cavity and into the inner integrating cavity, produces an isotropic and homogeneous field in the inner cavity.

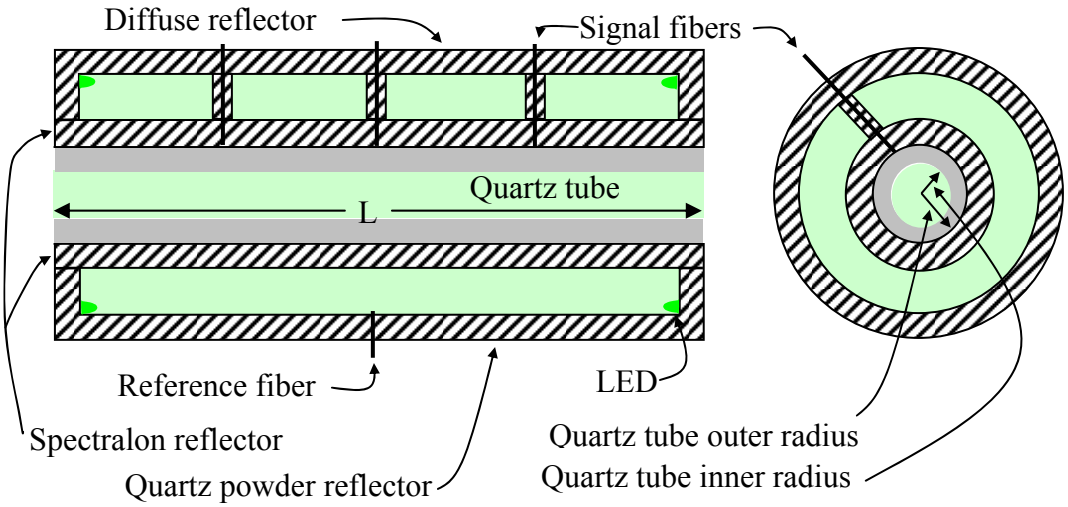

Figure 51. Flow-through ICAM design.

A 1 mm plastic fiber optic cable, Lumileen PRM 1640,* is placed in contact against the outer wall of the quartz tube to sample the intensity in the inner cavity. The fibers were located at 5.2 cm, 10.5 cm, 27.5 cm, 37 cm, and 50 cm respectively from the end of the diffuse reflector. An identical fiber is located at the midpoint of the outer cavity to measure a reference signal. These fibers are sheathed to prevent unwanted

---

*Lumileen PRM-1640 is a discontinued product of Poly-Optical Products, Inc., a division of Lumitex, Inc., Irvine, CA.

light from coupling into the fiber. The Absorption signal is taken to be the signal from the inner cavity divided by the signal from the outer cavity. The output of the signal fiber is passed through a neutral density filter wheel to prevent saturation of the Hamamatsu 1P21 photomultiplier tube. Depending on the position of the filter wheel, the transmission of the signal fiber to the PMT is 0%, 10%, 32%, 50%, 79%, or 100%. Neutral density filters are used to limit the transmission of the reference fiber to 0.1% when the ICAM is illuminated with the 443, 465 and 525 nm LEDs and to 10% when the ICAM is illuminated with the 570, 595 and 609 nm LEDs.

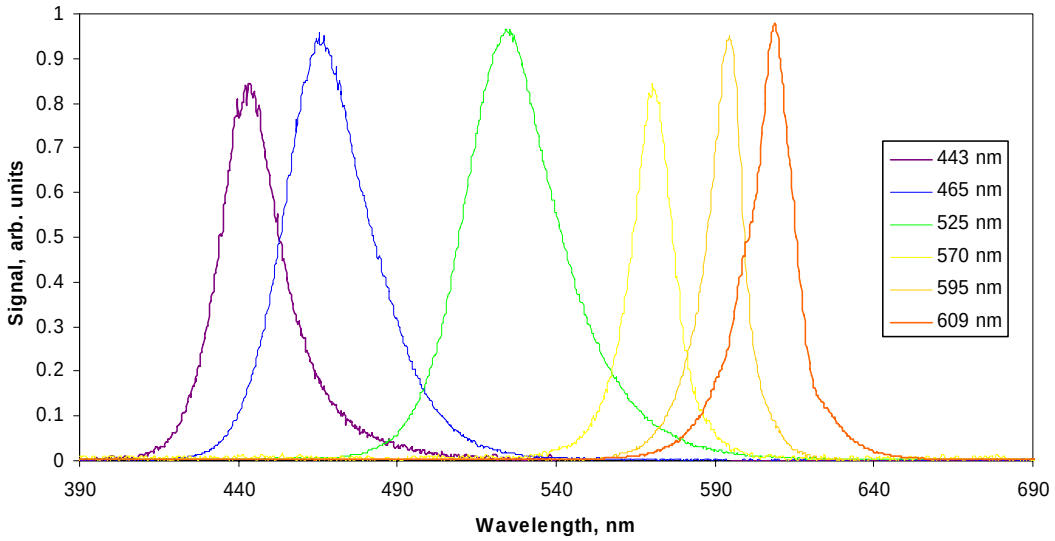

Fig. 52. LED spectrum.

2. Uniformity of the Light Field

A 1mm plastic optical fiber was sheathed inside a thin wall stainless steel capillary tube and used to test the uniformity of the light field in the inner cavity. The stainless steel tube insures the light can only couple into the fiber through its end face. The fiber has a small 90° bend at the end. Of course introducing the stainless steel capillary tube into the cavity will disturb the field to some degree. In Fig. 53, a plot of the intensity is shown as it was measured along the length of the tube, at the bottom of a cross section of the tube, while looking radially inward toward the center of the tube. The two pronounced peaks indicate the location of the LEDs. The distance is referenced to the location just before the first set of LEDs. The middle 50 cm of the light field appears relatively uniform. In Fig. 54 the intensity vs. the direction of the detector is shown. This measurement is from the bottom of a cross-section of the tube located at the midpoint along the tube's length. Notice how the light field is independent of the viewing direction.

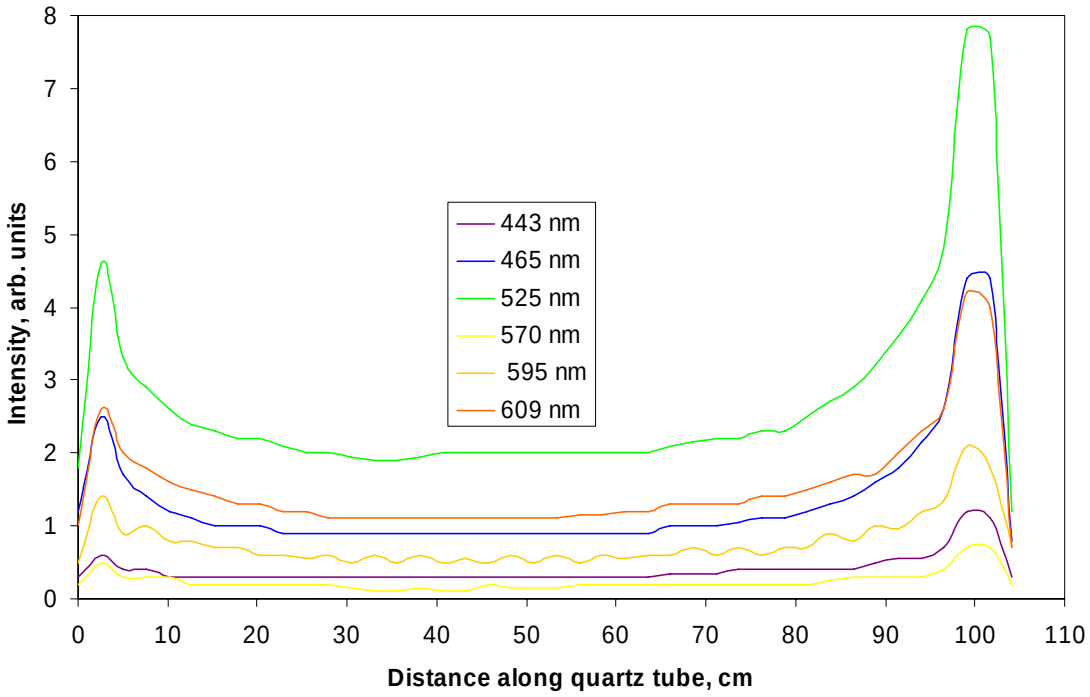

Fig. 53. Longitudinal inspection of the uniformity of the light field in the ICAM.

Fig. 55 displays the results of a measurement of the intensity vs. the height of the detector. This measurement was taken at the midpoint of the tube. One will notice that the first data point comes from a height of 1 cm; this is an artifact of the 1 cm length of the bend in the optical fiber used to sample the light field. One can see that the field is uniform in the middle of the tube both as a function of the radial position and sampling direction. These measurements were made with a background medium of air.

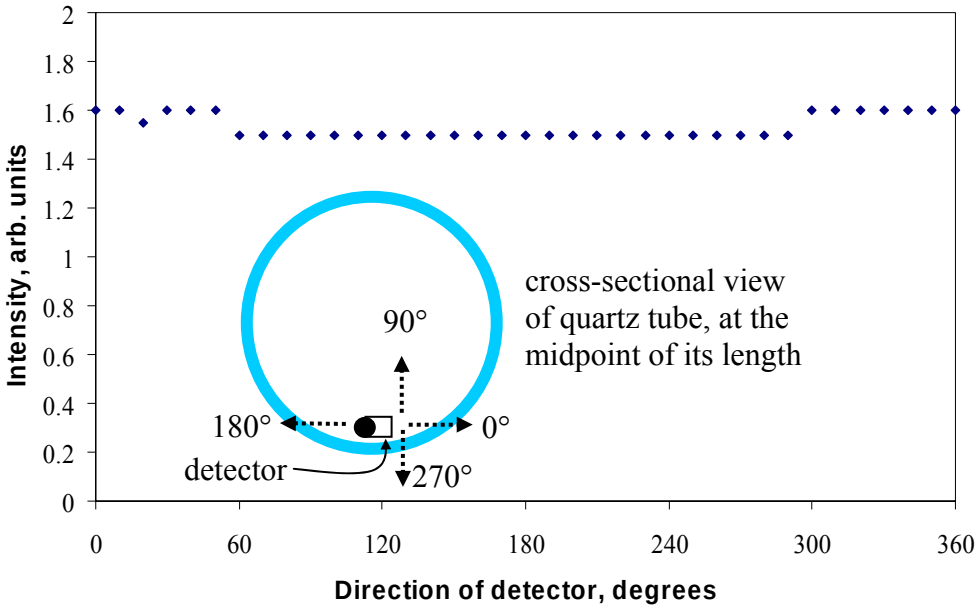

Fig. 54. Uniformity of the field in the cavity as a function of viewing angle.

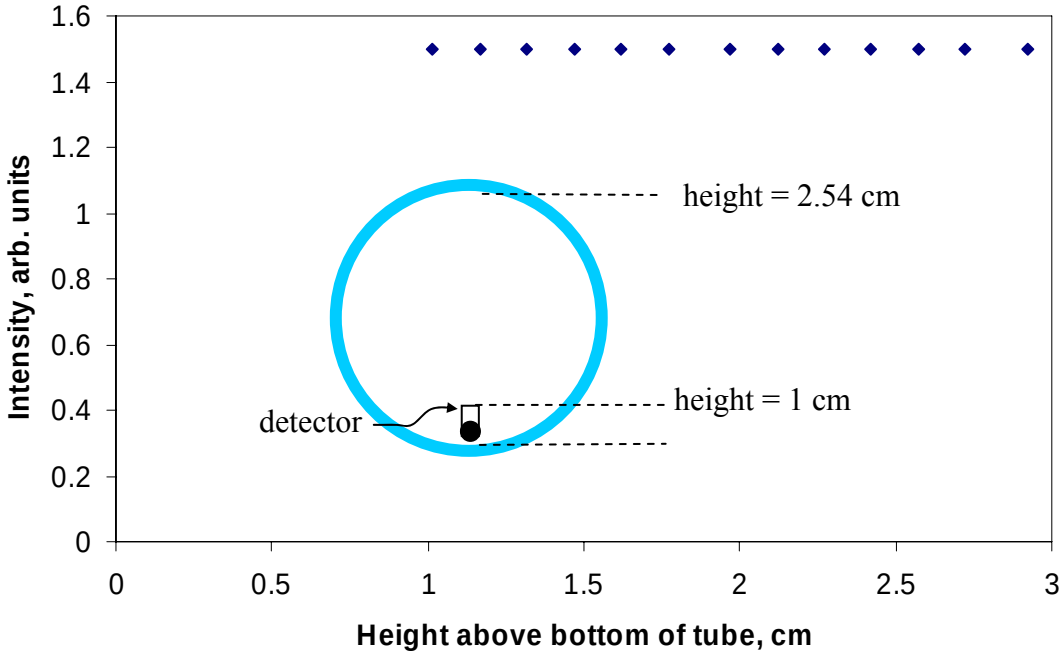

Fig. 55. Uniformity of the light field in the cavity as a function of the radial position.

Consider a spherical coordinate system with the origin located at the exact center of the tube, and the direction of the ray along $\theta = 0$ to point along the axis of the tube. With this reference frame in mind we discuss the nature of the homogeneity of the field. The absorption of rays traveling across the quartz tube is significant when the absorption increases to a level in which the inverse of the absorption coefficient is of the order of the tube's diameter. If one were located at the origin of the spherical coordinate system and looked in the direction along ($\theta = \pi/2$, ϕ_o) one would still see a uniform intensity of light regardless of ϕ_o. If one were to look at another angle, e.g. along (θ_o, ϕ_o), one would again see a uniform intensity regardless of ϕ_o. One would not see a uniform intensity if θ_o is varied. As θ_o varies the path length the photon travels varies, and in a highly absorbing medium this will produce nonuniformity in the radiance. One should also note that the field will vary as a function of the radial position from the centerline of the tube. Although the radiation field is varying there is still a great deal of symmetry in the field. The radiant energy sampled by a detector located on the cylinder wall at the midpoint of the tube is independent of ϕ. There is no position at the midpoint of the tube wall which would introduce some asymmetry in the ICAM's detected signal. This is not true for integrating cavities which introduce the light in an asymmetric manner.

3. Calibration Procedure

The ICAM was calibrated using solutions of "pure" water and irgalan black. For our purposes "pure" water will be taken to mean water purified by a Milli-Q®* system to less than 3 ppb total organic content and greater than or equal to 18 MΩ-cm of resistance. The full dye solution consists of 112 mg of irgalan black in 4 liters of "pure" water. The irgalan black powder is mixed with 150 ml of "pure" water. This solution is then placed in a sonic bath and then filtered through a qualitative P5 filter. The filtered dye solution is then mixed with 3.85 liters of "pure" water. The full dye solution is repeatedly cut in half by volumetric dilution with "pure" water until a solution with a concentration of $1/1024^{th}$ of the original irgalan black solution is produced. The absorption spectrum of irgalan black is shown in Fig. 56. The absorption coefficient of the full dye solution was measured by a SpectraMax Plus^{384} absorption spectrometer**. The absorption of each sample is determined as follows, $a_{\text{nth dilution}} = \frac{1}{2^n} a_{\text{full dye}} + \frac{2^n - 1}{2^n} a_{\text{"pure" water}}$, where n = 1 is the first dilution of the fully concentrated solution. We took $a_{\text{"pure" water}}$ as that as measured by Pope et al.[12]

---

* Milli-Q® is produced by the Millipore Corporation, Billerica, MA.

** SpectraMax Plus^{384} is produced by Molecular Devices Corporation, Sunnyvale, CA.

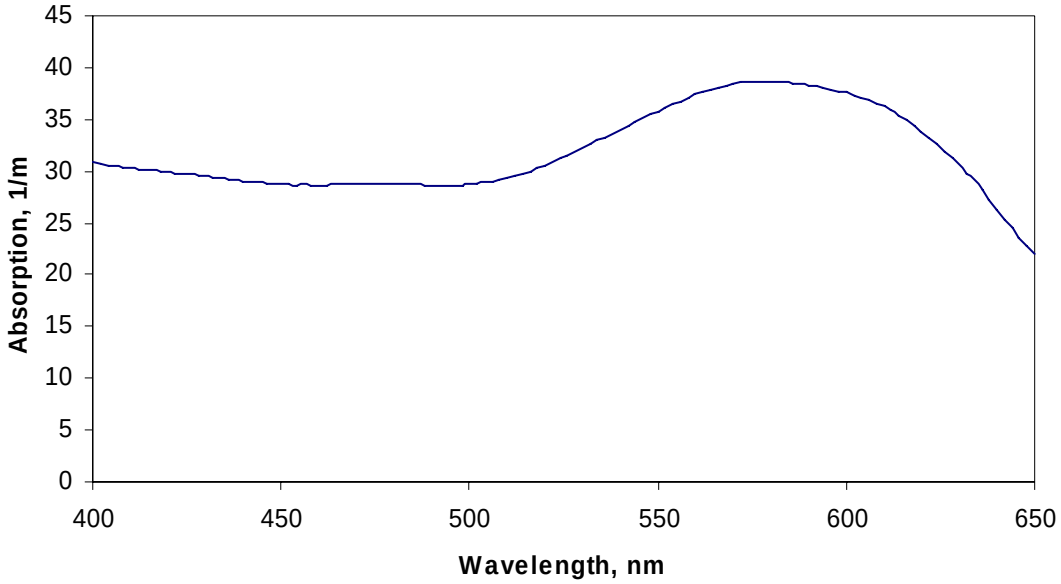

Fig. 56. Absorption spectrum of irgalan black.

The ICAM measures the absorption of solutions in either a static or a flow through manner. The data presented in this dissertation has been measured in a static manner except for the flow rate data in section 4.5. As section 4.5 indicates, this does not alter the data significantly. The ICAM requires a 1 liter sample. The ICAM is held in a vertical position throughout the measurements to prevent trapping of air bubbles along the tube. *In Situ* absorption meters are typically operated vertically for similar reasons as well as to prevent settling out of particulates on the walls of the device. Each sample was loaded into the ICAM from the bottom by a manometer-type device to minimize the introduction of air bubbles to the ICAM. After a "pure" water sample was measured by the ICAM each dye solution was then measured, beginning with the least concentrated. Figs. 57 - 62 show the absorption signal vs. the absorption coefficient.

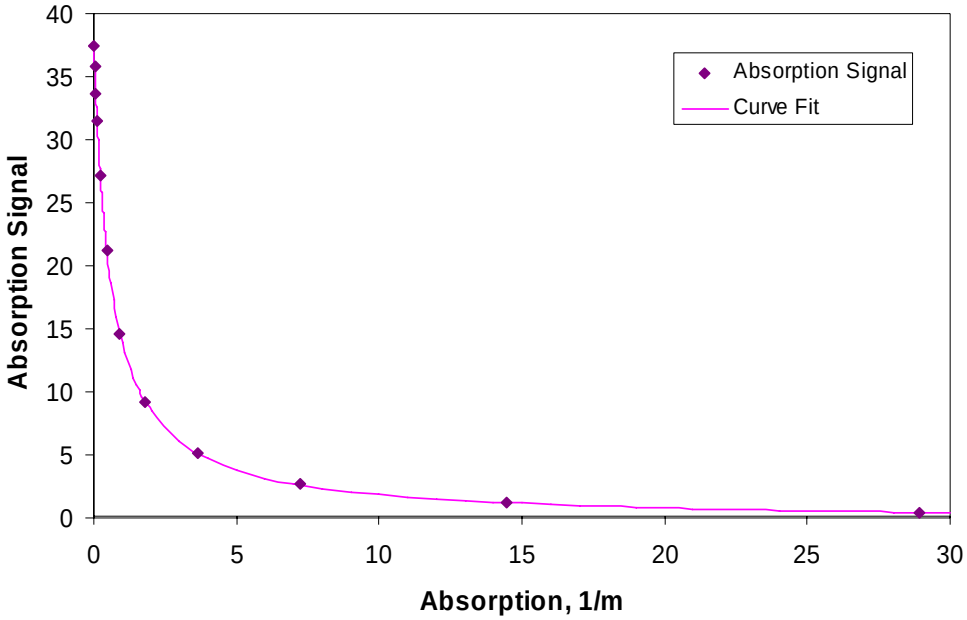

Fig. 57. ICAM response at 443 nm.

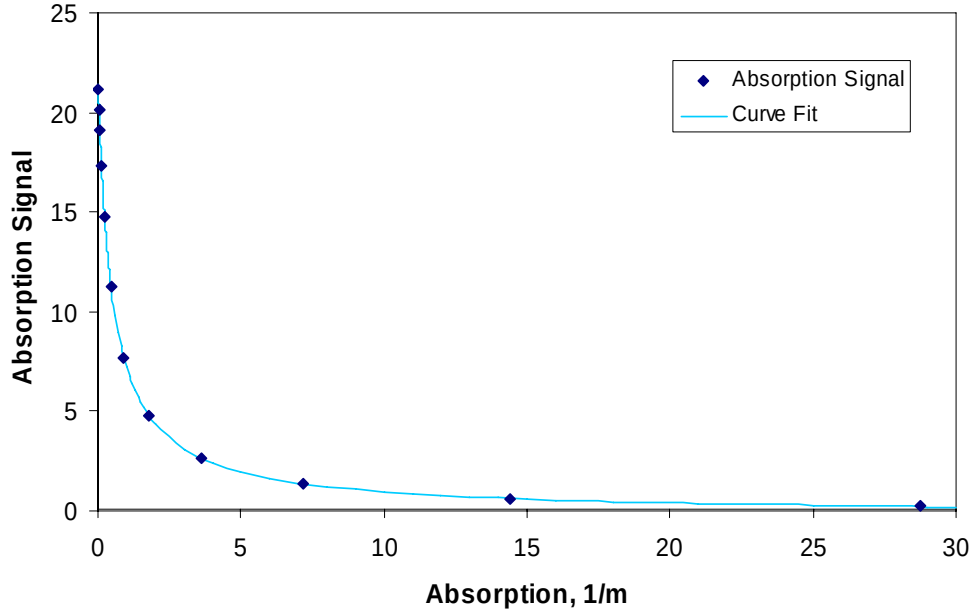

Fig. 58. ICAM response at 465 nm.

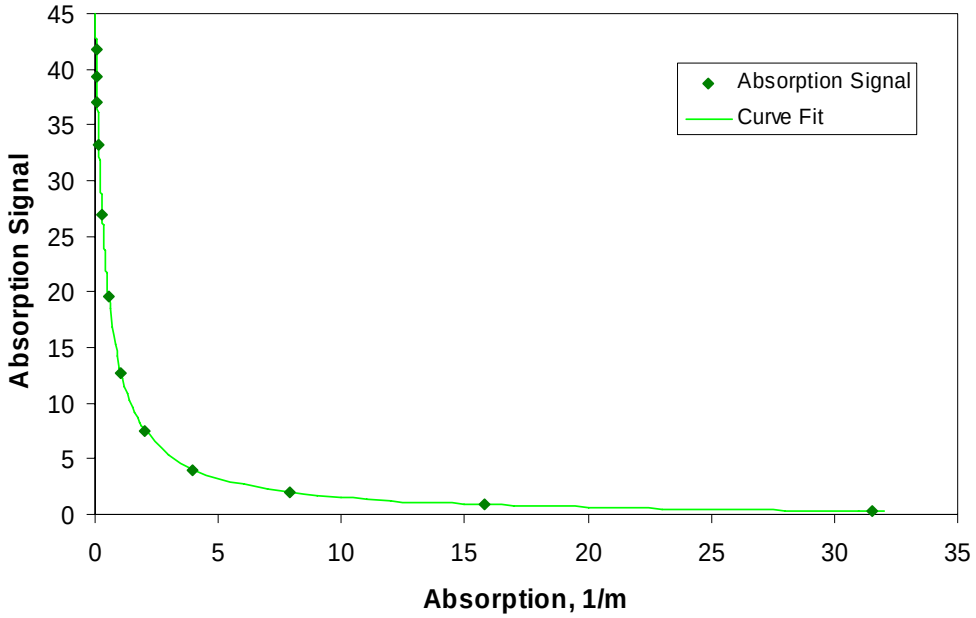

Fig. 59. ICAM response at 525 nm.

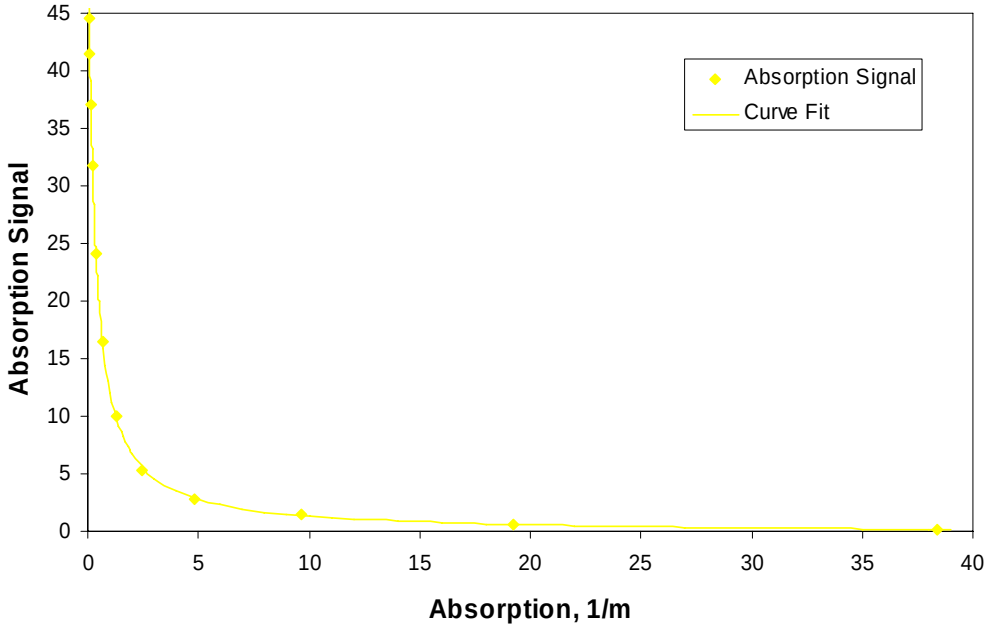

Fig. 60. ICAM response at 570 nm.

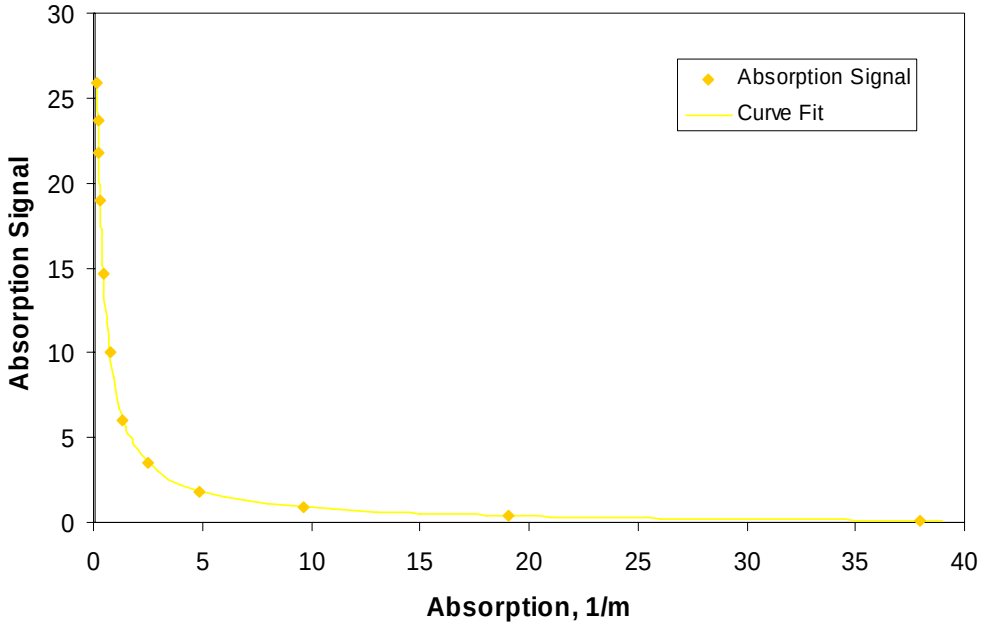

Fig. 61. ICAM response at 595 nm.

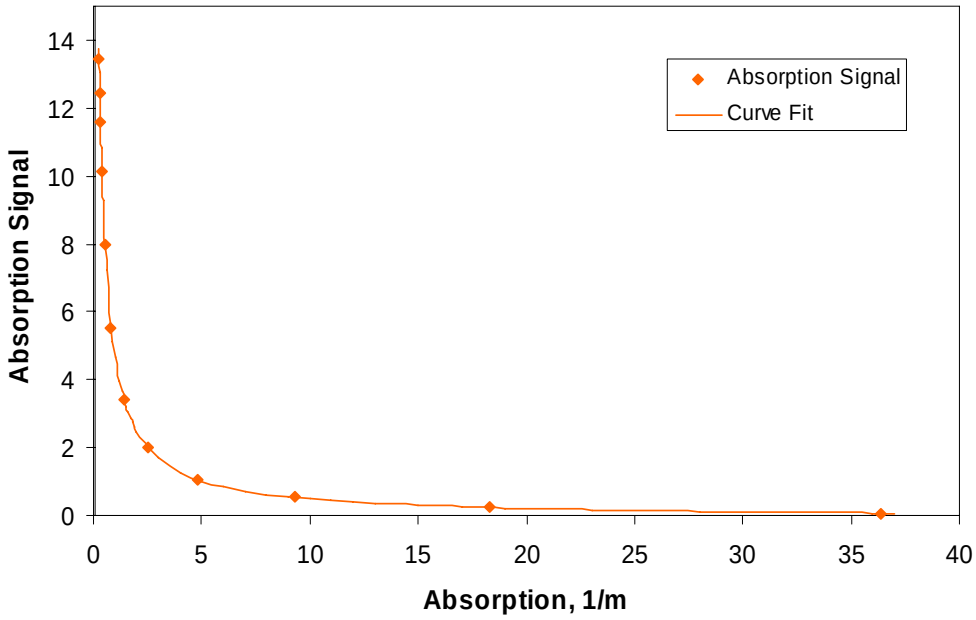

Fig. 62. ICAM response at 609 nm.

The data was fit with two different equations. The first fit was that described by Gray et al.[13,14],

$$S = \frac{m}{a + a_i} + b \tag{4.1}$$

in which S is the signal (signal fiber/reference fiber); a is the absorption coefficient; and a_i, m, and b are fitting parameters. The fits are outstanding. The fitting parameter a_i can be thought of as indicative of permanent loss mechanisms which are seen by the detector just as if they were an absorption baseline. For example, the quartz tube waveguides a nonzero amount of light out of the ICAM, and thus prevents that light from "sampling" the absorption level of the medium. The ICAM "sees" this loss of light just the same as if it were due to absorption. The fitting parameter b results from an offset in the signal. One source of this offset can come from the dark current of the PMT. Of course the dark current could be subtracted out to remove its contribution to this parameter. Other factors which affect b are the PMT's response curve, the coupling differences between the two fibers, and light reflecting back off the quartz tube directly into the signal fiber. The fitting parameter m describes the overall response of the ICAM and is primarily a function of the geometry of the cavity.

The second fit does not force the $(a+a_i)^{-1}$ relationship. Instead it allows the power factor to be fit by the data. The second fitting equation is

$$S = \left(\frac{m}{a + a_i} \right)^p + b\,. \tag{4.2}$$

A comparison between the two fitting equations is given in Table 3. As one can see the second fit is the better fit. Of course the fit with the parameter p = 1 is a little easier to

explain qualitatively; for if the cavity reflectivity was unity and no light escaped out the ends of the quartz tube one would expect the optical path length to be 1/a. It is interesting to note that the power parameter p from Eq. (4.2) is nearly 1. It should also be pointed out that although this calibration run only measured absorption coefficients out to 40 m^{-1}, the ICAM can measure higher absorption coefficients. Other calibration runs measured absorption coefficients out to 70 - 80 m^{-1}.

Table 3. Comparison between the two fitting methods.

	Fit 1	Fit 2		Fit 1	Fit 2
443 nm			465 nm		
a_i	0.596	0.598	a_i	0.510	0.459
m	22.65	22.83	m	11.05	10.63
b	-0.288	-0.356	b	-0.096	-0.243
p	1	0.9898	p	1	0.9306
R^2	0.9999	1.0000	R^2	1.0000	1.0000
525 nm			570 nm		
a_i	0.405	0.398	a_i	0.286	0.270
m	18.91	18.77	m	16.13	15.66
b	-0.307	-0.303	b	-0.303	-0.246
p	1	0.9899	p	1	0.989
R^2	.9999	1.0000	R^2	0.9997	0.9998
595 nm			609 nm		
a_i	0.216	0.150	a_i	0.142	0.0815
m	10.02	9.20	m	5.53	5.13
b	-0.160	-0.194	b	-0.089	-0.108
p	1	0.9294	p	1	0.9321
R^2	0.9999	0.9999	R^2	0.9998	0.9999

4. Blind Measurement Test

A blind test of the ICAM was performed in order to ascertain the reliability of the ICAM. A dye solution was mixed up as per the standard calibration procedure. A fellow graduate student, Jeffrey Katz, then discreetly added an additional volume of "pure" water to the master solution. The true value of the absorption of the master solution can only be determined with knowledge of this additional volume of "pure" water. A range of volumetric dilutions were then produced from this master solution. The absorption signal was then measured for all of the samples. The amount of water added to the master solution was revealed after the absorption coefficients were calculated from the absorption signals. Table 4 reveals the results of the blind test. Except for the sample with a = 0.0702 m^{-1} the results are remarkable. One should keep in mind that water with an absorption coefficient of 0.0702 m^{-1} is impossible to keep at 0.0702 m^{-1}. Leaving such a sample in a chemically cleaned quartz container overnight will alter the measurement.[27] The contamination from the oil of a fingerprint on a quartz container filled with 1 liter of "pure" water (a_{443} = 0.007 m^{-1}) is enough to increase the absorption over an order of magnitude.

Table 4. Blind test of ICAM.

	true absorption (1/m)	measured a (1/m)	% error
443 nm	0.070	0.079	12.15
	0.260	0.262	0.82
	1.018	1.000	1.70
	4.050	4.021	0.73
	8.094	8.014	0.98
525 nm	0.111	0.114	3.11
	0.317	0.319	0.70
	1.142	1.174	2.77
	4.444	4.418	0.59
	8.847	8.747	1.13
609 nm	0.343	0.345	0.73
	0.579	0.582	0.50
	1.526	1.508	1.15
	5.312	5.364	0.98
	10.360	10.420	0.58

5. Hardware Issues

It is not uncommon for instruments to have a warm up period or to experience signal drift. Tests were conducted to determine if any signal drift occurs. The absorption signals for three different levels of absorption were measured over a ten minute period. The samples were then diluted by 10% of their volume and then re-measured with the ICAM. The results for the 525 nm data are shown in Fig. 63 and are characteristic for the data from each set of LEDs. We could see a small drift in the PMT's signal throughout the ICAM's testing. The cause was due to drifts or noise between the two

PMTs. This irregularity only proved problematic when dealing with the cleanest of waters ($a \leq 0.09\ m^{-1}$). This has been resolved by measuring both signals on a single PMT.

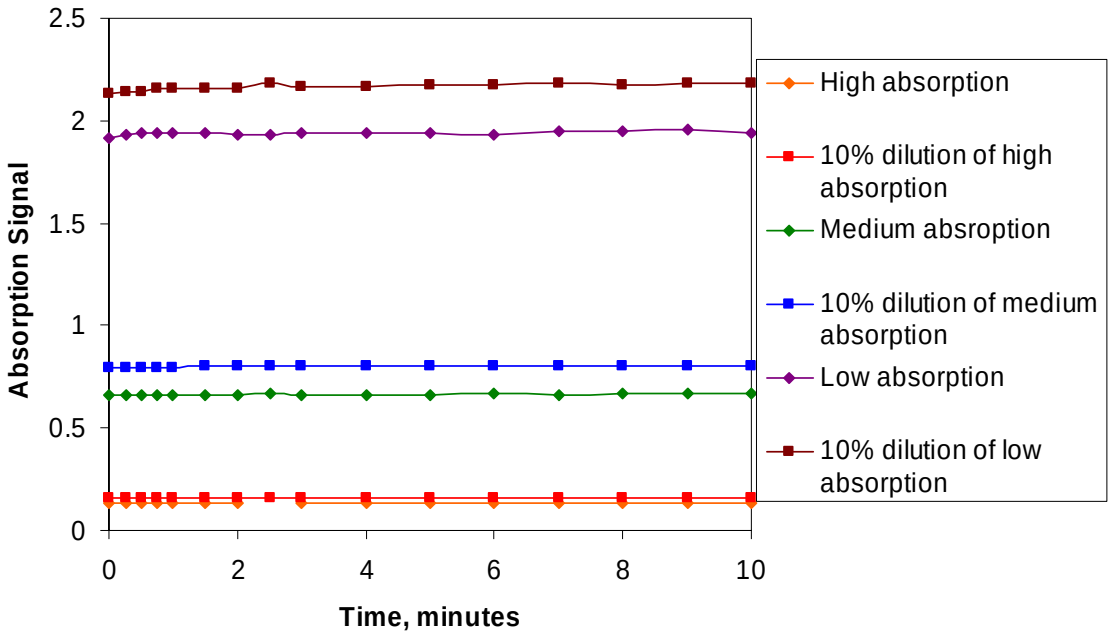

Fig. 63. Signal stability of the ICAM. The absorption signal has been scaled so that all three absorption levels can be seen on one graph.

The absorption signal vs. the LED voltage was investigated to insure that there are no saturation problems with the PMTs. One can see in Fig. 64 that once the voltage is sufficient to drive the LEDs (~10 V) the slope is nearly zero. This indicates that there is no saturation occurring in the PMTs. The slight rise of the slope from horizontal can be explained by the behavior of the LEDs. The wavelength of an LED is both a function

of its driving current as well as the ambient temperature. From 10 V to 24 V the driving current of the LEDS goes from 100 mA to 240 mA. Since the response of the ICAM is slightly dependent on the driving current, the LEDs are always operated at 240 mA. A possible change in the hardware system under consideration is the use of a fiber-coupled halogen bulb to illuminate the ICAM rather than LEDs. This would remove any concerns regarding the warm-up cycle of the LEDs. In this case the wavelength selectivity will be provided with a filter wheel or monochromator.

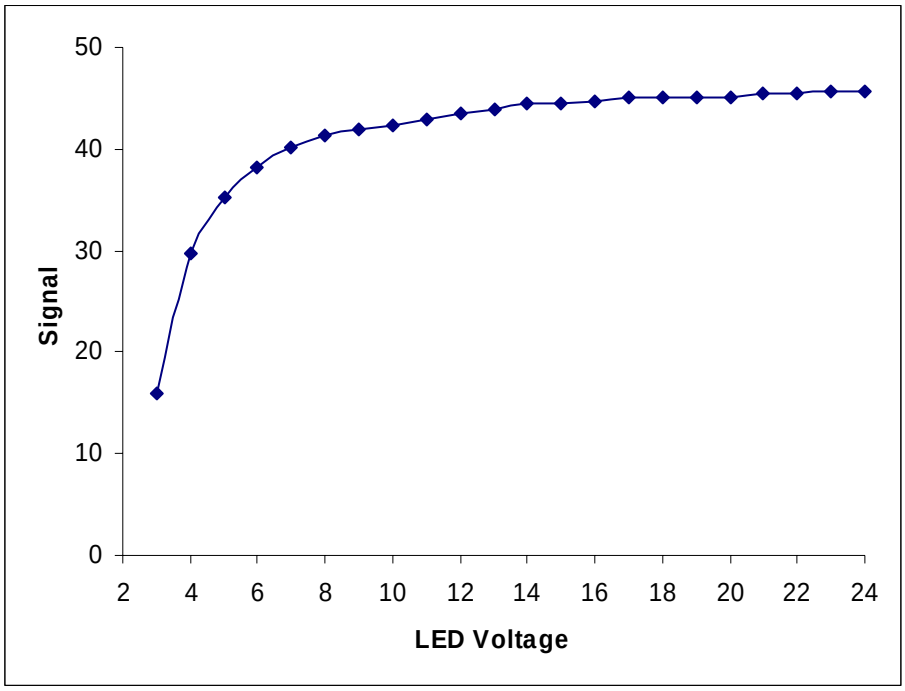

Fig.64. Absorption signal as a function of LED voltage.

Absorption instruments which are adversely affected by scattering generally have to restrict the flow rate through the instrument to prevent any turbulence or density

fluctuations. If turbulence or density fluctuations are introduced into these devices light will scatter off of these inhomogeneities and dramatically alter the absorption signal. Thus, a test was conducted to determine the impact of the flow rate upon the ICAM's absorption signal. In Fig. 65 one can see that the flow rate has a negligible effect on the absorption signal. Further tests taken out to 333 ml/s showed less than 3% change in the absorption signal. It should be pointed out that these measurements were made with the two-PMT detection system and therefore include more signal drift than would measurements made in the present ICAM.

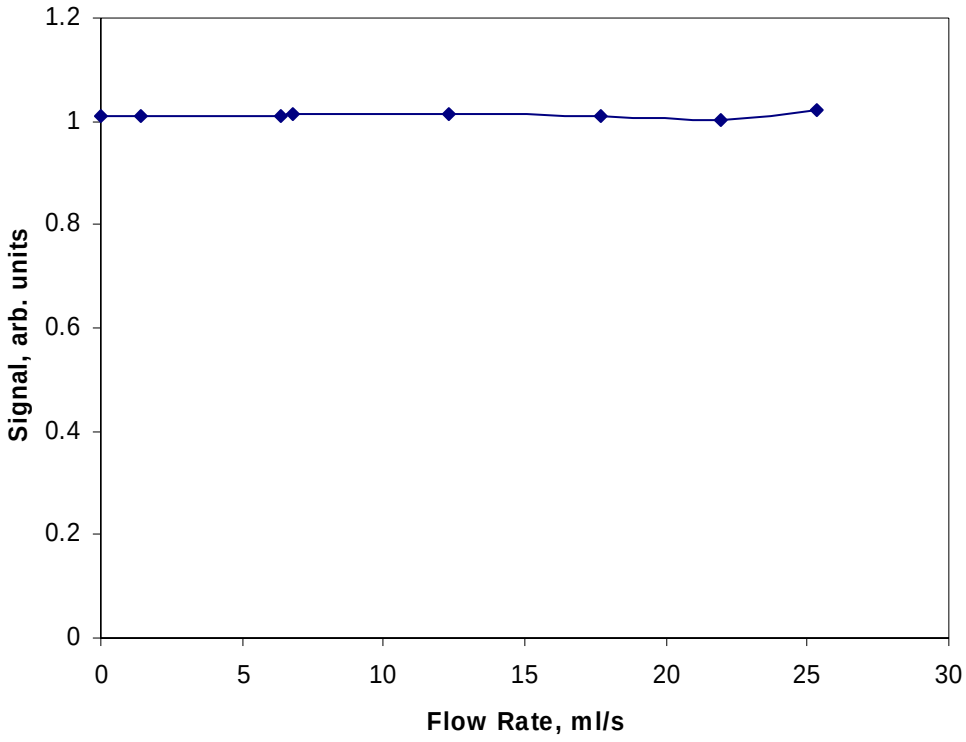

Fig. 65. Flow rate test of ICAM.

6. ICAM Signal vs. Scattering

Three sets of tests were carried out to determine the impact of scattering upon the ICAM. In the first two experiments, samples with respective absorptions of ~ 10 m^{-1} and ~ 45 m^{-1} were tested. At each of these absorption levels additional samples were produced by adding various amounts of polystyrene spheres (PSLs) to the samples. The PSLs increase the scattering coefficient of the sample with negligible increase in the absorption coefficient. Fig. 66 shows the measured absorption vs. the scattering coefficient. Clearly for mid to high levels of absorption the ICAM results are virtually independent of the scattering coefficient, just as predicted by Gray et, al.[13, 14] In fact the percent change in the measured apparent absorption was less than two percent for all of the data.

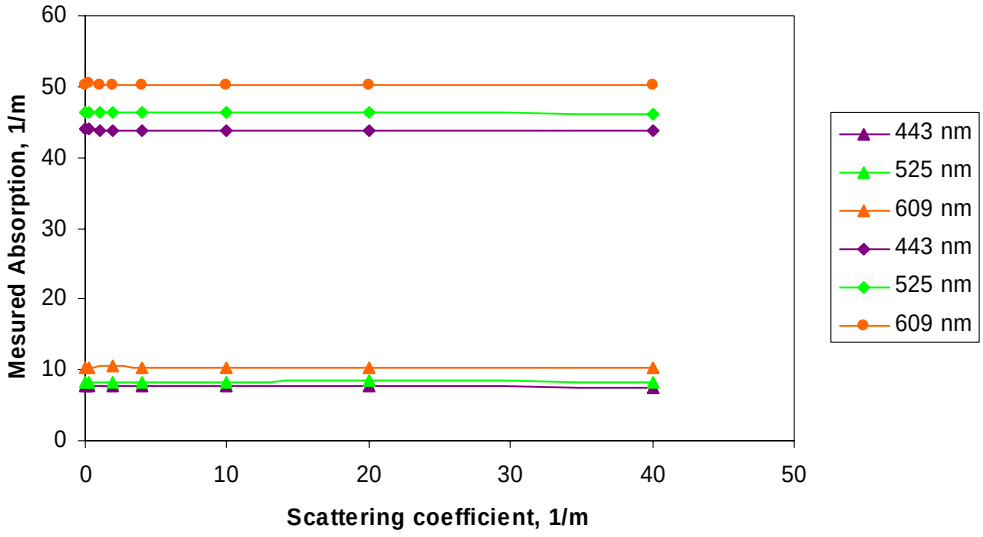

Fig. 66. Measured absorption vs. scattering for high and medium absorption levels.

The third experiment involved a low absorption sample, *i.e.* a ~ 0.3 m^{-1}. In this case separate samples were not prepared; instead, one sample was used in which additional PSLs were added to it while the sample was in the ICAM. This procedure required stirring the sample in the ICAM to ensure the PSLs were thoroughly dispersed. A clean glass rod was used for this purpose. The results are presented in Fig. 67. Again, one can see that the centrally located detector gives results that are nearly independent of scattering affects over the 0 to 40 m^{-1} scattering range. The measured apparent absorption coefficient, at 525 nm, had at most a 5% change in its value. The detector 5.2 cm from the end of the ICAM had a maximum 11% change in the measured apparent absorption coefficient. The central detector results are remarkable. Leathers et, al.[28] have pointed out that as scattering increases in a spherical integrating cavity the average path length will increase. Although the ICAM is not a closed cavity this could explain why we see an increase in the measured absorption coefficient at high scattering coefficients as each photon samples a greater path through the medium between wall reflections. At low scattering coefficients the response of the ICAM is more subtle.

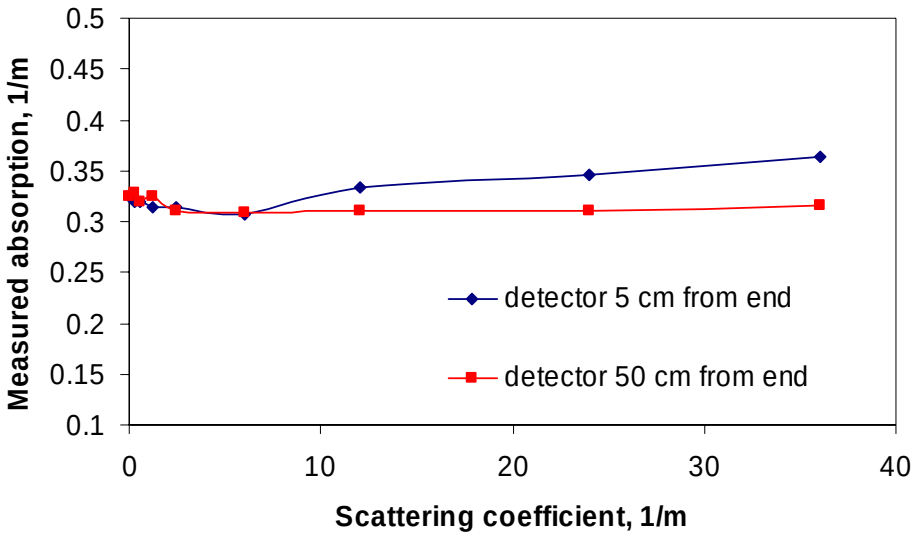

Fig. 67. Measured absorption at 525 nm vs. scattering at low absorption.

7. Error Analysis

In Section 4.3, in which we discussed the calibration procedure, we simplified the presentation, omitting some pertinent details. We were more concerned with communicating the general overview of the ICAM's operational features rather than getting bogged down in the minutiae of the calibration. Let us now get bogged down in the minutiae.

In Section 4.1 we said the ICAM was illuminated by 12 LEDs at 525 nm this was, of course, not quite true. Each LED may have a slightly different profile from the next due to manufacturing variances. The LEDs also have a finite spectral width $\Delta\lambda$. Thus it is not appropriate to simply use the absorption of "pure" water at 525 nm for calibration purposes. Instead the actual spectral output of each set of LEDs was

measured by an Ocean Optics USB2000* spectrometer directly from the inner cavity signal fiber. The spectrum of the LEDs was split into N subdivision 2.5 nm wide (the "pure" water data is in 2.5 nm wide increments). The absorption at the midpoint of each subdivision was then used to determine a weighted absorption value for "pure" water with each set of LEDs. The absorption coefficient for the set of 525 nm LEDs was determined by,

$$a_{525\ nm} = \frac{\sum_{n=1}^{N} h_n a_{\lambda(n)}}{\sum_{n=1}^{N} h_n}, \tag{4.3}$$

where h_n is the height of the n^{th} subdivision and $a_{\lambda(n)}$ is the absorption coefficient for "pure" water at the wavelength of the n^{th} subdivision. Further, when interpreting data from the ICAM, one should remember that they are not measuring the absorption at 525 nm, rather they are measuring the absorption within the spectral width of the LEDs which are centered at 525 nm.

Let us determine the uncertainty in the calibration data. We will concern ourselves just with the first fitting equation for this analysis. Recall Eq. (4.1), $S = \frac{m}{a + a_i} + b$, where m, b and a_i are fitting parameters. The uncertainty in the measured absorption of the dye solution propagates as follows,

$$\Delta S = -\frac{m}{(a + a_i)^2} \Delta a\ . \tag{4.4}$$

---

*Ocean Optics USB2000 is produced by Ocean Optics, Inc., Dunedin, FL.

To determine Δa we recall that each dye solution was volumetrically diluted from a full dye solution, whose uncertainty we know from the absorption spectrometer measurements. We shall call the uncertainty for the full dye solution δa_{fd}. We shall call the uncertainty from the "pure" water data δa_{pw}. To determine the uncertainty of the n^{th} dilution we first determine the absorption of the n^{th} solution,

$$a_n = \frac{a_{fd}}{2^n} + \frac{(2^n - 1)a_{pw}}{2^n} = \frac{V_{fd}}{V_T} a_{fd} + \frac{V_{pw}}{V_T} a_{pw}, \tag{4.5}$$

where V_{fd} is the volume of the original full dye solution in the n^{th} dilution, V_{pw} is the volume of "pure" water in the n^{th} dilution and V_T is the total volume of the solution. The uncertainty of the n^{th} dilution is $\Delta a_n = \frac{1}{2^n}\sqrt{\delta a_{fd}{}^2 + \left(2^n - 1\right)^2 \delta a_{pw}{}^2}$. Fig. 68 shows the calibration data with Δa and ΔS plotted.

Now we determine the uncertainty of an absorption measurement of the ICAM. One must consider other sources of error in the ICAM besides δa_{pw} and δa_{fd}. To determine an experimental uncertainty we first note that measurements of the signal fiber and the reference fiber were averaged over ten second time periods and were stable over such a period. The uncertainty of the oscilloscope measurement is taken to be half of the smallest increment of the scale we were operating on. The absorption signal S is equal to the inner cavity signal S_i divided by the reference signal S_r; therefore, $\Delta S = \sqrt{\Delta S_i{}^2 + \Delta S_r{}^2}$ and $\Delta a = -\frac{m}{(S-b)^2}\Delta S$. It should be pointed out that the uncertainty ΔS calculated from the oscilloscope's smallest increment is one order of magnitude larger than the uncertainty ΔS determined during the calibration from δa_{pw}

and δa_{fw}. Fig. 69 shows a plot of the blind test data at 525 nm along with the uncertainty.

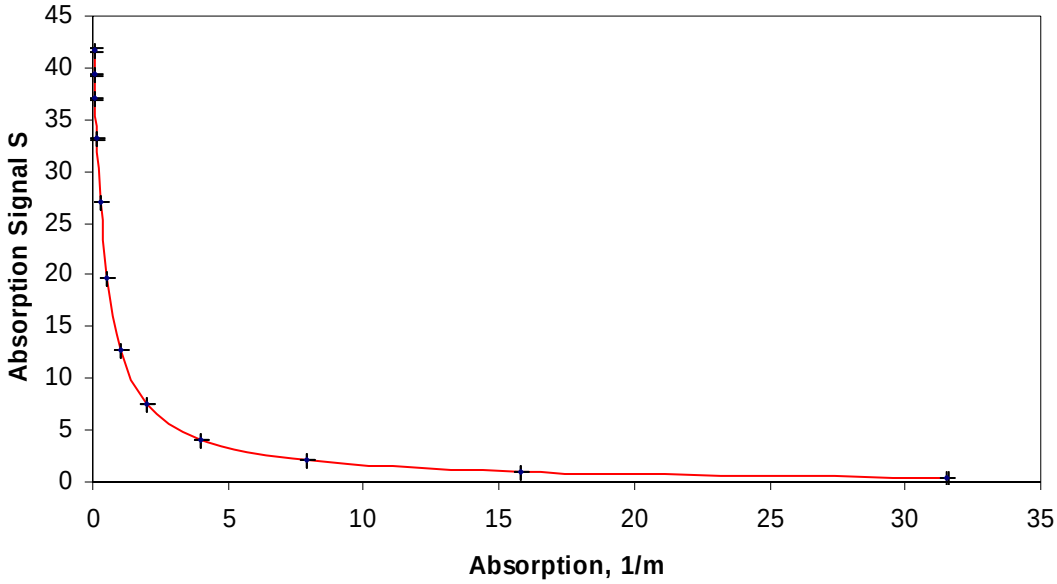

Fig. 68. ICAM calibration at 525 nm with uncertainties plotted.

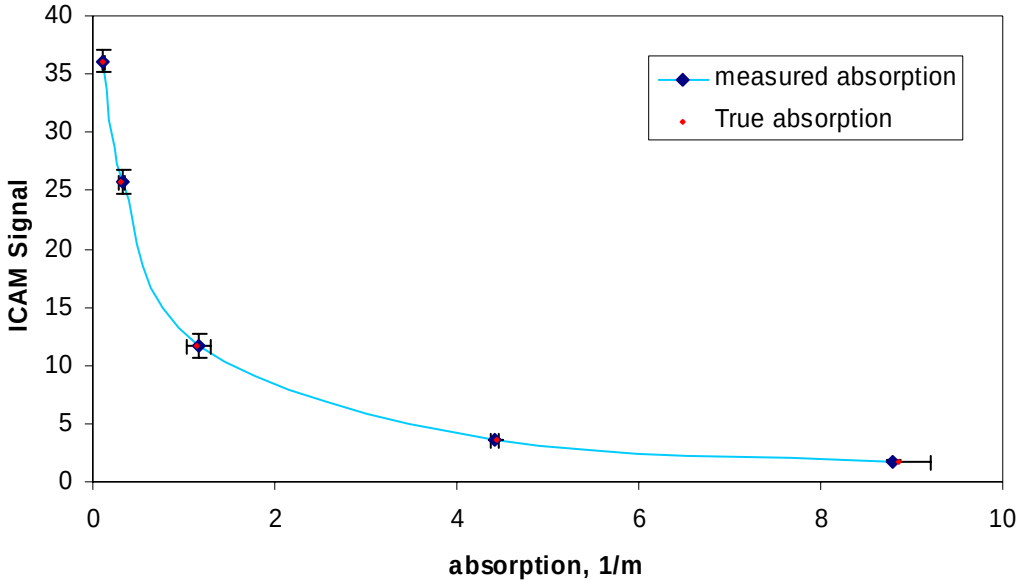

Fig. 69. ICAM blind test at 525 nm with uncertainties.

CHAPTER V

SUMMARY AND CONCLUSIONS

We have calculated the average behavior of photons in an integrating cavity, developed a new and improved diffuse reflector and constructed a flow-through integrating cavity absorption meter for use in natural waters.

1. Integrating Cavity Behavior

We demonstrated that the decay of radiation in an integrating cavity is not truly exponential; however, in cavities with a reflectivity near unity the radiation field is well modeled with an exponential decay. It was shown that the average distance a photon travels between reflections in an integrating cavity is 4V/S, regardless of the cavity geometry, provided the cavity reflectivity is near unity. Further, for any integrating cavity in which a sphere can be inscribed inside the cavity such that each face is in contact with the sphere at a minimum of one point, $\bar{d}$ =2/3 of the diameter of the sphere.

2. Diffuse Reflector

A diffuse reflector was developed that has the highest known diffuse reflectivity across the visible spectrum and on down to 266 nm. The key to such a reflector was the development of a material with ultra-high purity as well as high transmission at the wavelength of interest. To have reflectors of reasonable thickness the powder particles

must have dimensions of the order of 1 micron or less. Utilizing this material as we prescribed greatly enhances the performance of integrating cavities, increasing the optical path length by one to two orders of magnitude.

3. Flow-Through Integrating Cavity Absorption Meter

We built a flow-through integrating cavity absorption meter for natural waters. It was demonstrated to have a large dynamic range as well as high sensitivity. It has a constant cross-sectional throughput, eliminating any concerns of sample trapping during flow-through measurements. Further, it was shown to be largely independent of scattering affects over a wide range of scattering. This ability to measure such a large range of absorption levels with few detrimental scattering effects uniquely positions the ICAM for use not only in the ocean environment but also in the much more difficult river and shoreline environments.

REFERENCES

1 W. S. Pegau and J. R. V. Zaneveld, “Temperature-dependent absorption of water in the red and near infrared portions of the spectrum,” Limnol. Oceanogr. **38**, 188-192 (1993).

2 W. S. Pegau, J. S. Cleveland, W. Doss, C. D. Kennedy, R. A. Maffione, J. L. Mueller, R. Stone, C. C. Trees, A. D. Weidemann, W. H. Wells, and J. R. V. Zaneveld, “A comparison of methods for the measurement of the absorption coefficient in natural waters,” J. Geophys. Res. **100**, 13,201-13,220 (1995).

3 R. L. Miller, M. Belz, C. Del Castillo, and R. Trzaska, “Determining CDOM absorption spectra in diverse coastal environments using a multiple path length, liquid core wave guide system,” Cont. Shelf. Res. **22**, 1301-1310 (2002).

4 C. L. Gallegos, D. L. Correll, and J. W. Pierce, “Modeling spectral diffuse attenuation, absorption, and scattering coefficients in a turbid estuary,” Limno. Oceanogr. **35**, 1486-1502 (1990).

5 J. T. O. Kirk, “Estimation of the scattering coefficient of natural waters using underwater irradiance measurements,” Aust. J. Mar. Freshw. Res. **32**, 533-539 (1981).

6 T. Oishi, “Significant relationship between the backward scattering coefficient of sea water and the scatterance at 120°,” Appl. Opt. **29**, 4658-4665 (1990).

7 R. A. Maffione and D. R. Dana, “Instruments and methods for measuring the backward-scattering coefficient of ocean waters,” Appl. Opt. **36**, 6057-6067 (1997).

8 J. R. Zaneveld, J. C. Kitchen, and C. Moore, “The scattering error correction of reflecting-tube absorption meters,” in *Ocean Optics XII*, J. S. Jaffe, ed., Proc. SPIE **2258**, 44-55 (1994).

9 D. R. Dana and R. A. Maffione, “A new hyperspectral spherical-cavity absorption meter,” poster presented at AGU Ocean Sciences, Honolulu, HI, (2006), http://www.hobilabs.com/.

10 P. Elterman, “Integrating cavity spectroscopy,” Appl. Opt. **9**, 2140-2142 (1970).

11 E. S. Fry, G. W. Kattawar, and R. M. Pope, “Integrating cavity absorption meter,” Appl. Opt. **31**, 2055-2065 (1992).

12 R. M. Pope and E. S. Fry, “Absorption spectrum (380-700 nm) of pure water. II Integrating cavity measurements,” Appl. Opt. **36**, 8710-8723 (1997).

13 D. J. Gray, *Monte Carlo Solutions to the Radiative Transfer Equation in Ocean Optics: Applications to Instrument Design and Mueller Matrix Imaging* Ph.D. dissertation (Texas A&M University, 2003).

14 D. J. Gray, G. W. Kattawar, and E. S. Fry, “Design and analysis of a flow through integrating cavity absorption meter,” Appl. Opt. (to be published).

15 E. S. Fry, J. A. Musser, G. W. Kattawar, and P. W. Zhai, “Integrating cavities - temporal response,” Appl. Opt. (to be published).

16 J. Beaulieu, *A Guide to Integrating Sphere Theory and Applications* (Labsphere, Inc., 1999), http://www.labsphere.com/.

17 S. Bogacz, *Integrating Sphere Design and Applications* (SphereOptics LLC, 2004), http://www.sphereoptics.com/.

18 A. Arecchi, SphereOptics LLC, Contoocook, NH, (personal communication, slide presentation, 2005).

19 K. M. Case and P. F. Zweifel, *Linear Transport Theory* (Addison-Wesley Publishing Co., Inc., 1967). p. 56.

20 D. M. Hobbs and N. J. McCormick, "Design of an integrating cavity absorption meter," Appl. Opt. **38**, 456-461 (1999).

21 Labsphere, Inc., *A Guide to Reflectance Coatings and Materials* (Labsphere, Inc., 2006), http://www.labsphere.com/.

22 W. Möller, K. P. Nikolaus and A. Höpe, "Degradation of the diffuse reflectance of Spectralon under low-level irradiation," Metrologia **40**, S212-S215 (2003).

23 Labsphere, Inc., *Spectralon Care and Handling Guidelines* (Labsphere, Inc., 2006), http://www.labsphere.com/.

24 H. Barthel, M. Heinemann, M. Stintz and B. Wessely, "Particle sizes of fumed silica," Chem. Eng. Technol. **21**, 745-752 (1998).

25 F. E. Nicodemus, J. C. Richmond, J.J. Hsia, I.W. Ginsberg, and T. Limperis, *Geometric Considerations and Nomenclature for Reflectance* (U.S. Dept. of Commerce, NBS Monograph 160, 1977).

26 J. C. Stover, *Optical Scattering: Measurement and Analysis* (McGraw-Hill, 1990).

27 R. M. Pope, *Optical Absorption of Pure Water and Sea Water Using the Integrating Cavity Absorption Meter* Ph.D. dissertation (Texas A&M University, 1993).

28 R. Leathers, T. V. Downes, and C. O. Davis, "Analysis of a point-source integrating cavity," Appl. Opt. **39**, 6118-6127 (2000).

VITA

Joseph Alan Musser was born in Alexandria, Virginia on November 24, 1966 to Edgar and Patsy Musser. In 1984 Mr. Musser graduated from high school in Marengo, Illinois. He earned a Bachelor of Science in education from West Texas State University in 1988. He became certified by the State of Texas to teach secondary math, physical science and physics. He taught calculus, physical science, and physics at Caprock High School in Amarillo, Texas from 1988 to 1996. Mr. Musser earned his Ph.D. in 2006 from Texas A&M University. He can be reached by email at joered@tamu.edu, or by contacting Dr. Ed Fry at Department of Physics, TAMU MS4242, College Station TX 77843.